Meandering Loop Mirrors and Resonators in Silicon Photonic Integrated Circuits: Design, Fabrication, and Analysis

by

MUHAMMAD ZAKWAN

A Dissertation Submitted to the
Graduate School of Sciences and Engineering
in Partial Fulfillment of the Requirements for
the Degree of

Doctor of Philosophy

in

Electrical and Electronics Engineering

KOÇ
UNIVERSITY

August 23, 2017

Meandering Loop Mirrors and Resonators in Silicon Photonic Integrated Circuits: Design, Fabrication, and Analysis

Koç University

Graduate School of Sciences and Engineering

This is to certify that I have examined this copy of a doctoral dissertation by

Muhammad Zakwan

and have found that it is complete and satisfactory in all respects,
and that any and all revisions required by the final
examining committee have been made.

Committee Members:

Prof. Dr. İrşadi Aksun

Prof. Dr. Ali Serpengüzel

Prof. Dr. Özgür Müstecaplioğlu

Assoc. Prof. Dr. Erdem Alaca

Asst. Prof. Dr. Ahmet Öncü

Prof. Dr. Alper Kiraz

Asst. Prof. Dr. Onur Ferhanoğlu

Date: August 23, 2017

Abstract

Meandering Loop Mirrors (MLMs) and resonators based on MLMs are designed, fabricated, and analyzed using silicon integrated photonics circuit (Si-PIC) technology for operation in the standard near-infrared (near-IR) telecommunication band. Optical waveguides, directional couplers (DCs), MLMs, meandering resonators (MRs), antisymmetric meandering resonators (AMRs), and symmetric meandering resonators (SMRs) with symmetric and antisymmetric DCs were designed, fabricated, and analyzed as a function of the DC length to scan the desired near-IR telecommunication band.

A silicon on insulator (SOI) platform is used to realize strip waveguides in transverse electric (TE) mode polarized single mode configuration. The structures' design is based on numerical simulations using a photonics design kit and resulting geometry of the structures were incorporated into the photonics layout for fabrication by e-beam lithography. After the writing of the silicon strip waveguide, and before oxide deposition, the photonic structures were imaged with scanning electron microscopy (SEM) to physically characterize the fabricated devices.

Surface gratings are used to couple in and out of these photonic structures with single mode optical fibers. The excitation source for the spectral measurement of the device transmission is a tunable laser operating in the 1500 – 1600 nm wavelength range. The transmission signals in logarithmic (dB) scale are detected in the same experimental region using calibrated near-IR photodetectors. The data is acquired by a control and data acquisition computer.

The experimentally measured transmission spectra are compared with the numerically simulated transmission spectra. The normalized linear scale is used to make the peaks more prominent, whereas the logarithmic (dB) scale is used to make the dips more prominent. To make the results more reader friendly, the spectra are color coded: the normalized transmission

intensity (excluding grating couplers) are plotted in brown, the transmission intensity in logarithmic (dB) scale (excluding grating couplers) are plotted in red, the transmission intensity logarithmic (dB) scale (including grating couplers) are plotted in blue, whereas the transmission intensity (including grating couplers) are plotted in green. The free spectral range (FSR), finesse (F), quality factor (Q-factor), and extinction ratio (ER) are deduced from both the experimentally measured, and the numerically simulated transmission spectra, and were found to be in good agreement.

To understand the actual spectral response, we first analyze the simulated spectra, for the device under test. Since the input and outputs of the devices had to be connected to the grating couplers, to couple in and out from the optical fibers, the measurement responses are always modulated by the grating coupler responses, and thus cannot be directly compared to the numerical simulations. To make our simulation spectra comparable to the measurement spectra, we also simulated the transmission spectra of the devices including the grating couplers.

First we analyze the wavelength dependence of a DC, one of the basic elements used in our designs. We look at the coupled and the transmitted port intensities, and compare them with the measurement results. Then we look at the MLM spectral response, which incorporates a DC. After developing the understanding of DC and the MLM, we move to the analysis of the spectral responses of more complex structures, e.g., MR, AMR, SMR.

The general response of a tunable mirror is observed for the MLMs. MRs show the typical Fabry-Pérot response. The AMRs show the typical spectra similar to the coupled resonator induced transparency (CRIT), the analogue of the electromagnetically induced transparency (EIT) spectral responses. Whereas the SMRs show the mode split Fano resonance spectral responses.

All in all, MLMs and resonators based on MLMs show promise as a novel integrated photonics platform for Si-PIC elements for optical communication, computation, and sensing.

Özet

Kıvrımlı halka yansıtıcıları ve kıvrımlı halka yansıtıcı tabanlı çınlaçların tasarımı, üretimi ve incelemesi, yakın kızılaltı telekomünikasyon bandındaki işlemler için, silikon tümleşik fotonik devre teknolojisi kullanılarak yapılmıştır. Optik dalgakılavuzları, yönlü bağlaştırıcılar, kıvrımlı halka yansıtıcılar, kıvrımlı çınlaçlar, simetrik olmayan kıvrımlı çınlaçlar, ayrıca simetrik ve simetrik olmayan yönlü bağlaştırıcılar ile birlikte simetrik kıvrımlı çınlaçlar tasarlanmış, üretilmiş, ve yönlü bağlaştırıcıların uzunluğuna bağlı taranarak istenen yakın kızılaltı dalgaboylarında incelenmiştir.

Bir yalıtkan üstü silisyum düzlemi kullanılarak elde edilen şerit dalgakılavuzlarının enine elektrik kutbunda, ve tekil dalga kipinde çalışan yapısı gözlemlenmiştir. Yapılar, bir fotonik tasarım yazılımı yardımı ile sayısal benzeşimler kullanılarak tasarlanmış ve elde edilen yapı biçimleri bir fotonik taslak çizimine dönüştürülerek elektron ışını ışık yazımına hazır hale getirilmiştir. Şerit silisyum dalgakılavuzu yazılımından sonra, ve oksit çökeltmesinden önceki fotonik yapılar, üretilen aygıtların tanımlanması için taramalı elektron mikroskobu yardımı ile görüntülenmiştir.

Tek kipli optik lifler yüzey ızgaraları kullanılarak bu fotonik yapılara bağlaştırılmıştır. Aygıt geçirgenliklerinin izge ölçümleri için uyarma kaynağı olarak 1500-1600 nm dalgaboyları arasında çalışan bir ayarlanabilir lazer kullanılmıştır. Logaritmik (dB) ölçekteki geçirgenlik sinyalleri aynı deneysel bölgede ölçeklendirilmiş yakın kızılaltı fotoalgılayıcılar ile ölçülmüştür. Veriler bir denetleme ve veri edinim bilgisayarı tarafından sağlanmıştır.

Deneysel olarak ölçülen geçirgenlik izgeleri ile sayısal benzeştirilmiş geçirgenlik izgeleri karşılaştırılmıştır. Tepeleri öne çıkarmak için ölçütlendirilmiş doğrusal ölçek kullanılmıştır, ancak çukurları öne çıkarmak için logaritmik (dB) ölçek kullanılmıştır. Sonuçları okuyucuya daha iyi sunmak için, izgelerde bir renk kodlaması kullanılmıştır. Bu kodlamada

ölçütlendirilmiş geçirgenlik şiddeti (ızgara bağlaştırıcılar harici) kahverengi ile, logaritmik (dB) ölçekteki geçirgenlik şiddeti (ızgara bağlaştırıcılar harici) kırmızı ile, logaritmik (dB) ölçekteki geçirgenlik şiddeti (ızgara bağlaştırıcılar dahil) mavi ile, ve geçirgenlik şiddeti (ızgara bağlaştırıcılar dahil) ise yeşil ile gösterilmiştir. Gerek deneysel sonuçlar gerekse sayısal benzeştirilmiş geçirgenlik izgeleri kullanılarak boş izge aralığı, incelik, nitelik katsayısı, ve söndürme oranı (dB) ölçülmüş, ve karşılaştırılarak birbirleri ile uyumlu olduğu gözlemlenmiştir.

Asıl izge sonuçlarını anlamak için, öncelikle denenen aygıtın benzeştirilmiş izgeleri incelenmiştir. Üretilen aygıtların giriş ve çıkışları ızgara bağlaştırıcılara bağlı olduklarından, ve ölçülen sonuçlar, ızgara bağlaştırıcıların yanıtları tarafından sürekli kiplendirildiklerinden dolayı, geçirgenlik izgelerinin benzeştirilmiş sonuçları ile doğrudan karşılaştırılamaz. Bu karşılaştırmayı sağlayabilmek için benzeştirilmeler ızgara bağlaştırıcıları eklenmiş aygıtlar ile gerçekleştirilmiştir.

İlk olarak, yönlü bağlaştırıcıların dalgaboyu ile ilişkisi incelenmiştir, çünkü yönlü bağlaştırıcılar tasarımlarda kullanılan en temel unsurlardan biridir. Bağlaşmış ve iletilmiş kapı şiddetleri incelenmiş, ve ölçüm sonuçları ile karşılaştırılmıştır. Daha sonra, bir yönlü bağlaştırıcıdan oluşan kıvrılan halka yansıtıcısının izge yanıtına bakılmıştır. Yönlü bağlaştırıcı, ve kıvrımlı halka yansıtıcıları için bir anlayış edinildikten sonra, kıvrımlı çınlaç, simetrik olmayan kıvrımlı çınlaç, ve simetrik kıvrımlı çınlaç gibi yapılar incelenmiştir.

Kıvrımlı halka yansıtıcılar için ayarlanabilir aynaların genel yanıtları gözlemlenmiştir. Kıvrımlı çınlaçlar sıradan Fabry-Pérot yanıtı göstermiştir. Simetrik olmayan kıvrımlı çınlaçlar ise bağlaşmış çınlaç etkisiyle saydamlığa benzeyen bir izge göstermiştir. Bu durum elektromanyetik etkisiyle saydamlığın ortaya çıkarttığı izgenin bir benzeşimidir. Simetrik kıvrımlı çınlaçlar ise kip ayrıklı Fano çınlaması içeren izgeler sergiler.

Sonuç olarak, kıvrımlı halka yansıtıcılar, ve kıvrımlı halka yansıtıcı tabanlı çınlaçlar, yeni ve gelecek vaat eden silikon tümleşik fotonik devre unsurları için bir tümleşik fotonik düzlemi olarak optik iletişim, hesaplama, ve algılama uygulamaları için kullanılabilir.

Acknowledgements

I want to express my deep gratitude to all the people, who helped in making this thesis a success. Without their significant contributions, this work would have been impossible.

I would like to thank my thesis advisors professor İrşadi Aksun and professor Ali Serpengüzel for providing me with the opportunity to work at Koç University (KU), and for their valuable time and guidance, the committee members professor Özgür Müstecaplıoğlu, professor Erdem Alaca, professor Ahmet Öncü for their guidance, and my thesis jury members professor Alper Kiraz and professor Onur Ferhanoğlu, for their valuable time and feedback. I am very grateful to professor Mehmet Cengiz Onbaşlı for his contributions and directions towards my work. Also I would like to mention professor Şükrü Ekin Kocabaş for contributing to my education and traning in the field of photonics.

I would also like to thank all the current and the previous members of KU Microphotonics Research Laboratory, Ulaş Sabahattin Gökay, Imran Khan, Farhan Azeem, Muhammad Rehan Chaudhry, Syed Sultan Shah Bukhari, Suat Kurt, Nurperi Yavuz, Hüseyin Ozan Çirkinoğlu, Mohammed Sharif Murib, Yiğit Uysallı, Abdullah Demir, Mustafa Mert Bayer, Mehmet Ali Anıl, Ceren B. Dağ, Muhammad Hamza Humanyun, Oğuzhan Mete Öztürk, Zeeshan Rashid, and Muhammad Sohail Anwar for their help and support. I would like to mention some university colleagues, who have helped me throughout my stay at KU, Nabil Khalid, Rizwan Saddiq, Aatif Ijaz, Naveed Ahmed Abbasi, Syeda Narjis Fatima, Nusrah Hussain, Shoaib Rehman Somroo, Haris Shehzad, Aziz Karasahin, Mustafa Eryürek, Ismail Yorulmaz, Haroon Qureshi, Abdul Rehman, and Talha Irfan Kahan.

I acknowledge professor Lukas Chrostowski for offering the edX UBCx Phot1x Silicon Photonics Design, Fabrication and Data Analysis course, which is supported by the Natural

Sciences and Engineering Research Council of Canada (NSERC) Silicon Electronic-Photonic Integrated Circuits (SiEPIC) Program.

The devices were fabricated by Richard Bojko at the University of Washington, Washington Nanofabrication Facility, part of the National Science Foundation's National Nanotechnology Infrastructure Network (NNIN), and Cameron Horvath at Applied Nanotools, Inc. Enxiao Luan performed the measurements at The University of British Columbia.

I would like to acknowledge support from the Higher Education Commission (HEC) of Pakistan, and the Society of Photo-Optical Instrumentation Engineers (SPIE).

I am grateful to my parents, siblings, and family for all the help and support, which they have provided me throughout my life.

Dedicated to my family

Table of Contents

List of Figures

1 Introduction

1.1 Photonics

Photonics is virtually used by everyone today. The invention of the fiber optic cable [1], which uses optical signals to transmit data rather than electrical signals, had been one of the most distinctive developments of optics and photonics. In recent years photonics has found its way in other applications such as sensing [2], and data center communication [3].

Integrated circuits (ICs) until recently were based on electronic components only. In the past, with the advancement in the complementary metal oxide semiconductor (CMOS) technology the size of the electronic components had been decreasing, hence the industry was able to keep up with the demand of providing higher processing capabilities in a smaller chip area. However since the information carriers in the CMOS technology are electrons, which, due to their inherent properties, cannot keep up with the future demands of ultra-high-speed data transfer between multiple devices and chips. The increase in the communication bandwidth requires that, the next generation communication systems be shifted from copper wire to optical waveguides to match the market demands, a comparison between the two technologies has been presented [4]. Optical components have potential benefits in achieving high data rates, energy efficiency, and high interconnect density. Photonic components, such as wavelength splitters, are developed to couple the signal into the optical fibers for long range communications. Dense waveguides are critical for on board or on-chip, optical waveguiding purposes.

1.2 Integrated photonics

Optical waveguides and devices, are suitable candidates for ultrahigh speed data transfer applications. However, optical devices are not as good as CMOS electronic devices, when it comes to data processing, so the solution lies somewhere in between the electronics and photonics. In the integrated photonic circuits, the idea is to use photons to transmit and receive information instead of electrons. Since photons can travel extremely fast and have no mass, when compared to electrons, the idea of integrating photonic components into electronic chips have opened up the door to a new era of ultrahigh speed data processing and transmission. In future chips, further scaling of interconnect capacity may be achieved by advancements in optics [5].

1.2.1 Integrated photonics over fiber optics

Integrated silicon photonics offers advantages over fiber optics such as monolithic integration, smaller dimensions of devices with similar functionality and performance. The compatibility with well-established silicon CMOS technology of highly controllable silicon wafers, developed for the microelectronics industry, is a huge benefit to for photonics industry [6], providing a high index contrast, and low power consumption with respect to bulk components in telecommunication and signal processing [7]. Integrated silicon photonic platforms and devices are thus seen as promising building blocks for realizing silicon photonic integrated circuits (Si-PICs) and devices [8, 9].

Another key advantage of Si-PICs is that, integrated photonic waveguide geometries can be used for waveguide based lasers, channels, signal processors, photodetectors, as well as sensors.

A number of photonic resonator structures have been investigated analytically, numerically, and experimentally, as these structures can be applied for a range of components in Si-PICs.

Integrated photonics offers a two-dimensional or three-dimensional platform solution to the one-dimensional solution of fiber optics. Integrated photonics is the analogue of integrated electronics, whereas fiber optics is the analogue of electronic circuits assembled from discrete electronics components.

1.2.2 Integrated photonics Platforms

1.2.2.1 Silicon On Insulator (SOI)

Silica (SiO_2) is the most abundant mineral in Earth's crust. It has vast importance in many technological areas. SiO_2 exist in form of a linear molecule in the gas phase. SiO_2 has positive electron affinity. The molecule is very stable [10]. SiO_2 belongs to the family of metalloid oxides. These inorganic compounds contain the oxygen atom in oxidation state of -2, in which the heaviest atom bonded to the oxygen is a metalloid, therefore it is non-toxic and non-hazardous (III-V's can be poisonous/expensive/integration issues), and the integration with CMOS industry is relatively easy.

1.2.2.2 Silicon Nitride (SiN)

Silicon Nitride (Si_3N_4) is not as abundantly present in Earth's crust compared to vast availability of silica. Si_3N_4 is a non-oxide man-made material synthesized by the nitridation of silicon in N_2 atmosphere furnaces. Like other high tech materials, recent advances in super fine powder processing, and controlled atmosphere kilns have led to a commercial revival in the manufacturing, and use of this long known, but little used material. [11]

1.2.2.3 Gallium Arsenide (GaAs)

Gallium arsenide (GaAs) is also produced artificially via Czochralski or Horizontal Bridgeman technique. It is very problematic to obtain high purity single GaAs crystals, except under tightly controlled environmental conditions using Czochralski technique. Whereas, in Horizontal Bridgeman technique, GaAs is obtained by means of a self-limiting reaction, which hinders the

growth of large crystals. Also, in this latter technique, the process produces single crystals only under rigidly controlled conditions.

Most noticeable disadvantages of this method are as follows: alkyls of the group III elements are pyrophoric, whereas group V hydrides such as ASH, are extremely toxic. There are potential environmental, safety, and health hazards of handling these reagents. The high reactivity of these compounds makes them difficult to purify and handle. After purification, they are susceptible to reaction with their storage containers, thus introducing new contaminants. Problems include carbon incorporation, and the difficulty in maintaining the desired film stoichiometry, when growing ternary and quaternary compounds.[12]

1.3 Si-Photonic Integrated Circuits (Si-PIC)

In recent years, **silicon photonic integrated circuits (Si-PICs)** have become one of the most promising and fastest-improving photonics platforms [13]. With monolithic integration and silicon photonics, one can reduce the cost per telecommunication bandwidth, the chip power consumption per transmitted bit, and the component footprint. The improvement of silicon photonics can be attributed to the significant cost reductions in telecommunication and sensing devices by monolithic integration and mass manufacturing, well-developed and standardized silicon CMOS processing methods, well-established Si-CMOS microelectronic fabrication facilities, stable SiO_2, and highly reproducible dopant profiles in high-quality silicon wafers, as well as high-index contrast between silicon and air (or silica (SiO_2)).

Moreover, the existing CMOS technology facilities are another reason for the huge improvement over the several decades, and the microelectronics fabrication facilities, which are already used in CMOS technology, allows the photonic circuit elements to be produced with not much effort [14].

1.3.1 Photonic Components

Waveguides are vastly used as connection structures on silicon-on-insulator (SOI) platforms are composed of a silicon core (with n_{Si}= 3.47 near 1550 nm), a bottom layer of native silicon dioxide (SiO_2) (n_{SiO2}= 1.44 near 1550 nm), and a lower index top cladding (air or silicon oxide), as they help confine the waveguide eigenmodes in the transverse and lateral coordinates [13]. However, having a top layer composed of SiO_2 is desirable, because the SiO_2/Si/SiO_2 structure enables a symmetric mode profile, and lower loss due to substrate leakage.

The high refractive index contrast of **silicon-on-insulator (SOI)** photonics enables tight confinement of light in sub-micrometer waveguides, and sharp waveguide bends; making SOI promising for developing Si-PICs with high integration densities. In applications such as wavelength division multiplexing (WDM), Si-PICs often require precise matching of the central wavelength and the waveguide propagation constant between the components on a chip, such as ring resonators, and other optical filter structures. [15]

Si-PICs using a CMOS process for **monolithic photonic** and electronic integration have already been demonstrated for communication applications [16]. Also, **WDM** systems are one of the most efficient building structures in optical fiber communications [17] and integrated photonics [18], to expand the channel capacity, and increase the data transmission rates.

1.3.2 Advancements in Si photonics

Coupled resonator optical waveguides (CROWs) [19] are taking a lot of attention in recent years due to their potentials to be used in application areas such as optical filtering [20], high ordered filters [21], optical switching [22], nonlinear optics [23, 24], dispersion compensation [24], and optical buffering [23].

In WDM systems, optical interleavers are the fundamental building blocks to multiplex and demultiplex the signal both at the transmitter and the receiver sides [25, 26]. Due to its low

power consumption, compact, and broadband qualities a silicon photonics interleaver is necessary in all kinds of interleavers [27], and it is seen as one of the key structures in the future WDM applications. For multiplexing and demultiplexing the signals in the communication channels, different devices such as arrayed waveguide gratings (AWGs) [28], and Bragg gratings [29] are used. In many applications, an individual device operates in a limited wavelength range (< 30 nm). Also, in WDM systems, standard channel spacing is either 100 GHz (0.8 nm) or 200 GHz (1.6 nm), which requires a relatively small FSR. Also, high performance devices such as AWGs [8], waveguide crossing [30], high speed modulators [31], and photodetectors [32] are realized on SOI platforms. As the devices in the SOI platform increase in terms of quality and quantity, many platforms do not provide an integrated laser source [29]. A suitable way to implement mirrors on integrated chips is to use distributed Bragg reflectors (DBRs) [33]. Due to the high index contrast between silicon (Si) and silicon dioxide (SiO_2), narrow gratings on submicron waveguides require a size of less than 50 nm, beyond the current lithography technology, which works down to 100 nm. These structures are very sensitive to fabrication errors.

1.3.3 Applications and future of silicon photonics

As Si-PIC follows the development trajectory of microelectronics, and offers significantly wider bandwidth, and lower cost per flop and transmitted bit, one may expect highly-promising applications to emerge out of Si-PIC research in the next few decades in the fields of sensing, data communication, security, and medical technology.

The proposal to use optical interconnects instead of electronic vias [34] lays out the future of optical connectivity in the data center [3]. The fundamental limit for optical components [35], and device requirements for optical interconnects to silicon chips [5] have been studied. A review of recent Si photonics [36], and the appearance of high bandwidth on-chip Si-photonic

interleavers [37] herald that, silicon photonics based optical communication, computation, and sensing will develop at an ever increasing speed.

1.4 Grating couplers

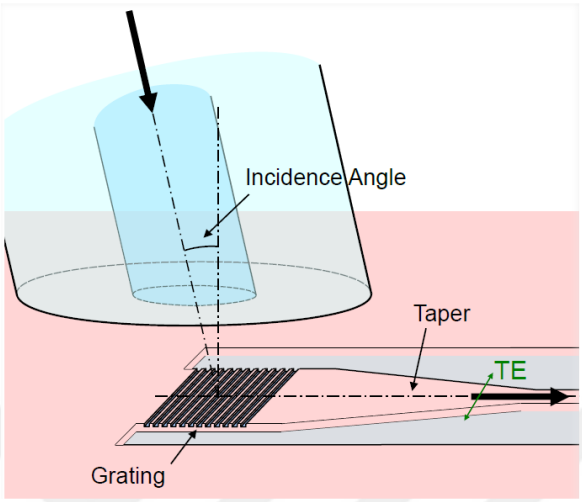

Figure 1.1: Coupling of light signal from an optical fiber to a grating coupler.

To couple the signal to and from an optical fiber, we used grating couplers. Figure 1.1 shows the illustration of the optical fiber to grating coupler. The grating couplers can be optimized for coupling a certain waveguide mode. In our designs, we used grating couplers optimized for the TE mode [38].

A diffraction angle is defined as the angle between the normal of the grating, and the diffraction direction of the light wave. The incident angle of the sub-wavelength grating coupler is determined by the diffraction angle of the grating. The optimized subwavelength grating coupler for the TE_{00} mode has a 593 nm grating period, a 237 nm grating width, and a 74 nm subwavelength grating width.

1.5 Waveguides

The high refractive index contrast of **silicon-on-insulator (SOI)** photonics enables tight confinement of light in submicron waveguides, and sharp waveguide bends, making SOI promising for developing Si-PICs with high integration densities. In applications such as WDM,

PICs often require precise matching of the central wavelength and the waveguide propagation constant between components on a chip, such as ring modulators, and optical filters [15].

1.5.1 Waveguide Types

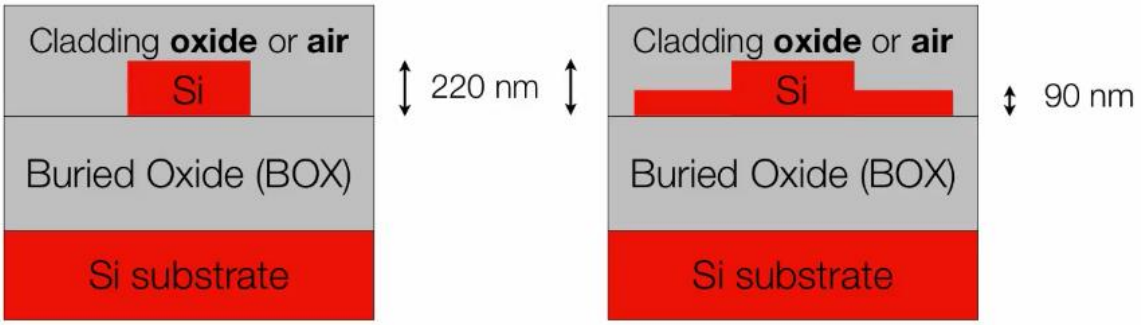

Figure 1.2: 2D cross section of strip (left) and rib (right) waveguides on an SOI platform.

In an SOI platform, the most commonly used waveguides are strip and rib waveguides, the 2D cross sections of these waveguides are shown in Figure 1.2.

Strip waveguides are suitable for use in passive devices, these waveguides can accommodate tight bends, and can be useful in making small footprint devices. The disadvantage is that, these waveguides are sensitive to side wall variations, so the fabrication process has to be precise. Comparison between rib and strip waveguides in SOI is well studied [39].

1.6 Optical Resonators

An optical resonator, is an arrangement of reflectors, which forms a standing wave cavity for light waves. Optical resonators are key components in developing active components such as lasers, as they surround the gain medium, and provide feedback of these devices. Resonators are also used in optical parametric oscillators (OPOs), interferometers [40], optical switching [41], feedback control and on-chip transparent monitoring [42].

1.6.1 Optical resonators

1.6.1.1 Fabry–Pérot resonator

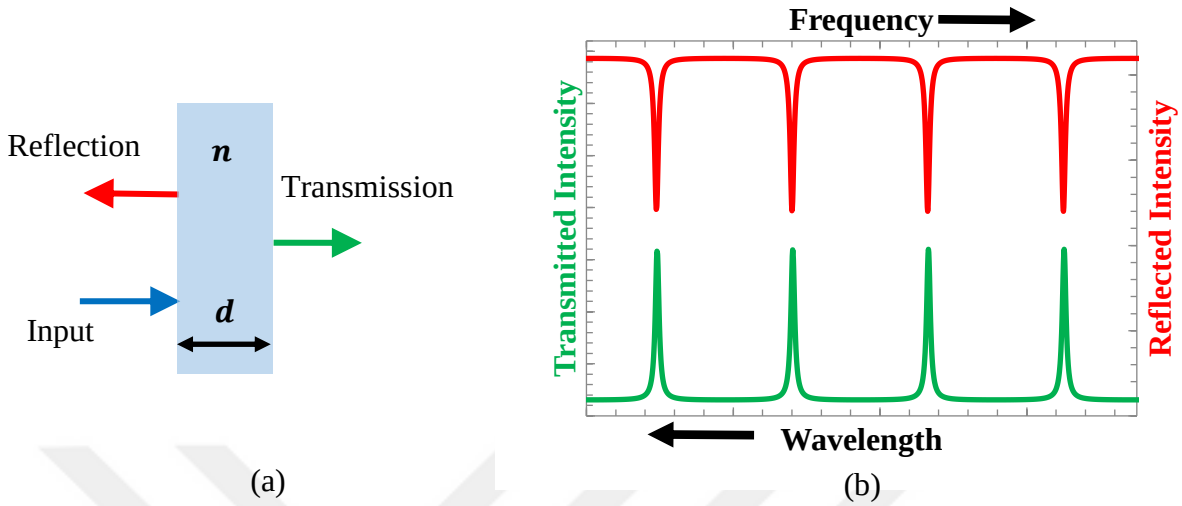

Figure 1.3: Block diagram of a Fabry–Pérot etalon with the reflection and transmission spectra.

Consider a Fabry–Pérot etalon with a slab thickness d, and refractive index *n*, as shown in Figure 1.3 (a). Transmittance of an ideal Fabry–Pérot resonator with equal reflectance R for both mirrors, are given by the following equations [43].

$$T = \frac{(1-r)^2}{1 - 2r\,cos\delta + r^2} \tag{1.1}$$

$$R = 1 - T \tag{1.2}$$

where r is the reflectivity of the mirrors and δ is the phase difference between the two successive transmitted waves. The transmission and reflection for a Fabry–Pérot etalon are plotted in Figure 1.3 (b), when light is launched into the resonator under normal incidence.

1.6.1.2 Spherical resonators

The microsphere resonator is the three dimensional analogue of the Fabry-Pérot resonator, and can be used as a channel dropping filter [44]. Figure 1.4 shows the schematic of a channel

dropping filter realized with a microsphere resonator. With spherical geometries, much higher Q-factors can be achieved. Since spherical resonators are three dimensional structures, they can accommodate extra Eigen modes not accessible in planar resonators. Fabrication of such structures with current lithographic process remains a challenge though.

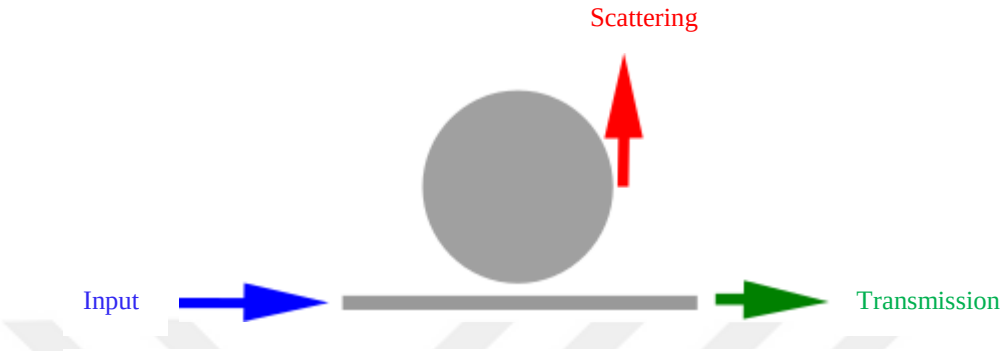

Figure 1.4: Channel dropping filter realized with a microsphere resonator.

1.6.1.3 Ring resonators

Figure 1.5 shows a ring resonator coupled to an optical waveguide. The relations for coupling of optical powers between the waveguide and the ring are studied in [45]. The transmission

Figure 1.5: A channel-dropping filter realized with a ring resonator.

spectra of the waveguide coupled to a ring looks similar to the reflection spectra of the FP resonator as shown in Figure 1.3 (b).

1.6.2 Meandering Resonators

Meandering resonators are based on meandering loop mirror (MLM) or the Sagnac loop mirror.

1.6.2.1 Meandering Loop Mirrors (MLM)

Meandering loop mirror (MLM) works on the principle of interference. The incoming beam is split into clockwise (CW) and counterclockwise (CCW) paths, these beams are brought

together at the coupling points, due to the different phases accumulated by the counterpropagating beams the interference can be either constructive or destructive, leading to different reflected and transmitted intensities.

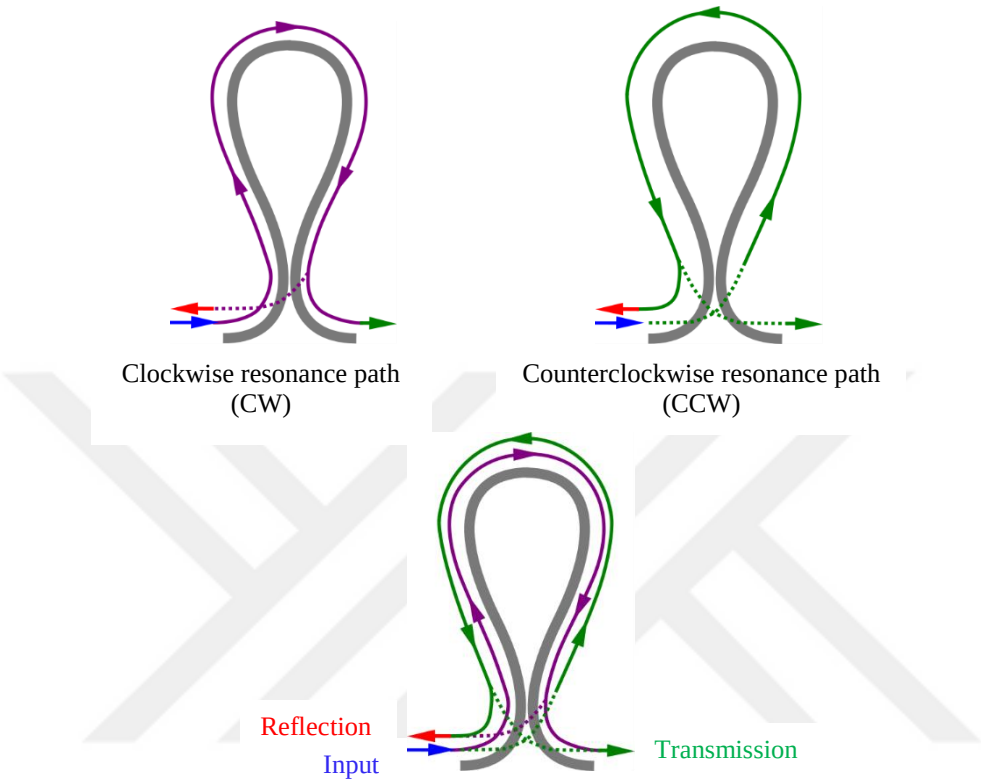

Figure 1.6: MLM interferometer with CW and CCW beams interfering at the coupling point.

Meandering loop mirror (MLM) structures can be produced on SOI platforms [46]. SOI loop mirrors have several applications as sensors [47], thermo-optical switches [48], and laser cavities [29]. In this doctorate thesis, several SOI MLMs are investigated with different coupling lengths and structures. Experimental spectra are analyzed in comparison with the theoretical, and numerical simulation spectra. The MLM transmission is analyzed in the near-IR C-band from 1500 nm to 1580 nm for the experimental spectra, and 1500 nm to 1600 nm for the simulation spectra.

1.6.2.2 Meandering Resonators (MR)

Meandering Resonators (MR) can be considered as one of a building block for integrated Si-PICs. These resonators are integrated photonic waveguide structures, which consist of two

cascaded meandering loop mirrors (MLMs) [46, 49]. In a configuration of two cascaded MLM's, each MLM behaves as a mirror, and the path adjoining the two MLMs is the thickness of the cavity, with resonance modes traveling in both CW and CCW directions as shown in Figure 1.7. Such a resonator have an added advantage over the conventional resonator systems in terms of feedback, which is inherent property of an MLM.

Two cascaded MLMs behave like a Fabry-Pérot cavity [43]. MRs have been previously used as resonating structures in optical circuits to produce tunable lasers, [50] and filters [51] in optical fibers. MRs in optical fiber form were also studied for their optical bistability, instabilities, and power limiting behavior [52]. In addition to MLMs behaving as mirrors in MRs, MRs can also function as two interferometers coupled together to form a resonating structure [53].

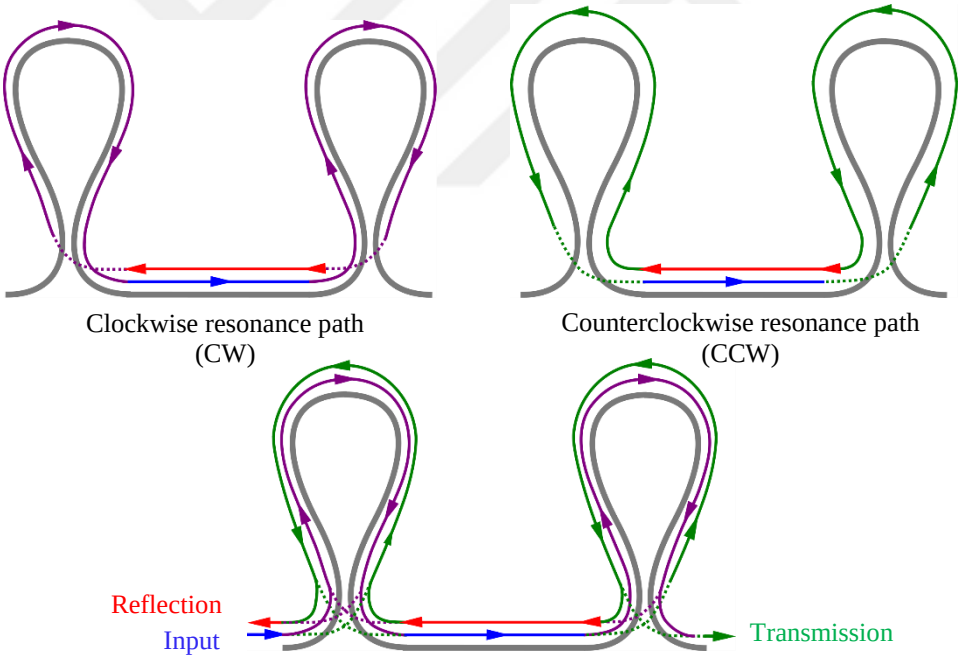

Figure 1.7: MR diagram with CW and CCW resonance paths.

By coupling two interferometers, one can extend the free spectral range (FSR) of the overall structure by using the Vernier effect, which provides more capabilities for enhancing the dynamic range, and sensitivity of MLM-based sensors, as applied in optical fibers [54]. MRs have been utilized in SOI platform to realize optical comb filters [53, 55, 56].

In this doctorate thesis, we propose MR based structures, which can be used to design integrated lasers, filters, and sensors on SOI platform with extended dynamic range and sensitivity. We design and investigate various MR structures with both symmetric and asymmetric MLMs to achieve different coupling coefficients. Our analyses are based on an SOI platform within the 1500-1600 nm wavelength range.

1.6.2.3 Antisymmetric Meandering Resonators (AMR)

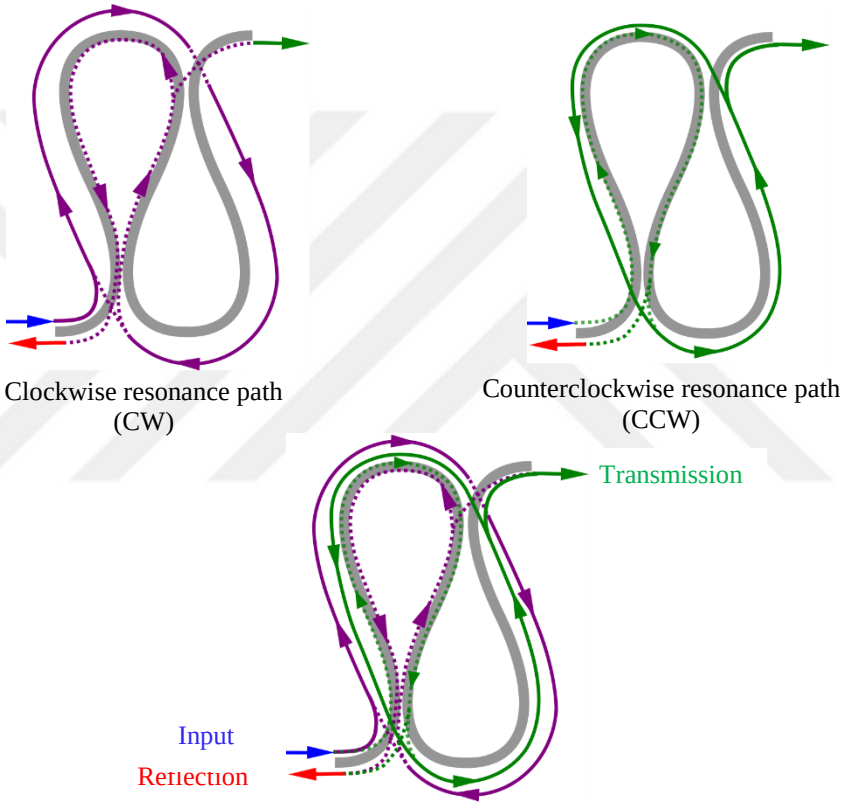

Figure 1.8: AMR with CW and CCW resonance paths.

Antisymmetric Meandering Resonators (AMR) can be realized by cascading a half MLM section after a full MLM, in such a way that, two coupling points are created at the top and the bottom, as shown in Figure 1.8. Coupled mode theory analysis for mode splitting in a coupled cavity system was performed [46, 57], cascaded SCOW structures were analyzed [58] and two stage cascaded SCOW were demonstrated [59]. AMR structures have been also been investigated for coupling tuning the transmission spectra [60], and for high-speed fourth-order

photonic differentiator [61]. On-chip all-optical analogue to electromagnetically induced transparency [62] has been demonstrated by using coupled ring resonator structures. Later on, the same effect was demonstrated on the AMR/SCOW structure [63] with a smaller footprint.

1.6.2.4 Symmetric Meandering Resonators (SMR)

Symmetric Meandering Resonators (SMR) have been proposed and analyzed [64] as an alternative SCOW structure with additional spectral properties. SMRs have been also proposed and analyzed as a special case of the distributed meandering waveguide (DMW) structures [46]. The SMR can be tuned to exhibit a mode split [65] of both Lorentzian and Fano resonance lineshapes, which can be useful for spectral filtering applications.

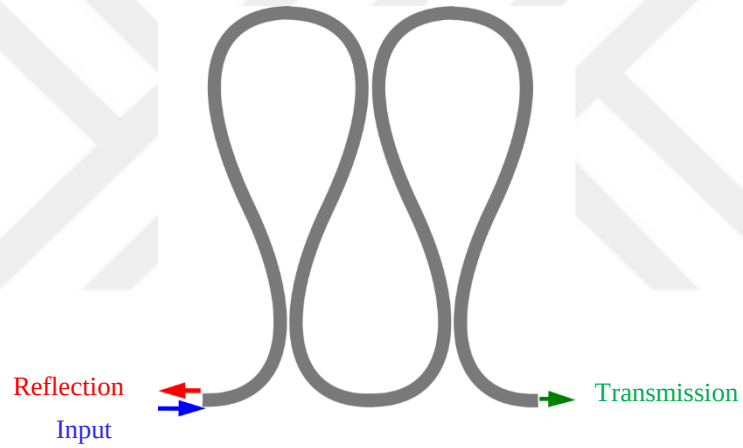

Figure 1.9: Symmetric Meandering Resonators (SMR) structure.

1.6.2.5 Distributed Meandering Waveguide (DMW) structures

SMDFB was proposed [66] and recently used as interleavers [67] in WDM odd / even channel separation. The simpler version of the SMDFB, the MDFB (cascaded MRs) were proposed [26] and analyzed [68] for integrated photonic devices. The MDFB is basically a one-dimensional photonic crystal structure composed of MLMs, exhibiting photonic bandgaps (PBGs).

1.7 Transfer Matrix Method (TMM)

The transfer matrix method (TMM) allows the multiplication of cascaded multiport device responses, if their scattering matrix (input / output responses) are known. For each device port,

there is an additional dimension added to the transfer matrix, i.e., a 2 port device requires a 2 x 2 matrix, a 6 port device requires a 6 x 6 matrix. This technique is fast and efficient in calculating the response of a cascaded system. TMM has been used to calculate the transmission equations for the distributed feedback (DFB) structures of MR, AMR, and SMR [46]. TMM approach provides an exact answer for one-dimensional structures such as thin-film reflectors, and distributed Bragg reflectors (DBRs). The use of TMM approach in Si-PICs requires an approximation of the structure as being one-dimensional, such as a Bragg grating, where the structure is assumed to have a varying index of refraction in the direction of propagation, but where the transverse geometry does not change.

1.8 Figures of Merit

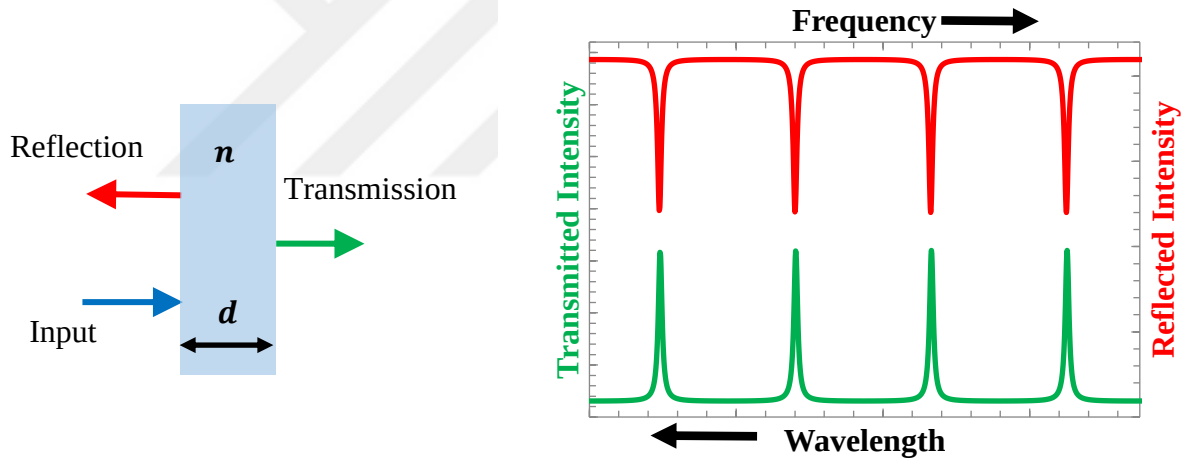

Figure 1.10: Block diagram of a Fabry–Pérot etalon with the reflection and transmission spectra.

To characterize our photonic devices, we have used the figures of merit described in the subsequent sections, with respect to the Fabry–Pérot resonator [43]. Consider a Fabry–Pérot etalon with a slab thickness d, and refractive index *n*, as shown in Figure 1.10. The transmission and reflection for Fabry–Pérot etalon are also plotted in Figure 1.10.

1.8.1 Quality Factor (Q)

The Q-factor is a parameter that relates the stored and dissipated energies of an oscillatory system, mathematically

$$Q = \frac{\nu_m}{\delta\nu} \tag{1.3}$$

where ν_m is the resonant frequency of the m^{th} mode, $\delta\nu$ also known as the linewidth, is the frequency band around which, the transmission intensity value drops to half compared to its peak value.

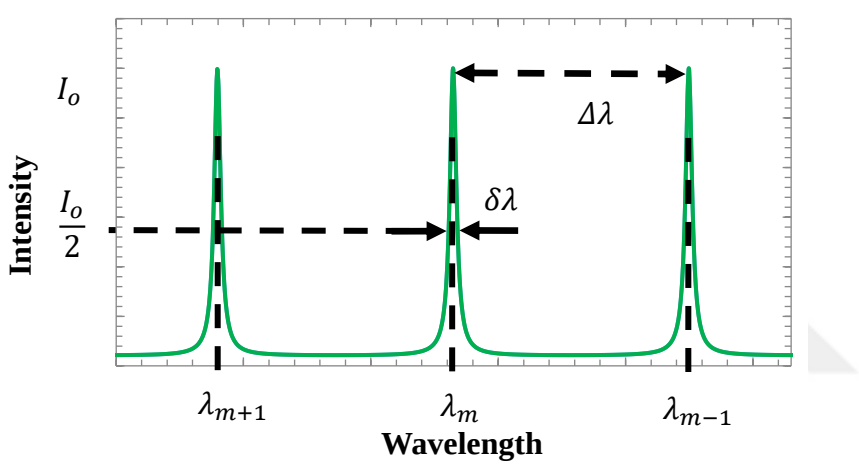

Figure 1.11: Transmission spectrum of a Fabry–Pérot etalon plotted with respect to wavelength.

For very high Q factor values, it is also approximated by the following relation.

$$Q = \frac{\lambda_m}{\delta\lambda} \tag{1.4}$$

where $\lambda_m$the resonant wavelength of the m^{th} mode, $\delta\lambda$ also known as the full-width-half-maximum (FWHM) is the wavelength band around the resonant wavelength, λ_m, where the transmission intensity value drops to half compared to its peak value. In a Fabry-Pérot etalon, a peak is observed in the transmission intensity, and a dip is observed in the reflection intensity at $\lambda_m$condition.

The sharper the dip becomes, the higher the Q factor value is achieved. For most applications, a higher the Q factor value is desirable.

1.8.2 Free spectral range (FSR)

The free spectral range (FSR) is an important parameter of a resonator device. It is a measure of the optical bandwidth between two successive resonant conditions

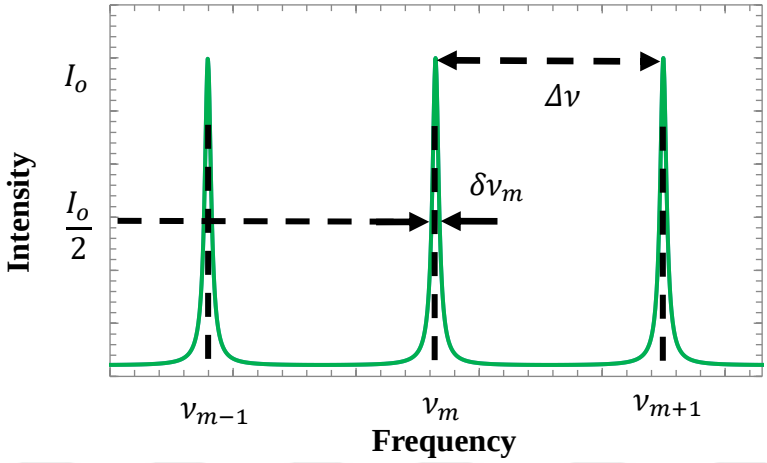

Figure 1.12: Transmission spectrum of a Fabry–Pérot etalon plotted with respect to frequency.

$$FSR = \Delta\nu = \frac{c}{opl} = \frac{1}{T_R} \tag{1.5}$$

$$opl = n\,L \tag{1.6}$$

where, c is the speed of light in vacuum, n the refractive index of the material, opl the optical path length of the resonator, and L the total length of the resonator, which is $2d$ for the Fabry-Pérot resonator in Figure 1.10. Round trip time T_R, is the inverse of FSR. Alternatively, the FSR can be approximated to the following formula in terms of wavelength.

$$FSR = \Delta\lambda \approx \frac{\lambda^2}{opl} \tag{1.7}$$

In an optical sensor application, the dynamic range of the sensor is generally limited due to the FSR, so a higher value can be desirable for certain applications. To study, how the FSR is

effected in our devices, we have considered structures with both constant and varying optical path lengths.

1.8.3 Finesse (F)

The finesse relates the $\Delta\lambda$ (FSR) to the $\delta\lambda$ (FWHM) by the following expression:

$$F = \frac{\Delta\lambda}{\delta\lambda} \tag{1.8}$$

In a communication system, F is the total number of usable channels in one FSR.

1.8.4 Extinction ratio (ER)

In an optical system, the extinction ratio (ER) is the ratio of two optical power levels. For the case of Fabry-Pérot resonator, ER can be defined as the peak transmission intensity (on resonance condition) to the minimum transmission intensity (off resonance condition).

$$ER = \frac{I_o}{I_{min}} \tag{1.9}$$

2 Methods for Simulation, Design, Fabrication, & Characterization

2.1 Numerical Simulations

For simulation of our structures, we used a Finite Difference (FD) technique. The FD technique is particularly well suited for Si-PIC, since it has high refractive index contrast structures, and has the benefit that, the cubic mesh is compatible with the finite difference time domain (FDTD) technique.

The structures were divided into small reusable components, and the FDTD simulations were used to calculate the s-parameters of each component. Eventually, the device response was calculated by combining the s-parameters of each component in the desired order.

2.1.1 Optical Waveguides

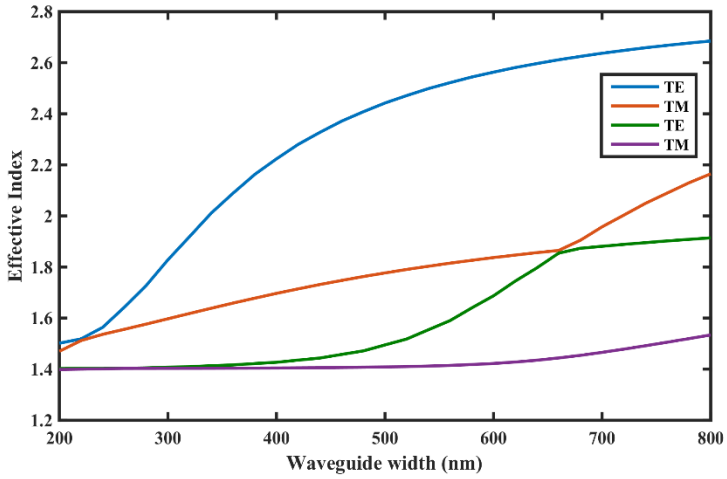

Figure 2.1: Higher order modes cut off for an SOI strip waveguide with varying width and fixed height of 220 nm.

The standard height of a SOI wafer used in the industry is 220 nm, so we have the option to adjust the width of the waveguide to get minimal losses, while remaining in the single mode regime. Figure 2.1 shows the simulated effective indices for various widths of a strip waveguide. The cutoff for four waveguide modes are plotted in the figure. Since we desire to operate at a single mode, we pick the waveguide width to be equal to 500 µms.

2.1.1.1 2D mode profile calculations

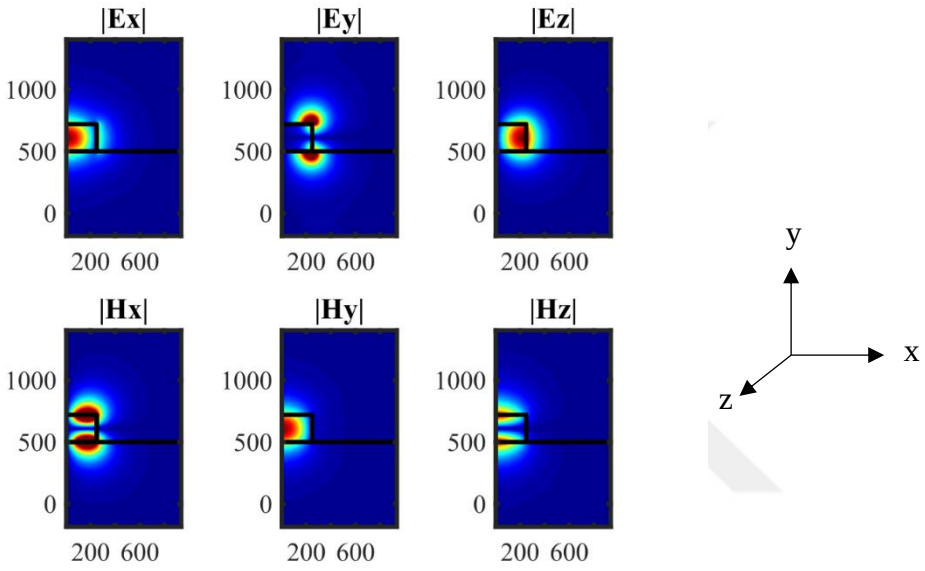

Figure 2.2: E and H field components for the fundamental TE mode of the right half of a strip waveguide (axes are labeled in nm).

In our analysis, we used only the first order quasi-TE mode. To observe the E and H-fields, we perform accurate calculations for the mode profile for the 2D cross-section of the waveguide, by drawing the waveguide, defining the simulation parameters, and solving for the mode solution using the fully vectorial method implemented in Lumerical Mode solutions. We define the width and height of the waveguide to be 500 nm and 220 nm, respectively. The components of E and H fields for the fundamental TE mode are shown in Figure 2.2 (The color scale for Ey, Ez, Hx and Hz fields components are magnified 10 time to make them visible). It is evident that, the mode is not strictly a TE mode, where only the Ex component would be present, but rather is a three-dimensional vectorial field profile. The cross section of a TE mode profile for

a straight strip waveguide with a width of 500 nm and a height of 220 nm on an SOI platform is shown in Figure 2.3.

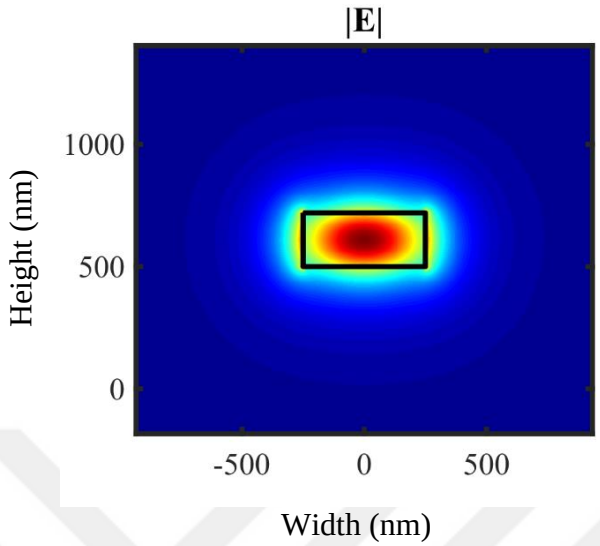

Figure 2.3: Cross section of a strip waveguide showing the total E-field of the fundamental TE mode.

Since the refractive index changes with a change in operating wavelength, the effective refractive index of the 1st order TE mode in the strip waveguide between the wavelength range of 1500 nm to 1600 nm, and with a width × height of 500 × 220 nm, is shown in Figure 2.4. The propagation speed of a pulse is described by the group index as in Eq. (2.1).

$$v_g(\lambda) = \frac{c}{n_g} \tag{2.1}$$

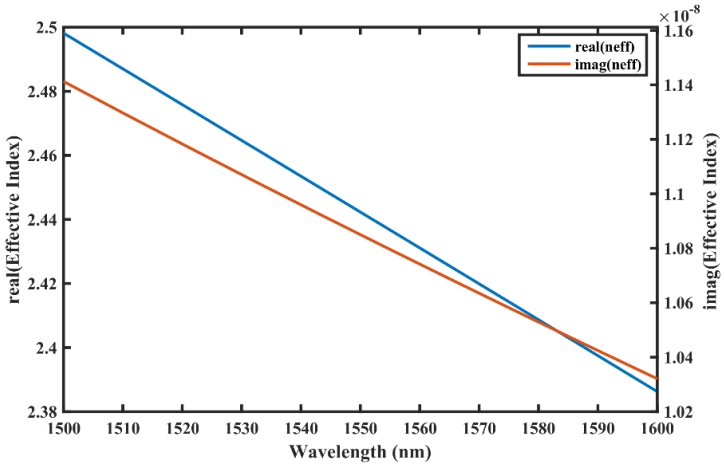

Figure 2.4: The effective refractive index of the 1st order TE mode in a SOI strip waveguide.

Where v_g is the group velocity of the pulse propagating in the waveguide, n_g is the group index and c is the speed of light in vacuum. The group index n_g and the effective index n_{eff} can be related by Eq. (2.2).

$$n_g(\lambda) = n_{eff}(\lambda) - \lambda \frac{dn_{eff}}{d\lambda} \tag{2.2}$$

The group index is the quantity, which determines the speed of the pulse propagating in the waveguide, and this group index is to be used in the calculations for the parameters of resonators, e.g., FSR and optical path lengths.

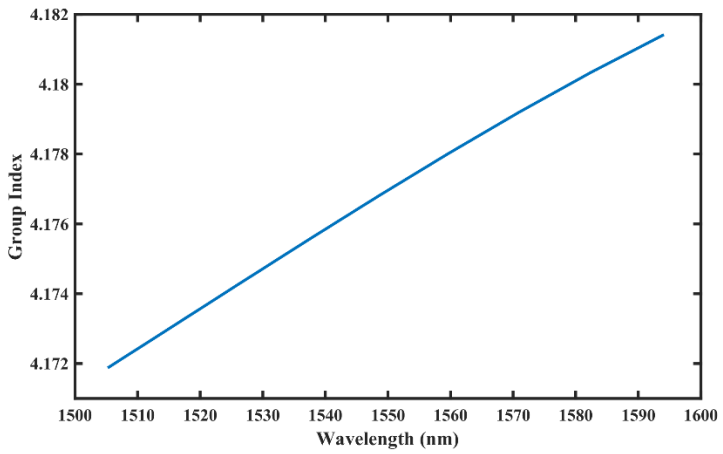

Figure 2.5: The simulated group index of the 1st order TE mode in a SOI strip waveguide.

2.1.1.2 Bends in waveguides:

The mode mismatch loss is the loss in an optical waveguide caused by the mismatch of modes traveling in a bend and a straight waveguide at each transition. The example of a miss matched mode are shown in Figure 2.6 and Figure 2.7.

Figure 2.8 shows the total losses present in a waveguide. These numerical simulations were performed to find the waveguide bending radius, which would produce the minimum loss. As the figure depicts, for bend radii smaller than 5 µm, the mode mismatch loss is the dominating factor, but when the bending radii are greater than 10 µms, the 2 dB/cm propagation losses

surpass the mode mismatch losses, and become the major loss factor. 2 dB/cm propagation losses are plotted for a quarter circle length.

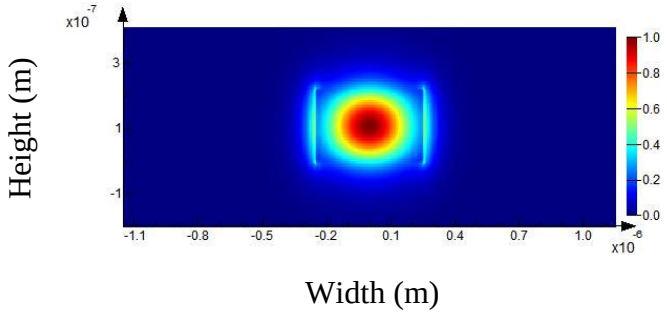

Figure 2.6: Simulated TE mode profile for a straight SOI waveguide with a width of 500 nm and a height of 220 nm.

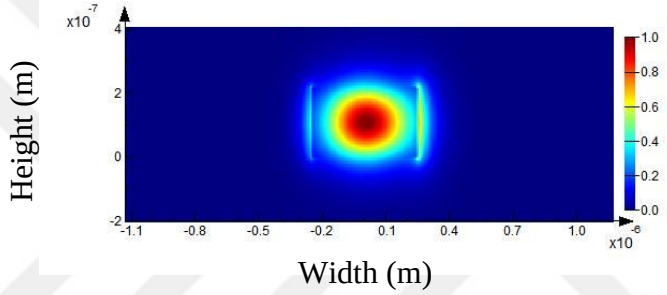

Figure 2.7: Simulated TE mode profile for a bend (towards right side) SOI waveguide with a bend radius of 3 µm width of 500 nm and a height of 220 nm.

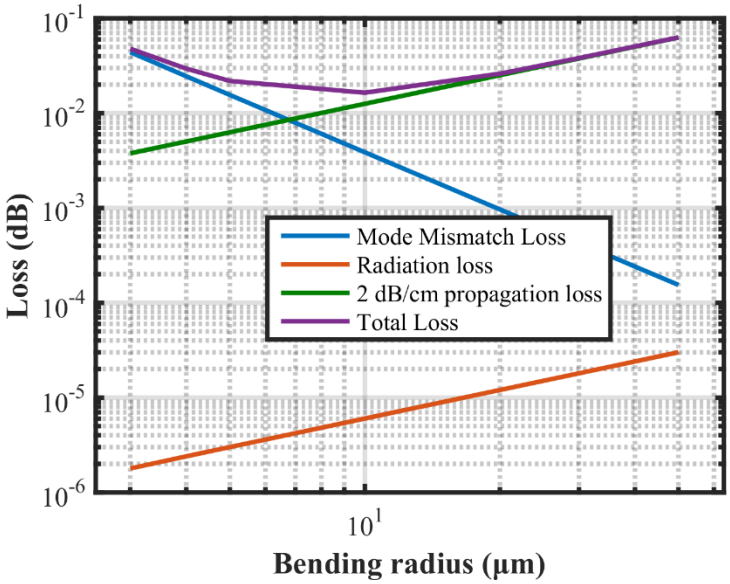

Figure 2.8: Various individual losses and total losses, experienced by the mode traveling in a bend strip waveguide with bending radii from 2 to 50 µm.

2.1.2 Directional coupler (DC)

We used directional couplers (DCs) in designing the MLMs and resonators. In designing DCs, there are two factors, which need to be addressed to achieve the desired coupling. The first factor is the gap between the waveguides, which are to be coupled. The second factor is the interaction length. The power in a DC oscillates between the two waveguides as a function of the coupling length/interaction length, if the gap between the waveguides is constant. For the DCs studied in this research, the gap between the waveguides was keep constant and equal to 200 nm, as shown in Figure 2.9. This value is limited by the resolution of the fabrication process. Numerical simulation results for the DCs with coupling length between 5 µm to 35 µm, and the gap of 200 nm, were calculated for the range of 1500 to 1600 nm.

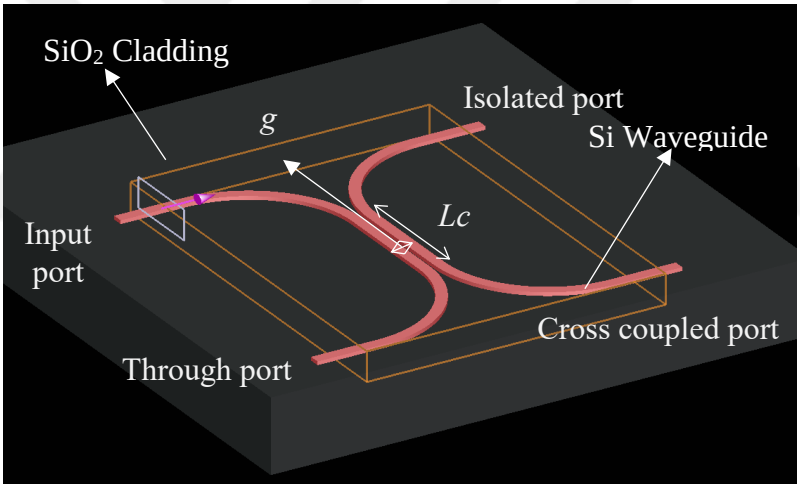

Figure 2.9: Directional coupler (DC) design with a coupling length Lc and a gap g.

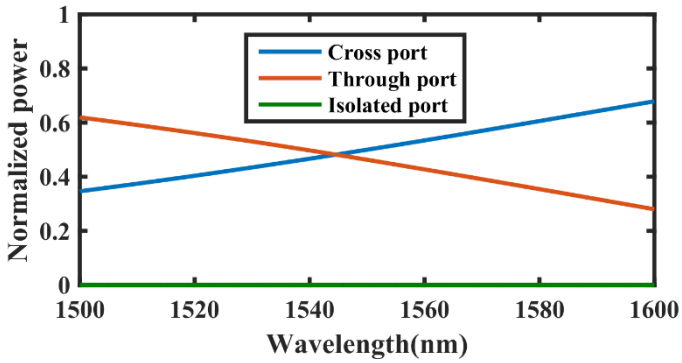

Figure 2.10: Simulation result for a directional coupler of Lc = 17 µm and g = 200 nm.

A typical response of a DC is shown in Figure 2.10. Since the n_{eff} is a function of wavelength, the coupling is also tuned, when the wavelength is tuned from 1500 nm to 1600 nm. At any instance the total power would be the sum of intensities at all three ports. The isolated port remains zero in numerical simulations, but in a fabricated device the isolated port value is greater than zero, since some of the energy in the DC is scattered to the isolated port through the roughness of the side walls.

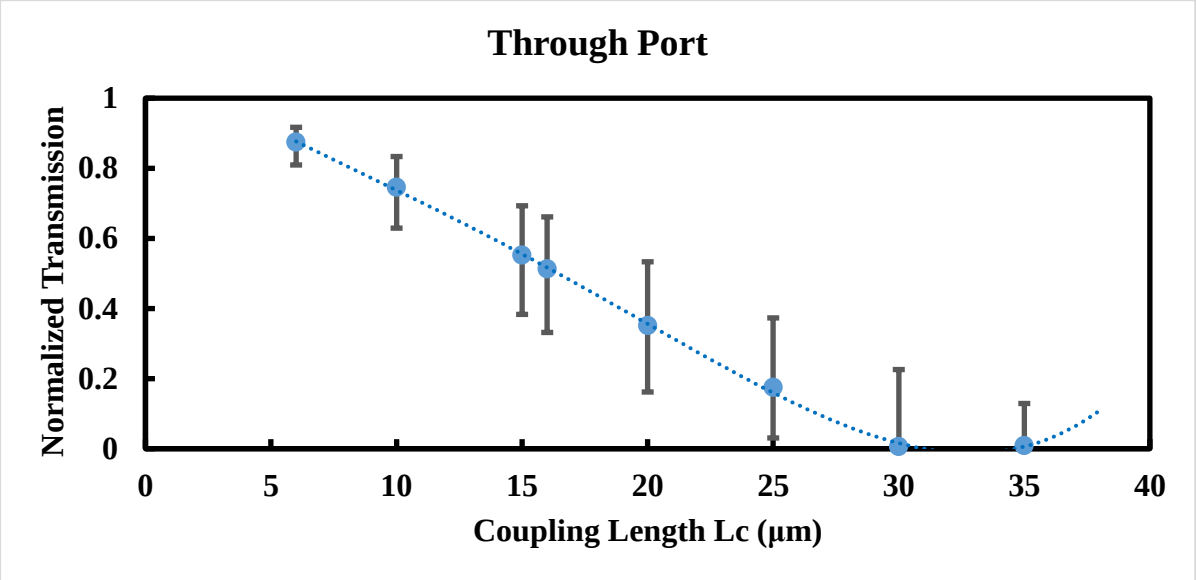

Figure 2.11: Power coupling to the through port of the directional coupler as a function of coupling length Lc.

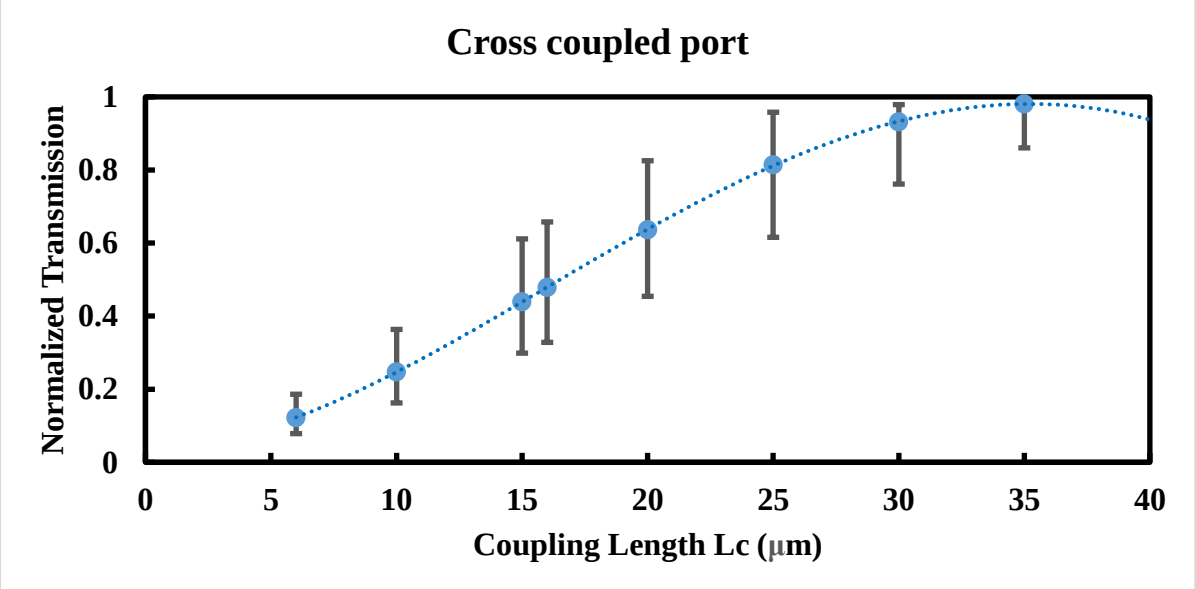

Figure 2.12: Power coupling to the through port of the directional coupler as a function of coupling length Lc.

The power transmitted to the through port and cross coupled ports are shown in Figure 2.11 and Figure 2.12 respectively, at the wavelength of 1550 nm. The error bars show the tuning of coupling for the wavelength range from 1500 nm to 1600 nm. These DCs were chosen for designing the meandering elements because the wavelength sweep would correspond to the tuning due to coupling of the devices.

2.2 Layout Design

2.2.1 Layout versus Schematic

Once a photonic circuit is designed, the designer uses the schematic to layout the photonic components in a physical mask layout using a variety of design aids. This is followed by the verification, including the manufacturing design rule checking (DRC), and the layout versus schematic checking (LVS).

The layouts for this work were designed in Klayout and stored in a graphic data system (GDS) format. [69] A typical schematic-driven design flow includes a schematic, a circuit simulation, a layout, and a verification [6]. The approach taken here is Layout-driven, followed by verification, then a schematic (via a netlist extraction), and simulations [69, 70].

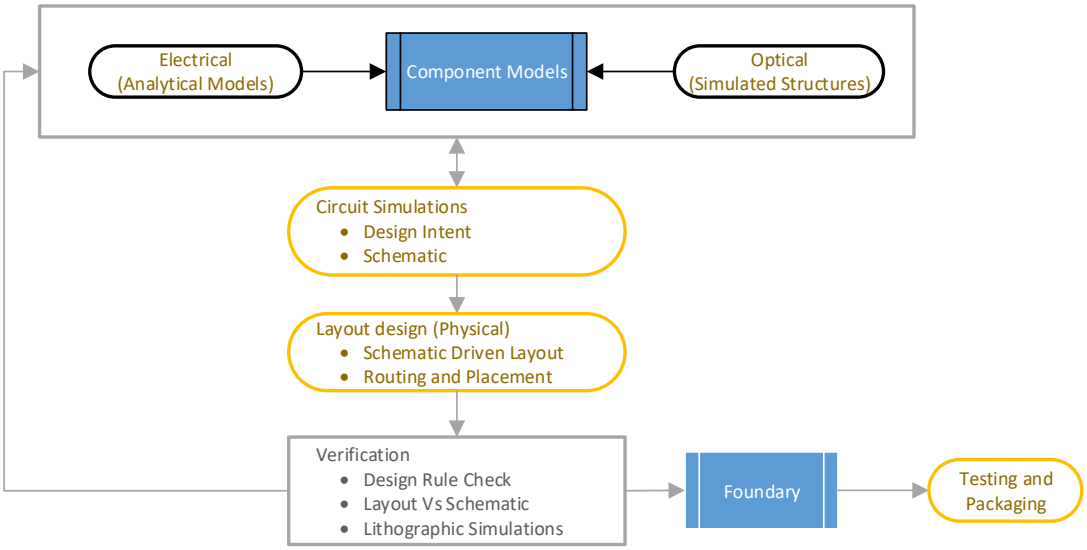

Figure 2.13. Workflow of a typical Si-PIC system design.

2.3 Layout for the devices

2.3.1 De-embedding structure

To calibrate the device under test, we used the de-embedding structure shown in Figure 2.14 to record the overall background response of the system without including the device. The device is placed in the subsequent designs, and eventually the spectrum of the de-embedding structure is decoupled from the measured spectra using signal processing techniques.

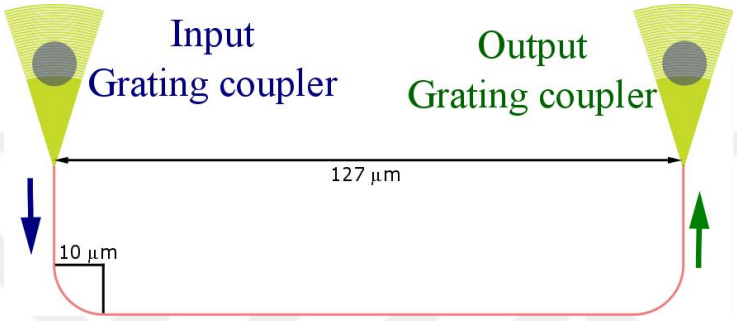

Figure 2.14: Layout design of a de-embedding structure with a grating separation of 127 µm.

The input fiber is brought above the input grating coupler, and the TE mode is coupled from the optical fiber to the SOI waveguide. The beam, after passing through the waveguide, gets coupled to the optical fiber above the output grating coupler, which is then connected to a photodetector to record the transmission measurement.

2.3.2 Meandering loop mirror (MLM)

The optical path length (perimeter) of a meandering loop mirror (MLM), shown in Figure 2.15, can be given as:

$$opl = (MLM\ Lc)\ \times n_g \tag{2.3}$$

$$MLM\ Lc = 2[R(\pi + 1) + 2Lc] + g \tag{2.4}$$

where opl is the optical path length of the device, g = 200 nm the gap between the DC waveguides, R is the bend radius, and n_g the group index of the waveguide for the first order TE mode.

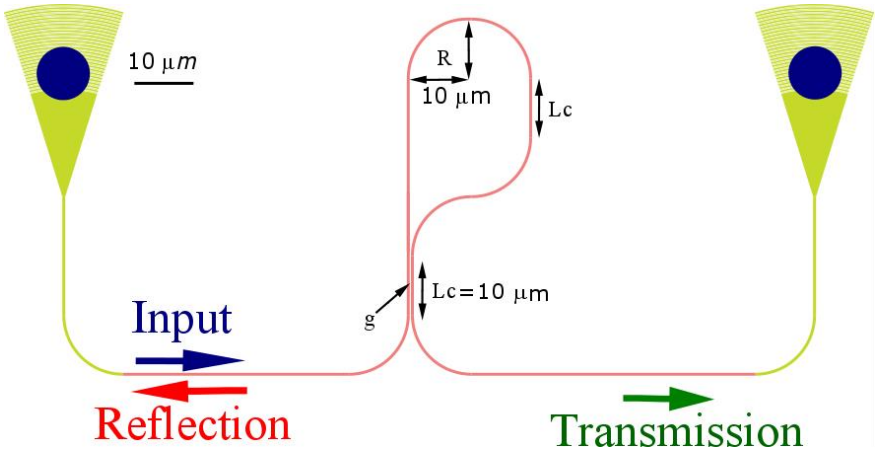

Figure 2.15: Layout of a meandering loop mirror (MLM) with Lc = 10 μm.

2.3.3 Meandering Resonator (MR)

We investigated MRs for the cases, when Lc1 = Lc2 (Symmetric MR) and Lc1 ≠ Lc2 (Asymmetric MR). The geometric path length (perimeter) of a MR is given by (2.5):

$$MR\ Lc1\ vs\ Lc2 = MLM\ Lc1 + MLM\ Lc2 + 2(\pi R + L) \quad (2.5)$$

where g = 200 nm is the gap between the DC waveguides, and L = 25 μm is the waveguide length connecting the two cascaded MLMs as shown in Figure 2.16.

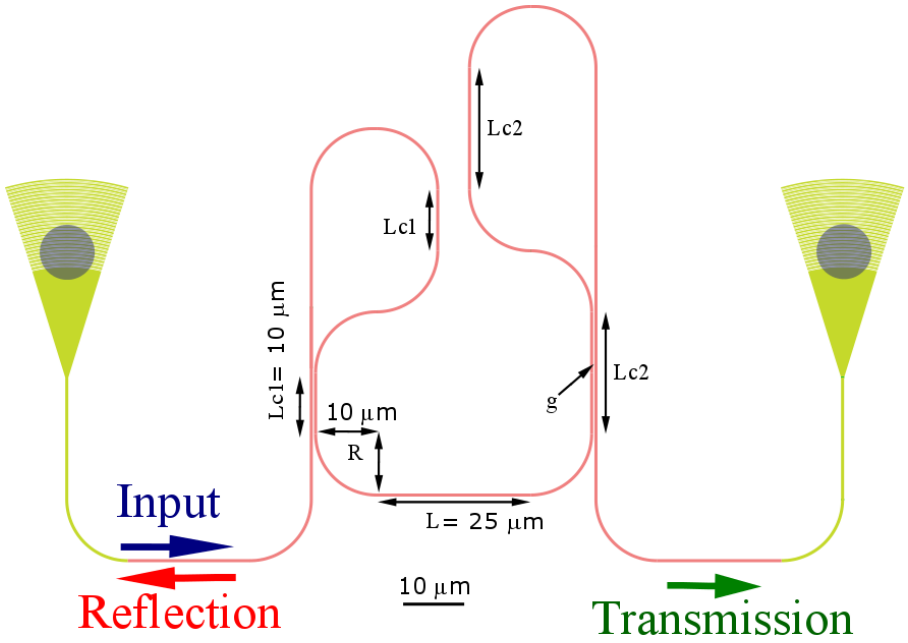

Figure 2.16: Layout design of a MR with Lc1 = 10 μm, Lc2 = 20 μm, L = 25 μm, and R = 10 μm.

2.3.4 Antisymmetric Meandering Resonator (AMR)

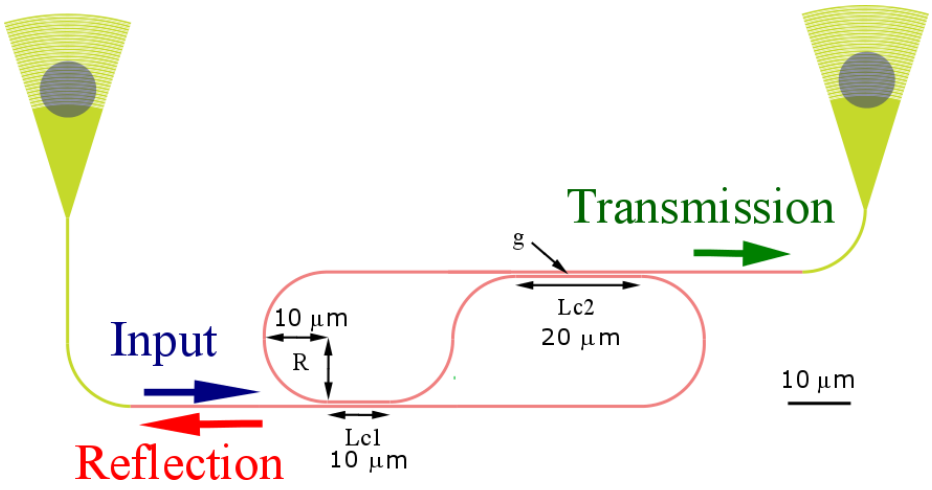

Figure 2.17: Layout design of an AMR with Lc1 = 10 µm, Lc2 = 20 µm and R = 10 µm.

Antisymmetric Meandering Resonator (AMR) is a compact design among the others, as it uses only the footprint of an MLM, with two coupling points, as shown in Figure 2.17. The geometric path length of such a structure is given by:

$$AMR\ Lc1\ vs\ Lc2 = 2((\pi + 2)R + Lc1 + Lc2 + g) \quad (2.6)$$

We investigated AMR for the cases when $Lc1 = Lc2$ and $Lc1 \neq Lc2$.

2.3.5 Symmetric Meandering Resonator (SMR)

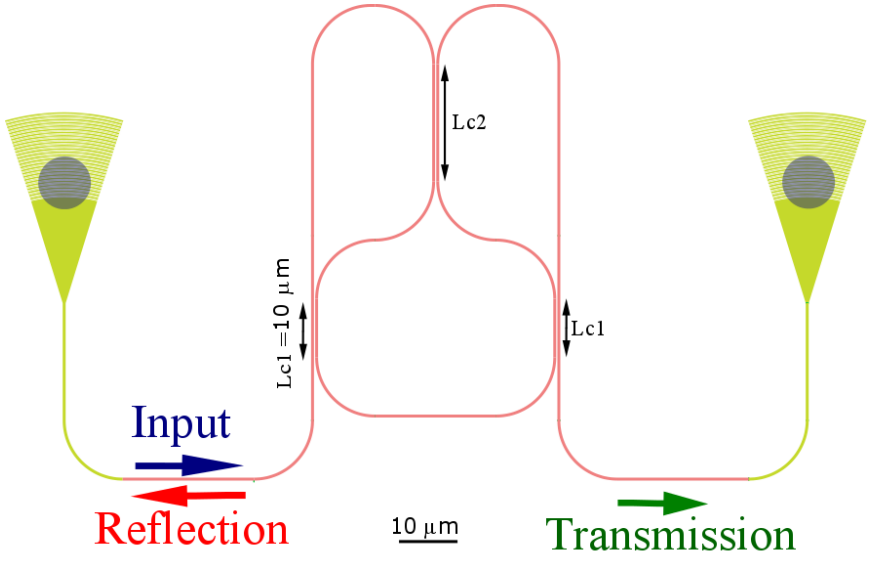

Figure 2.18: Layout design of a SMR with Lc1 = 10 µm, Lc2 = 20 µm and R = 10 µm.

Figure 2.18 shows a layout of a symmetric meandering resonator (SMR), where, Lc1 and Lc2 are the coupling lengths of the DCs. R are the bending radii, which for our case are equal to 10 µm. SMR can be treated as a higher order AMR. We have investigated SMR for the cases, when $Lc1 = Lc2$ and $Lc1 \neq Lc2$. A sample layout is shown in Figure 2.19.

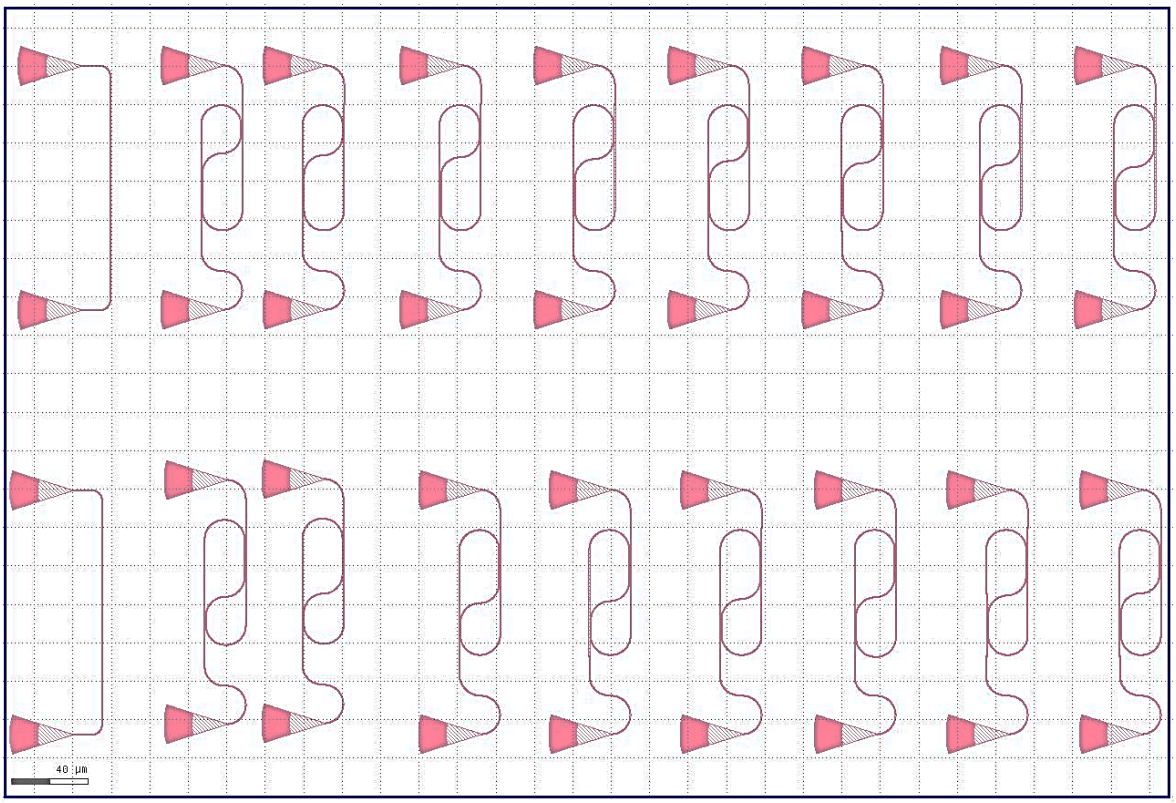

Figure 2.19: An area of 605 X 410 µm^2 on the chip with AMR variations and two de-embedding structures.

2.4 Fabrication

For fabricating our devices, we used e-beam lithography. Since the chips were manufactured by two different foundries, the specifications and processes details for each are provided in the following section.

2.4.1 General e-beam process steps

We used Soitec UNIBOND 6" Prime grade SOI wafers, with a silicon thickness of 220 nm, with a 6 sigma of 22.3 nm, and buried oxide (BOX) thickness of 3.017 µm, with a 6 sigma of 6 nm.

Figure 2.20 shows the general process steps involved in e-beam lithography.

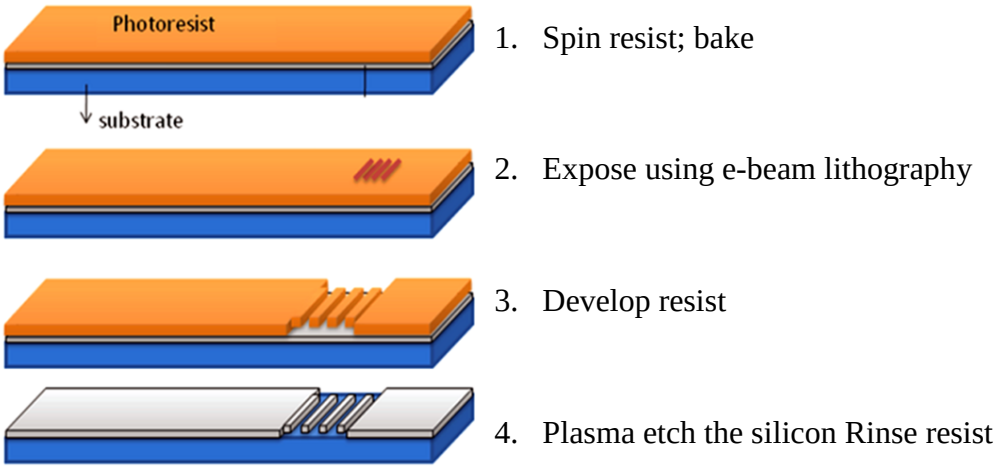

Figure 2.20: General process steps involved in e-beam lithography and fabrication.

The following are the optional steps and can vary per application requirements.

- SEM mid-process imaging,
- Deposition of oxide to cover the waveguide,
- Dicing and packaging of the chips,
- Testing.

Chips were fabricated at two foundries:

- Applied Nanotools (ANT), Inc.
- University of Washington (UW), Washington Nanofabrication Facility (WNF).

The following are the process descriptions. The details of the fabrication process, and the steps involved by the foundries involved in fabricating the devices are mentioned in the following sections.

2.4.2 Applied Nanotools (ANT), Inc. NanoSOI process:

The photonic devices were fabricated using the NanoSOI MPW fabrication process by Applied Nanotools Inc. [71], which is based on direct-write 100 keV e-beam lithography technology. Silicon-on-insulator (SOI) wafers of 200 mm diameter, 220 nm device thickness, and 2 µm buffer oxide thickness are used as the base material for the fabrication. The wafer was prediced

into square substrates with dimensions of 25 mm x 25 mm, and lines were scribed into the substrate backsides to facilitate easy separation into smaller chips once the fabrication was complete. After an initial wafer clean using piranha solution (3:1 H_2SO_4:H_2O_2) for 15 minutes and water/isopropyl alcohol (IPA) rinse, hydrogen silsesquioxane (HSQ) resist was spin-coated onto the substrate and heated to evaporate the solvent. The photonic devices were patterned using a Raith EBPG 5000+ e-beam instrument using a raster step size of 5 nm. The exposure dosage of the design was corrected for proximity effects, which result from the backscatter of electrons from exposure of nearby features. Shape writing order was optimized for efficient patterning and minimal beam drift. After the e-beam exposure, and subsequent development with a tetramethylammonium sulfate (TMAH) solution, the devices were inspected optically for residues and/or defects. The chips were then mounted on a 4" handle wafer and underwent an anisotropic inductively coupled plasma-reactive ion etching (ICP-RIE) process using chlorine after qualification of the etch rate. The resist was removed from the surface of the devices using a 10:1 buffer oxide wet etch, and the devices were inspected using a scanning electron microscope (SEM) to verify patterning and etch quality. A 2.2 μm oxide cladding was deposited using a plasma-enhanced chemical vapour deposition (PECVD) process based on tetraethyl orthosilicate (TEOS) at 300ºC. Reflectrometry measurements were performed throughout the process, to verify the device layer, buffer oxide, and cladding thicknesses, before delivery.

2.4.3 University of Washington (UW), Washington Nanofabrication Facility (WNF) silicon photonics process:

The devices were fabricated using 100 keV e-beam lithography [72, 73]. The fabrication used an SOI wafer with a 220 nm thick silicon on 3 μm thick silicon dioxide. The substrates were 25 mm x 25 mm squares diced from 150 mm wafers. After a solvent rinse, and hot-plate dehydration bake, hydrogen silsesquioxane resist (HSQ, Dow-Corning XP-1541-006) was

spin-coated at 4000 rpm, then hotplate baked at 80 °C for 4 minutes. E-beam lithography was performed using a JEOL JBX-6300FS system operated at 100 keV energy, 8 nA beam current, and 500 μm exposure field size. The machine grid used for shape placement was 1 nm, while the beam stepping grid, the spacing between dwell points during the shape writing, was 6 nm. An exposure dose of 2800 μC/cm^2 was used. The resist was developed by immersion in 25% tetramethylammonium hydroxide (TMAH) for 4 minutes, followed by a flowing deionized water rinse for 60 s, an isopropanol (IPA) rinse for 10 s, and then blown dry with nitrogen. The silicon was removed from unexposed areas using inductively coupled plasma (ICP) etching in an Oxford Plasmalab System 100, with a chlorine gas flow of 20 sccm, pressure of 12 mT, ICP power of 800 W, bias power of 40 W, and a platen temperature of 20 °C, resulting in a bias voltage of 185 V. During etching, chips were mounted on a 100 mm silicon carrier wafer using perfluoropolyether vacuum oil. The cladding oxide was deposited using plasma enhanced chemical vapor deposition (PECVD) in an Oxford Plasmalab System 100 with a silane (SiH4) flow of 13.0 sccm, nitrous oxide (N2O) flow of 1000.0 sccm, high-purity nitrogen (N2) flow of 500.0 sccm, pressure at 1400 mT, high-frequency RF power of 120 W, and a platen temperature of 350 ˚C. During deposition, the chips rest directly on a silicon carrier wafer, and are buffered by silicon pieces on all sides to aid uniformity. After the lithography process we were able to achieve a sidewall angle 82º for the waveguides and a minimum isolated feature size of 60 nm.

2.4.4 Scanning electron microscopy (SEM)

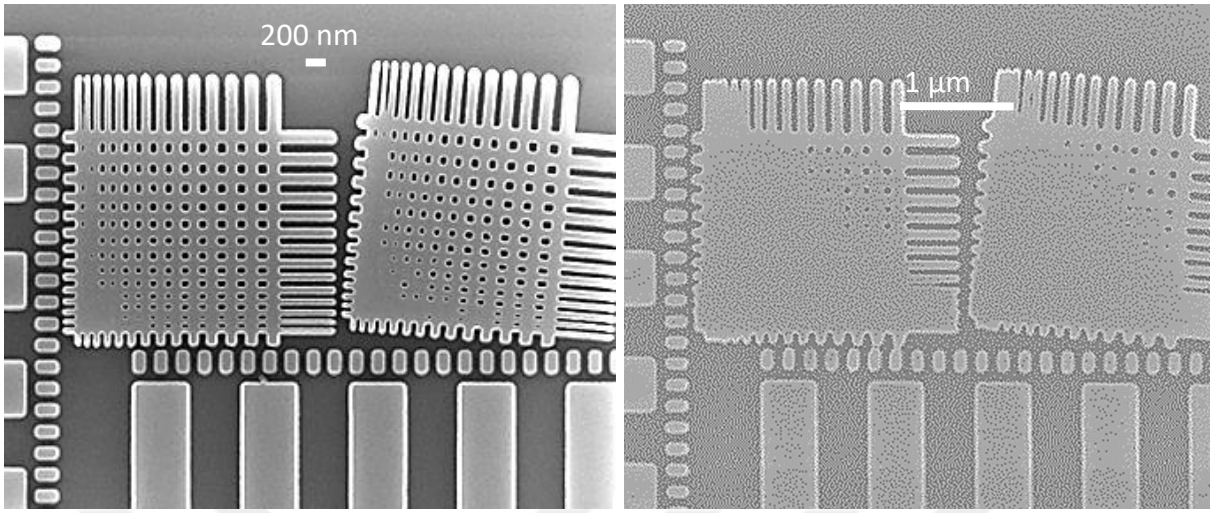

Figure 2.21: Fabrication characterization patterns from ANT-2 (left) and UW-1 (right) chips.

Dummy patterns are etched on the wafer to characterize the fabrication process and see the minimum resolvable feature sizes during a fabrication run. Figure 2.21 shows the SEMs of such patterned structures on the chips fabricated by ANT and UW. ANT has a better resolution as compared to UW process, as it is able to resolve smaller feature sizes.

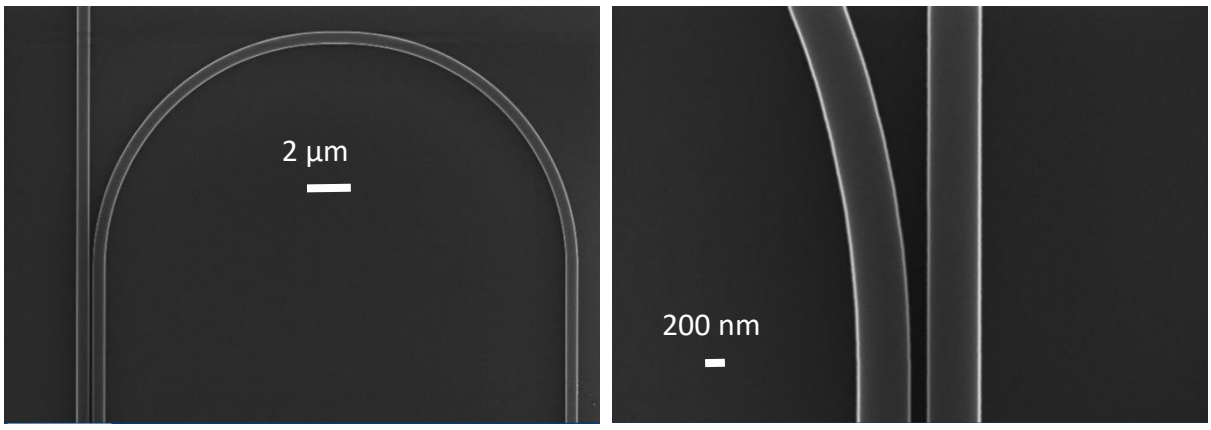

Figure 2.22: DC waveguide bend SEMs fabricated in ANT.

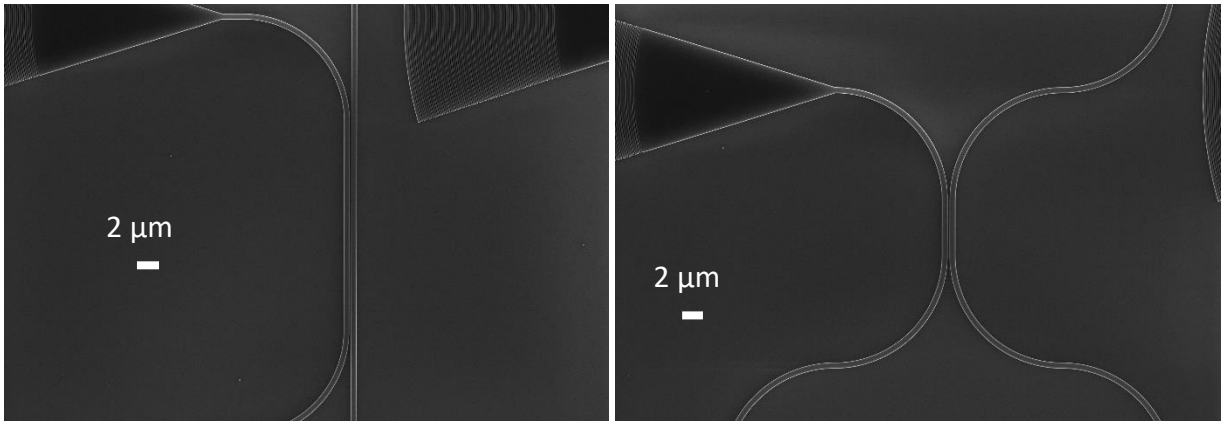

Figure 2.23: DC SEMs.

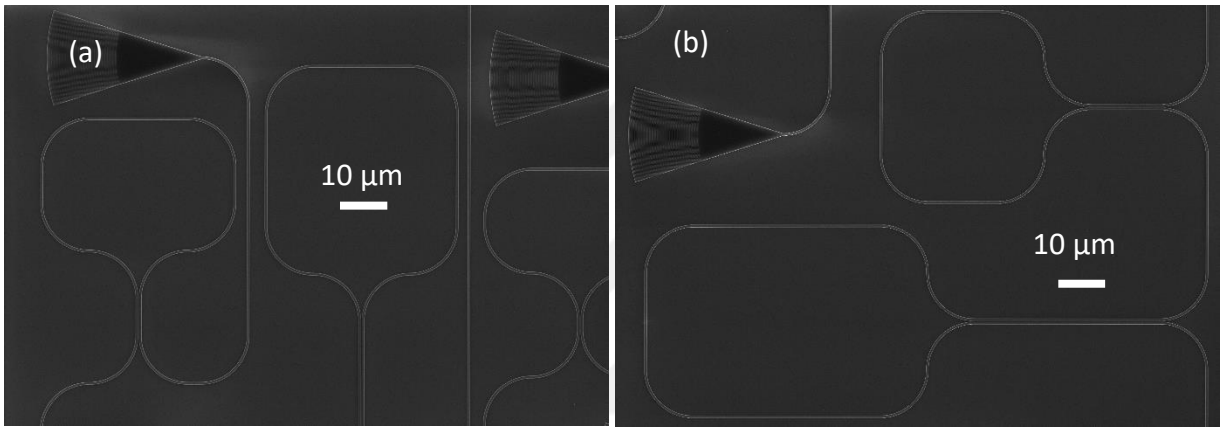

Figure 2.24: (a) MLM SEM (b) MR SEM.

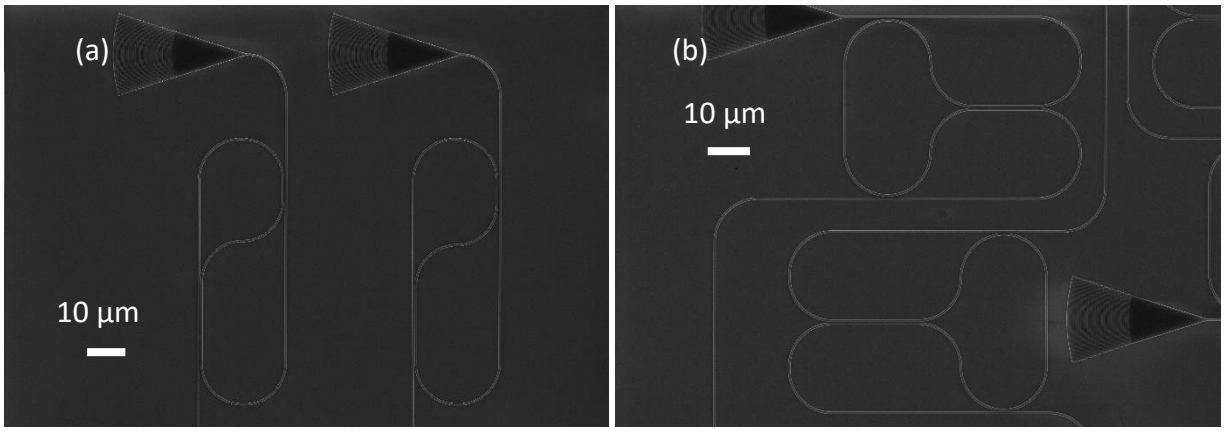

Figure 2.25: (a) AMR SEM (b) SMR SEM.

2.4.5 Variations in Fabrication

Since the optical systems are prone to fabrication variations, in our analysis, we accommodated for the following variations.

- Intra-Chip (device replicas developed on the same chip)
- Inter-Fab (multiple devices developed in the same Fab. on multiple chips)
- Intra Fab (same layouts developed in different Fab)
- Temperature variations (Recorded same device spectra at different temperatures)

To study the thermal response of the devices manufactured on an SOI, we recorded the measurements at different temperatures.

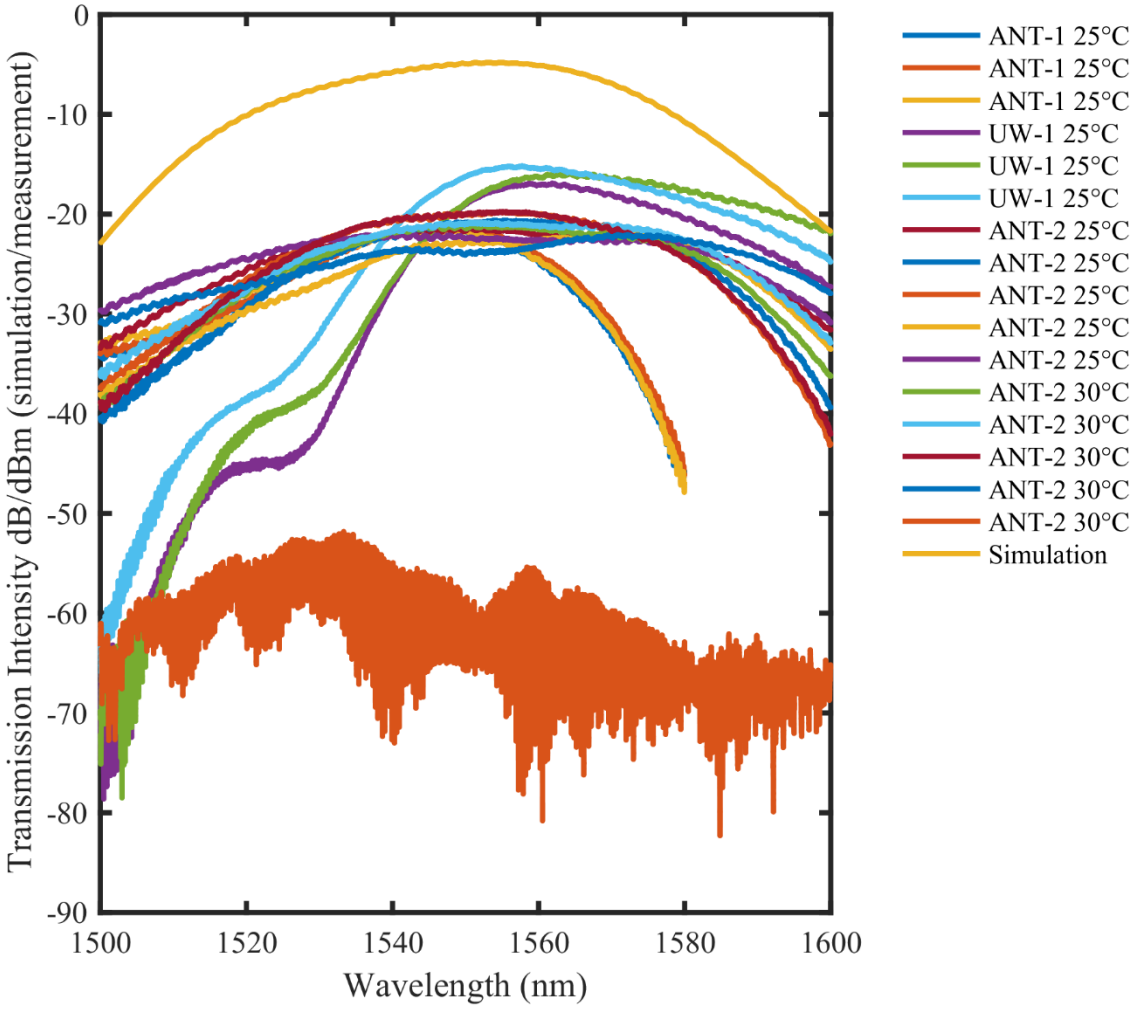

Figure 2.26: Spectral variations of a de-embedding structure due to fabrication imperfections and thermal variations.

Figure 2.26 captures the deviations in the spectrum of a waveguide coupled to a grating shown in Figure 2.27 due to fabrication imperfections and thermal drifts. The spectral responses can

vary significantly, which can affect the yield of the Si-PIC process. To overcome these variations, we need to increase the resolution of the fabrication processes.

2.5 Near-Infrared Spectral Measurements

2.5.1 Measurement Setup:

To characterize the devices, a custom-built automated spectroscopy setup [6, 74] with automated control software written in Python was used [75]. An Agilent 81600B tunable laser was used as the input source, and an Agilent 81635A optical power sensor as the output photodetector. The wavelength was swept from 1500 nm to 1600 nm in 10 pm steps. Polarization-maintaining (PM) optical fiber technology was used to maintain the polarization state of the light, to couple in TE polarization into the grating couplers [38]. A polarization maintaining fiber array was used to couple light in/out of the photonic chip [76].

2.6 General Analysis steps

2.6.1 Characterization

2.6.1.1 Grating background removal

This is an alternative approach, we used to extract the figures of merits for our devices. First step to remove the background was to fit a lower, e.g., 5^{th} order polynomial to the spectrum. The fitted polynomial was then subtracted from the device spectra, finally the DC offset is removed. This process is relatively easy, and fast and was used initially to extract the general behavior of the devices. For calibration, we used the process explained in the next section.

2.6.1.2 Near-IR Spectrum calibration

To calibrate the device under test, we used the de-embedding structure shown in Figure 2.14 to record the overall background response of the system without including the device. The device is placed in the subsequent designs, and eventually the spectrum of the de-embedding structure is decoupled from the measured spectra using signal processing techniques.

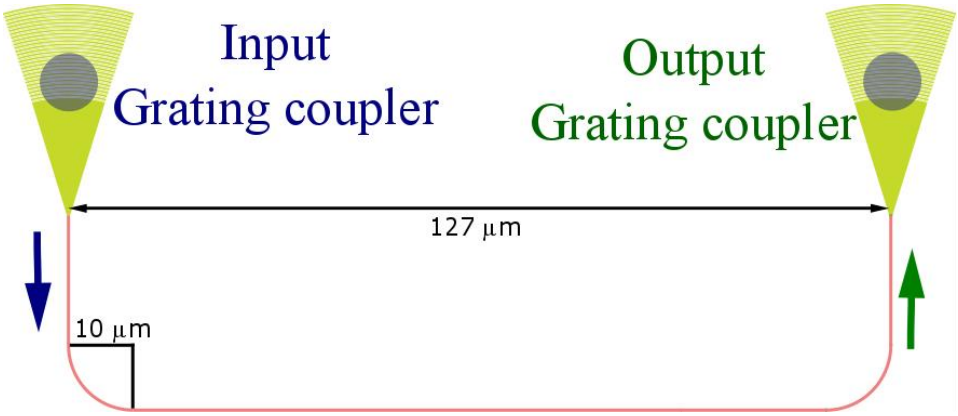

Figure 2.27: Layout design of a de-embedding structure with a grating separation of 127 µm.

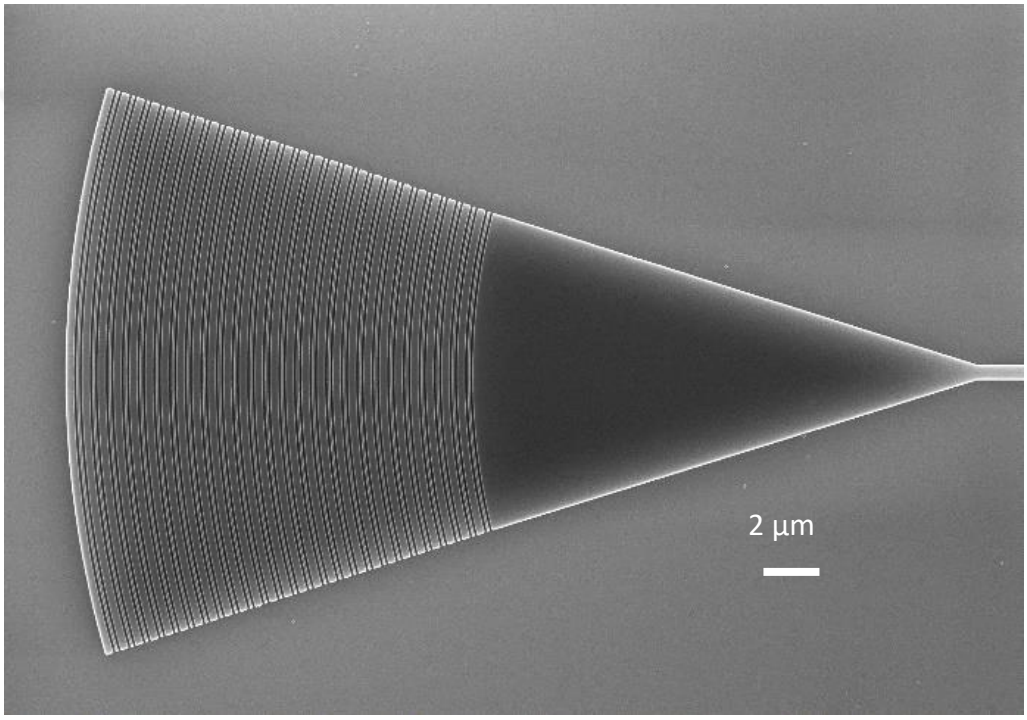

Figure 2.28 SEM of the grating structure with a grating separation of 127 µm.

2.6.2 Figures of merit

To characterize our photonic devices, we have used the figures of merit described in the subsequent sections, with respect to the Fabry–Pérot resonator [43]. Consider a Fabry–Pérot etalon with a slab thickness d, and refractive index *n*, as shown in Figure 2.29. The transmission and reflection for Fabry–Pérot etalon are also plotted in Figure 2.29.

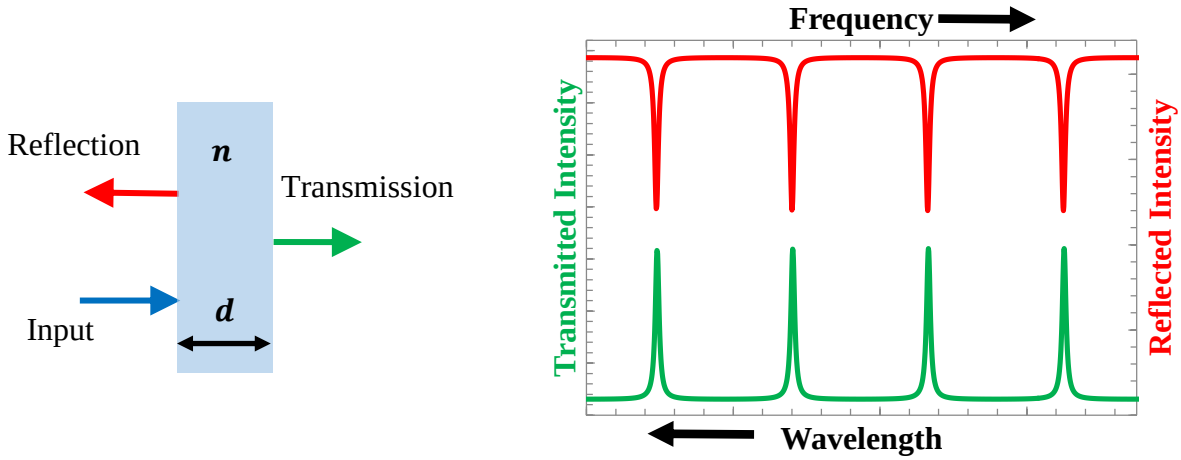

Figure 2.29: Block diagram of a Fabry–Pérot etalon with the reflection and transmission spectra.

2.6.2.1 Quality Factor

The Q-factor is a parameter that relates the stored and dissipated energies of an oscillatory system.

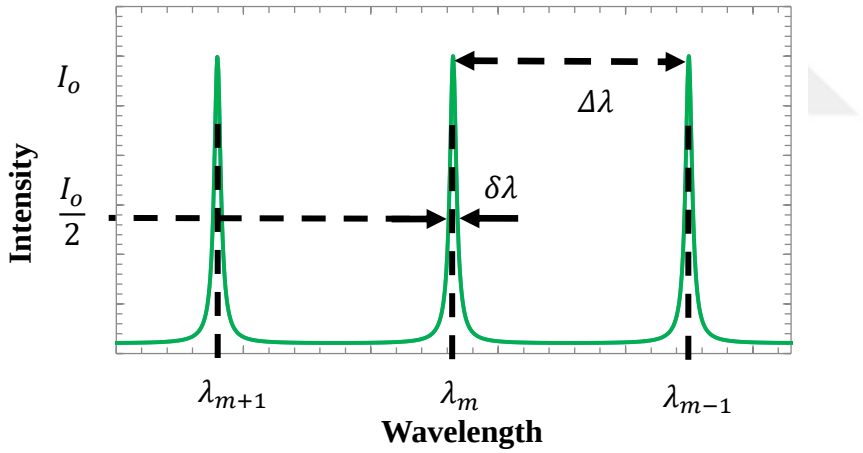

Figure 2.30: Transmission spectrum of a Fabry–Pérot etalon plotted with respect to wavelength.

$$Q = \frac{\lambda_m}{\delta\lambda} \tag{2.7}$$

where λ_m the resonant wavelength of the m^{th} mode, $\delta\lambda$ also known as the full-width-half-maximum (FWHM) is the wavelength band around the resonant wavelength, λ_m, where the transmission intensity value drops to half compared to its peak value. In a Fabry-Pérot etalon,

a peak is observed in the transmission intensity, and a dip is observed in the reflection intensity at $\lambda_m$condition.

2.6.2.2 Free spectral range (FSR)

The free spectral range (FSR) is an important parameter of a resonator device. It is a measure of the optical bandwidth between two successive resonant conditions

$$FSR = \Delta\lambda \approx \frac{\lambda^2}{opl} \tag{2.8}$$

$$opl = n\,L \tag{2.9}$$

where, c is the speed of light in vacuum, n the refractive index of the material, opl the optical path length of the resonator, and L the total length of the resonator, which is $2d$ for the Fabry-Pérot resonator in Figure 2.29. Round trip time T_R, is the inverse of FSR. Alternatively, the FSR can be approximated to the following formula in terms of wavelength.

2.6.2.3 Finesse (F)

The finesse relates the $\Delta\lambda$ (FSR) to the $\delta\lambda$ (FWHM) by the following expression:

$$F = \frac{\Delta\lambda}{\delta\lambda} \tag{2.10}$$

2.6.2.4 Extinction ratio

In an optical system, the extinction ratio (ER) is the ratio of two optical power levels. For the case of Fabry-Pérot resonator, ER can be defined as the peak transmission intensity (on resonance condition) to the minimum transmission intensity (off resonance condition).

$$ER = \frac{I_o}{I_{min}} \tag{2.11}$$

3 Near-IR Spectral Response and Structural Analysis

In this section, we present our measurement spectra and compare them with the simulations, to account for the variations, which may have occurred due to the fabrication imperfections.

First, we analyze the wavelength dependence of a directional coupler (DC), since the DC is one of the basic elements used in our designs. We look at the coupled and the transmitted port intensities of the DC and compare them with the spectral measurement results.

Then, we look at the meandering loop mirror (MLM) response, which is composed of a DC, and study the effects of such a mirror under varying wavelengths.

After developing the basic understanding of DC and the MLM, we move to the next step and analyze the spectral responses of more complex structures, e.g., MR, AMR, and SMR.

To understand the actual spectral response, we first analyze the simulated spectra, for the device under test. Since the input and outputs of the devices had to be connected to the grating couplers, to couple in and out from the optical fibers, the measurement responses are always modulated by the coupler responses, and thus cannot be directly compared to the simulations. To make our simulation spectra comparable to the measurement spectra, we also simulated the transmission spectra of the devices including the grating couplers.

To make the results more reader friendly all the spectra are color coded: the normalized transmission intensity (excluding grating couplers) are plotted in brown, the transmission intensity in logarithmic scale (dB) (excluding grating couplers) are plotted in red, the

transmission intensity in logarithmic scale (dB) (including grating couplers) are plotted in blue, whereas the transmission intensity (including grating couplers) are plotted in green.

3.1 Meandering loop mirror (MLM)

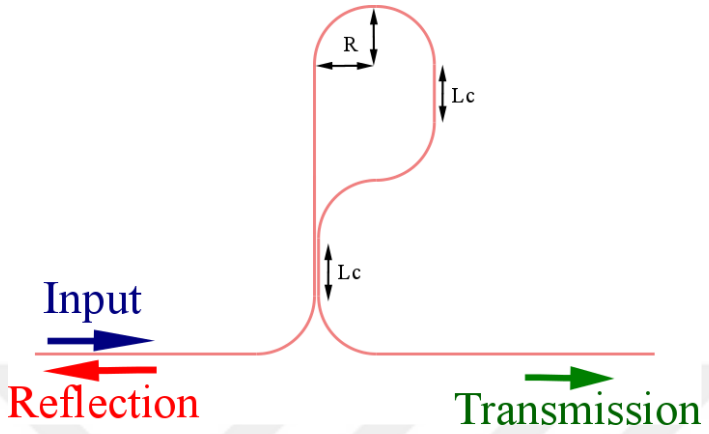

Figure 3.1: MLM consisting of a coupler of length Lc and bending radii of R.

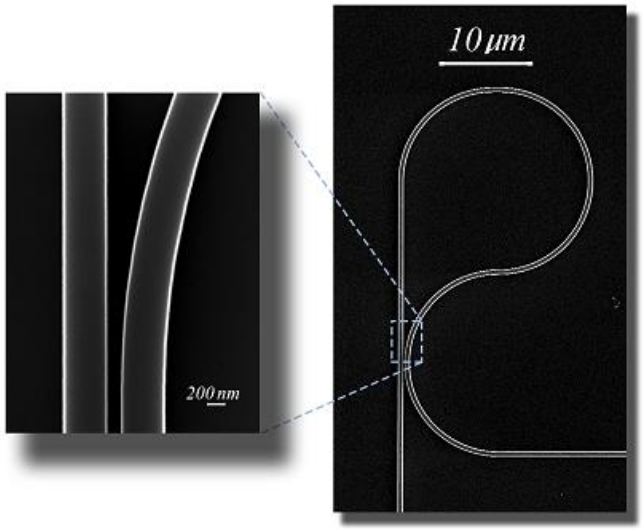

Figure 3.2: MLM SEM.

Figure 3.1 and Figure 3.2 show a schematic diagram and the SEM of a meandering loop mirror **MLM Lc** structure respectively, where Lc is the coupling length of the directional coupler, R the bending radius of the waveguide, in our designs we kept R as 10 μm. We studied the effects of variations of the DCs coupling lengths on the transmission spectra of the MLM, whereas the gap between the coupling waveguides was kept constant at 200 nm. We simulated and fabricated the MLMs with coupling lengths from 0 μm to 40 μm with a step size of 1 μm.

The optical path length (perimeter) of such an MLM can be given as

$$MLM\ Lc = 2[R(\pi + 1) + 2Lc] + g \quad (3.1)$$

Figure 3.3 show the simulation results of de-embedding structure with input and output grating couplers and MLM 10 with and without input and output grating couplers, respectively. The resonance observed in the simulated de-embedding structure is due to the FP effect created by the reflections from the input and the output grating couplers. The free spectral range (FSR) for the simulated structure is 1.88 nm, which matches with the theoretical FSR value of 1.9 nm for a waveguide length of 160 μm with a group index of 4.

The interference in MLM 10 (excluding grating) structure creates a pattern with a simulated FSR of 4.3 nm. Since the dynamic range of the interference is small compared to the FP effect, the change produced by this effect is not making a significantly visible modulation in the spectrum.

The FP effect in MLM 10 (with gratings) with a smaller FSR of 1.6 nm is due to the reflections from the gratings. The FSR is smaller than the de-embedding structure's FSR of 1.8 nm, because of longer optical path length introduced by the MLM 10 itself.

The larger FSR modulated on top of the smaller FSR in MLM 10 (with grating) is due to the FP effect created by the reflections by the grating coupler and the MLM itself. The simulated FSR value is around 9 nm which corresponds to a theoretical FSR created by an optical path length of approximately 70 um, which corresponds to the a physical distance of the MLM placed in between the input and the output grating couplers.

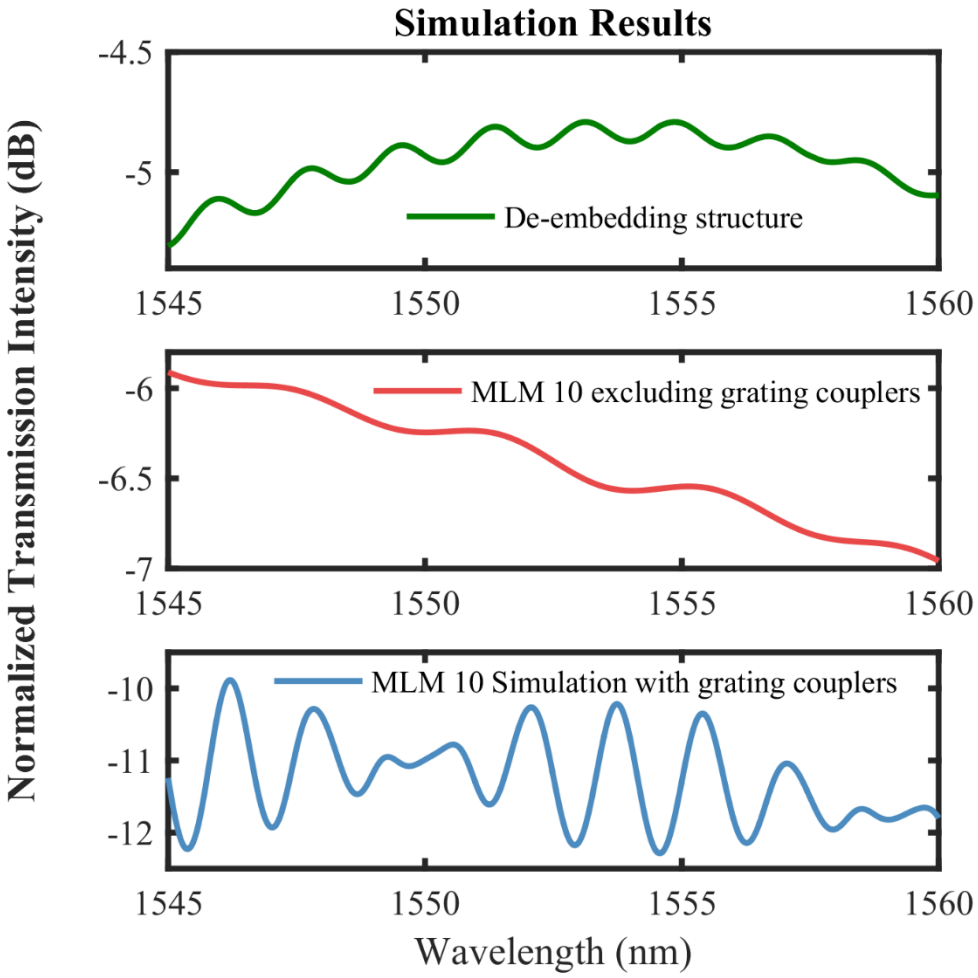

Figure 3.3: Simulation results of de-embedding structure with input and output grating couplers and MLM 10 with and without input and output grating couplers respectively.

The plots in Figure 3.4 and Figure 3.5 show the simulation results for the transmission intensities in normalized and decibel (dB) scales, for the MLM structures with coupling lengths from 10 μm to 20 μm. The dB scale is used to make the dips more prominent as is the case in the Figure 3.5. The general response of a tunable mirror is observed, where the dip corresponds to the maximum reflectivity of the mirror. The dotted red line indicates the shift of the dip position, when the coupling length is varied. The wavelength range of 1500 nm to 1600 nm was used in our analysis.

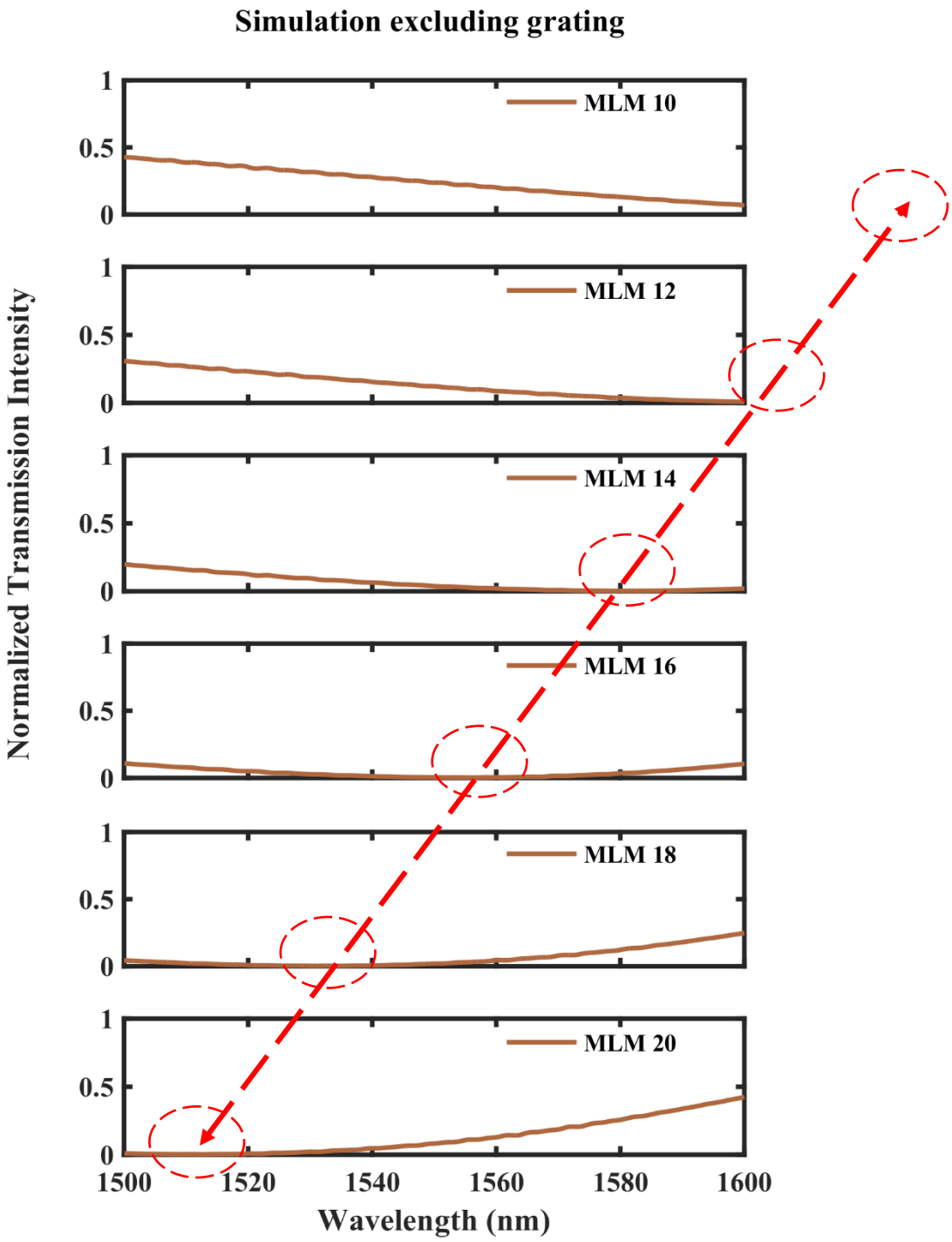

Figure 3.4: Simulation: Normalized transmission intensities of meandering loop mirrors with coupling lengths varying from 10 μm to 20 μm.

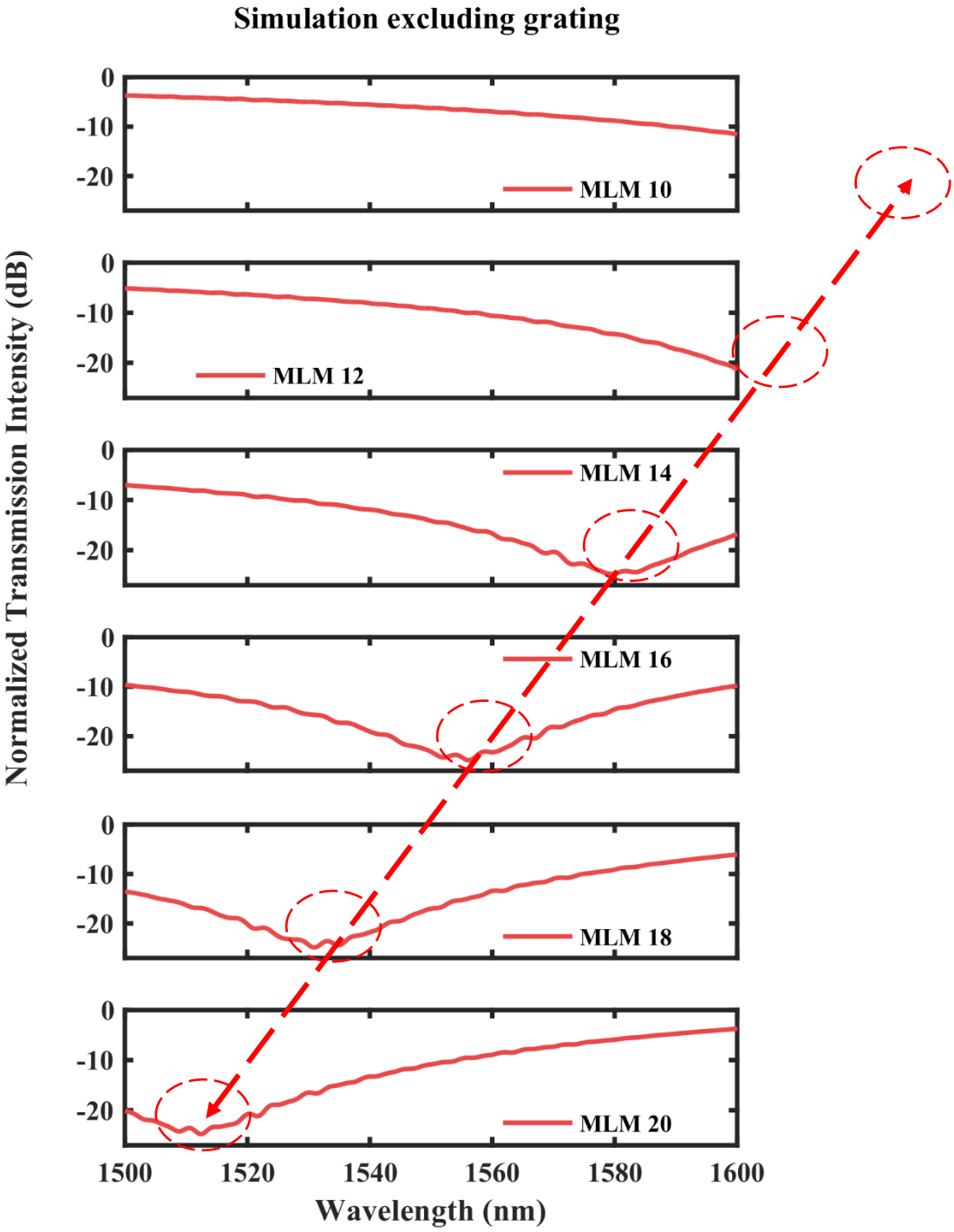

Figure 3.5: Simulation: Normalized transmission intensities in decibel scale (dB) of meandering loop mirrors with coupling lengths varying from 10 μm to 20 μm.

Since the fabricated devices were connected to the grating couplers to couple the light, in and out of the waveguide, the device response was modulated with a grating response. Figure 3.6 shows the modulated device response with the grating couplers. The grating response is shown in Figure 2.26.

We located the dip position moving from 1610 nm in MLM 12 to around 1510 nm in MLM 20. At this dip, the reflectance of the MLM reaches the maximum value, and only a small portion of the input beam is propagated through to the output port. We compared the simulation results in Figure 3.6 to the measurement results in Figure 3.7. The position of the dip can be located at 1610 nm in MLM 12 and moves to 1510 nm in MLM 20. These results correspond well with the simulated results.

In Figure 3.8 and Figure 3.9, we plotted the normalized transmission intensities for the simulated case, and the received transmission intensities for the fabricated case, respectively. The dips can be located in both the cases and are indicated with a dashed red line. The slope of the mentioned line indicates that the dip is moving to the lower wavelengths (blue shifting) as the coupling length is increased from 10 μm to 20 μm.

Figure 3.10 and Figure 3.11, show the normalized transmission intensities, and transmission intensities in dB scale respectively, of the MLM with the coupling lengths varying from 10 μm to 40 μm. The peaks in MLM 25 to MLM 40 correspond to the region, where the MLM has the minimum reflectance. Contrary to the dips, the peaks are more prominent in the normalized transmission intensities, and are indicated by a dashed green line. The two different slopes, i.e., the dashed red line, and the dashed green line, indicate that, the coupler is mismatched and the chirp is observed in the coupling [77]. The coupling will oscillate faster, if the couplers length are increased further.

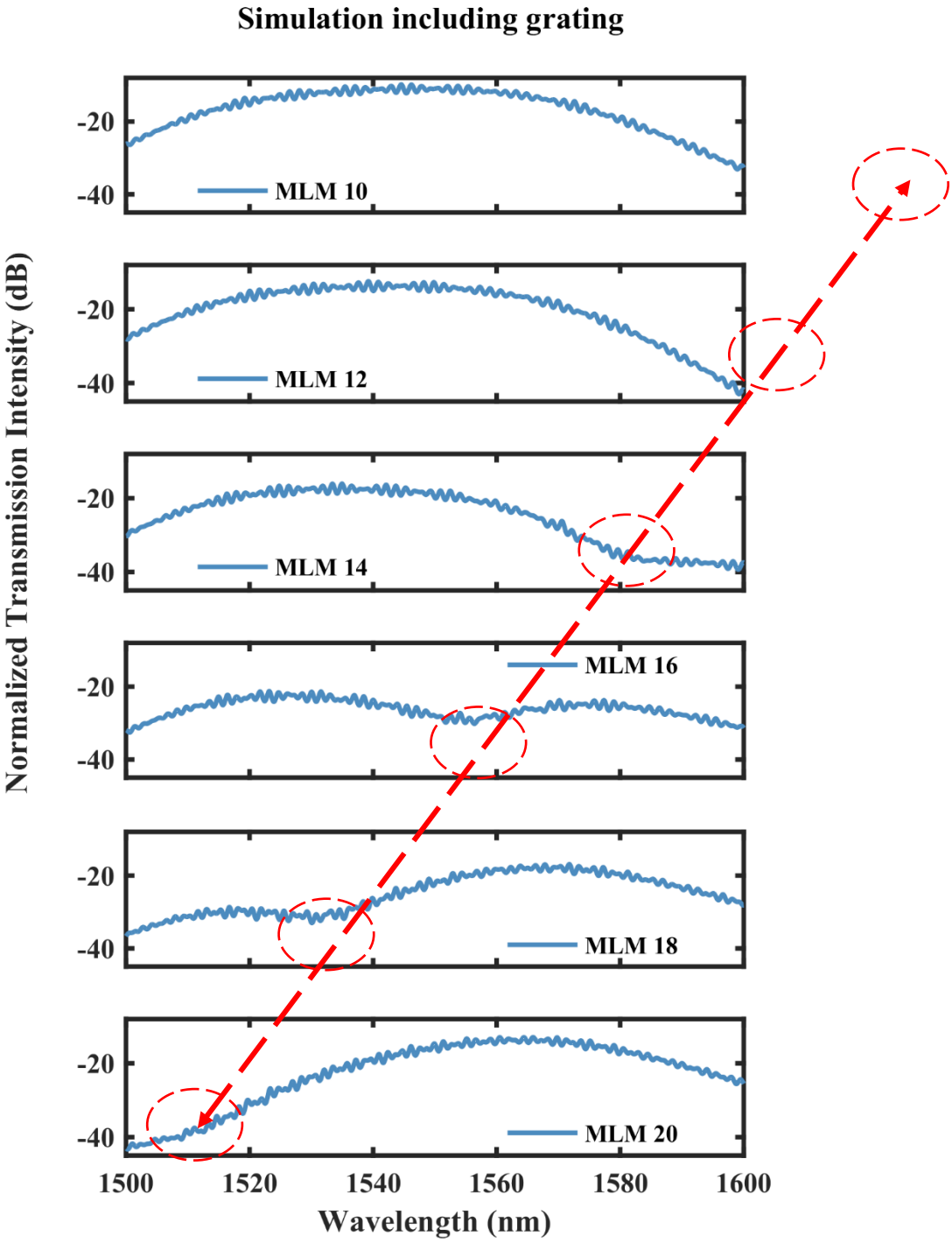

Figure 3.6: Simulation: Normalized transmission intensities in decibel scale (dB) of meandering loop mirrors with coupling lengths varying from 10 μm to 20 μm, modulated with grating couplers.

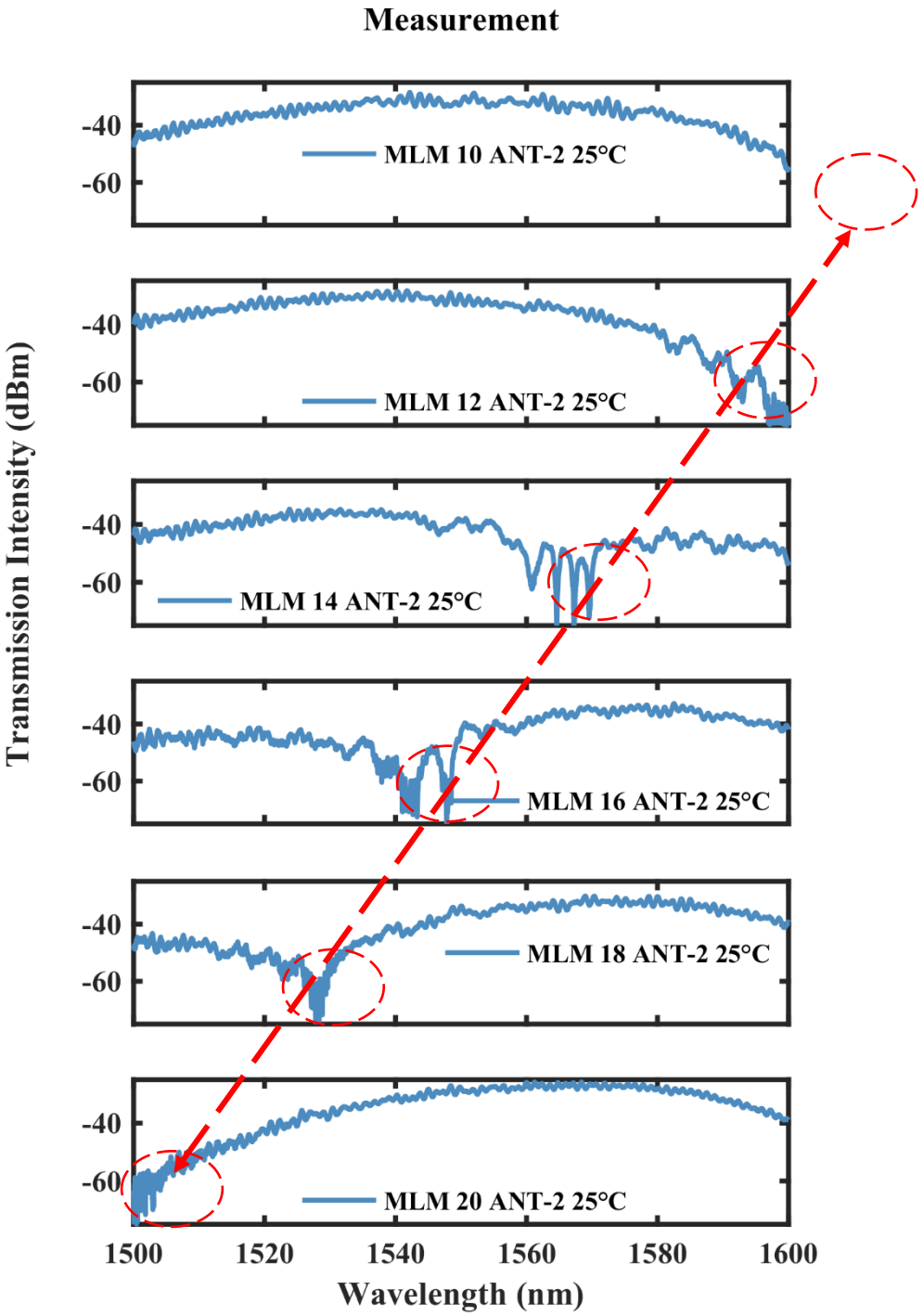

Figure 3.7: Measurement: Normalized transmission intensities in decibel scale (dBm) of meandering loop mirrors with coupling lengths varying from 10 µm to 20 µm, modulated with grating couplers.

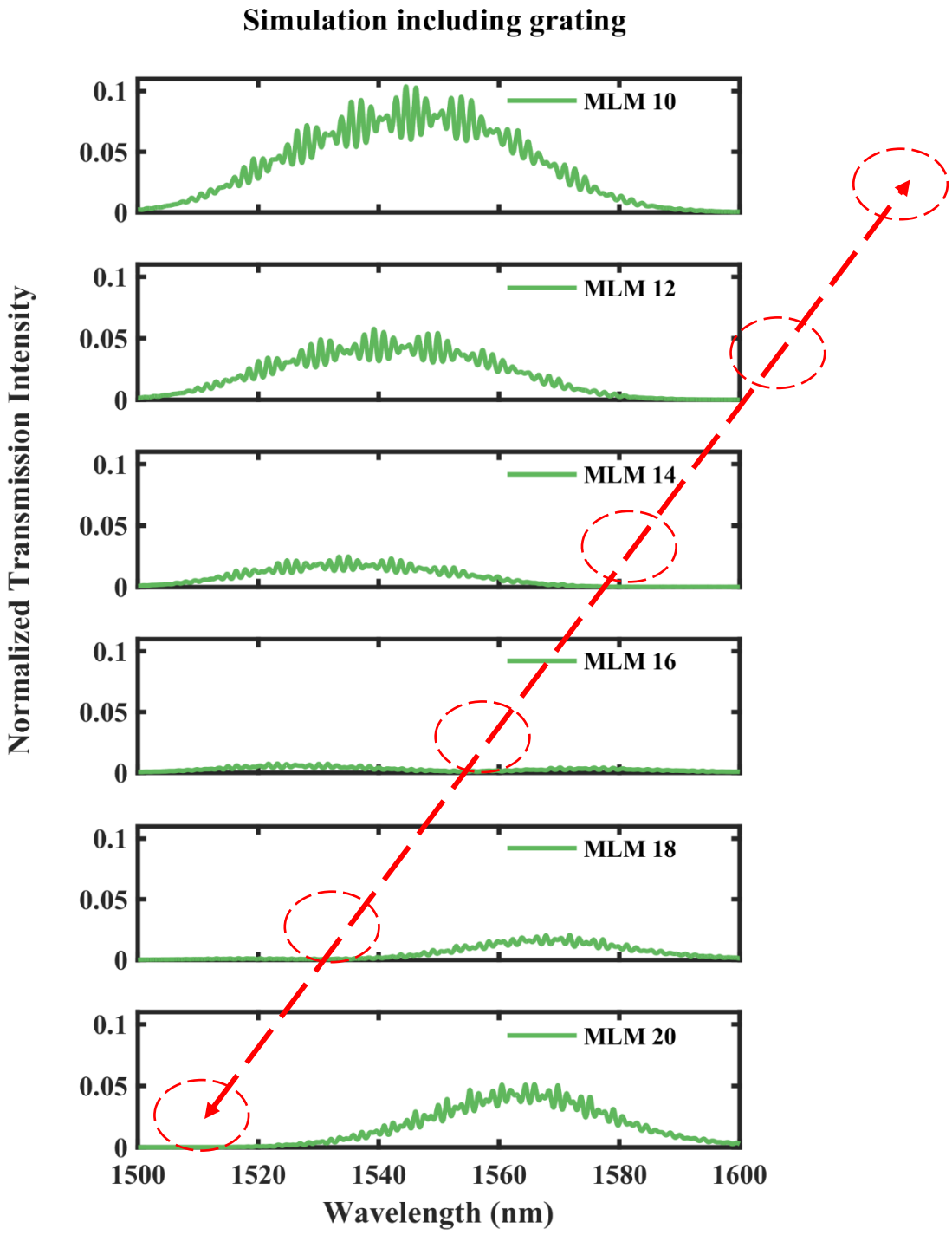

Figure 3.8: Simulation: Normalized transmission intensities of meandering loop mirrors with coupling lengths varying from 10 μm to 20 μm, modulated with grating couplers.

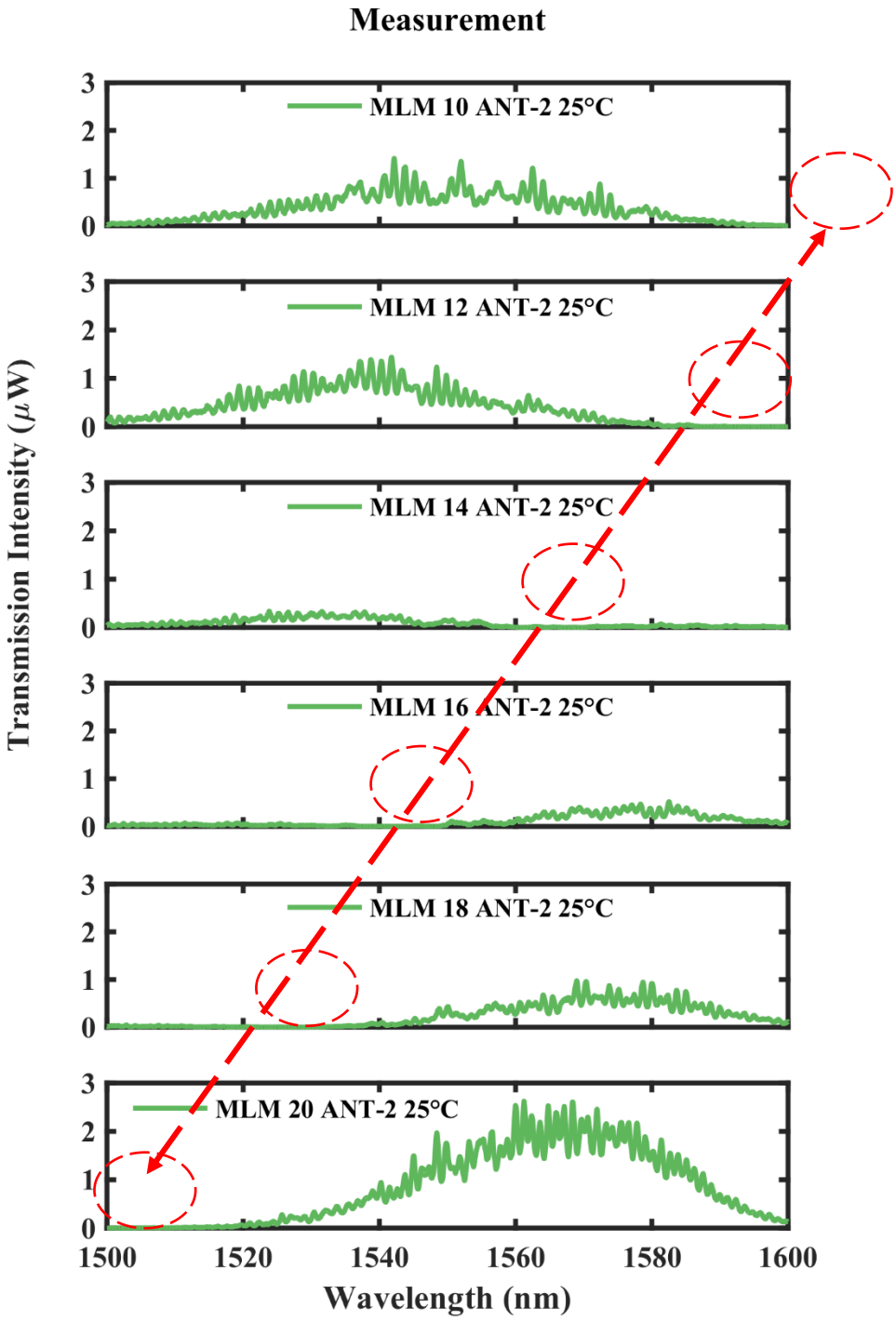

Figure 3.9: Measurement: Transmission intensities (mW) of meandering loop mirrors with coupling lengths varying from 10 μm to 20 μm, modulated with grating couplers.

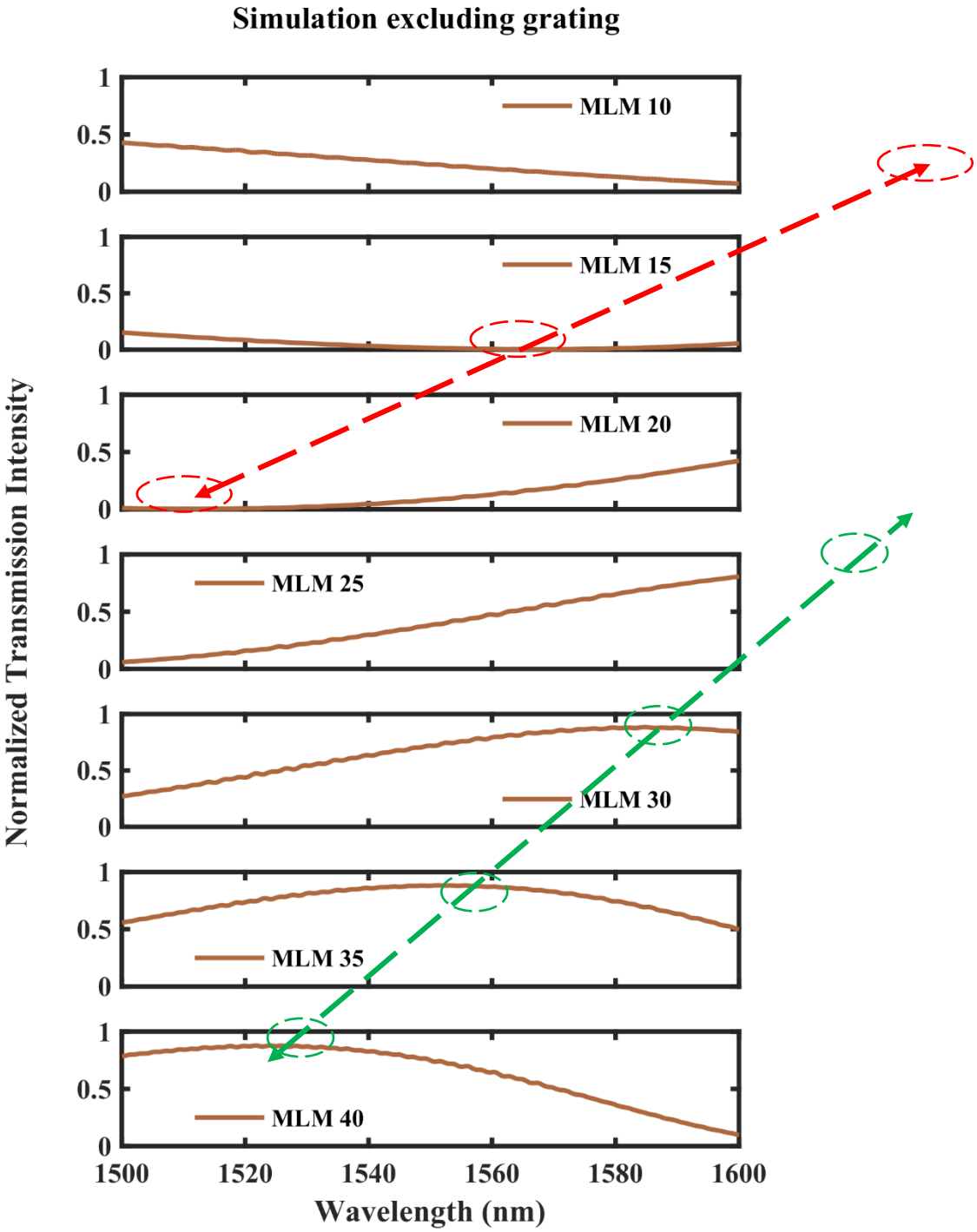

Figure 3.10: Simulation: Normalized transmission intensities of meandering loop mirrors with coupling lengths varying from 10 μm to 40 μm.

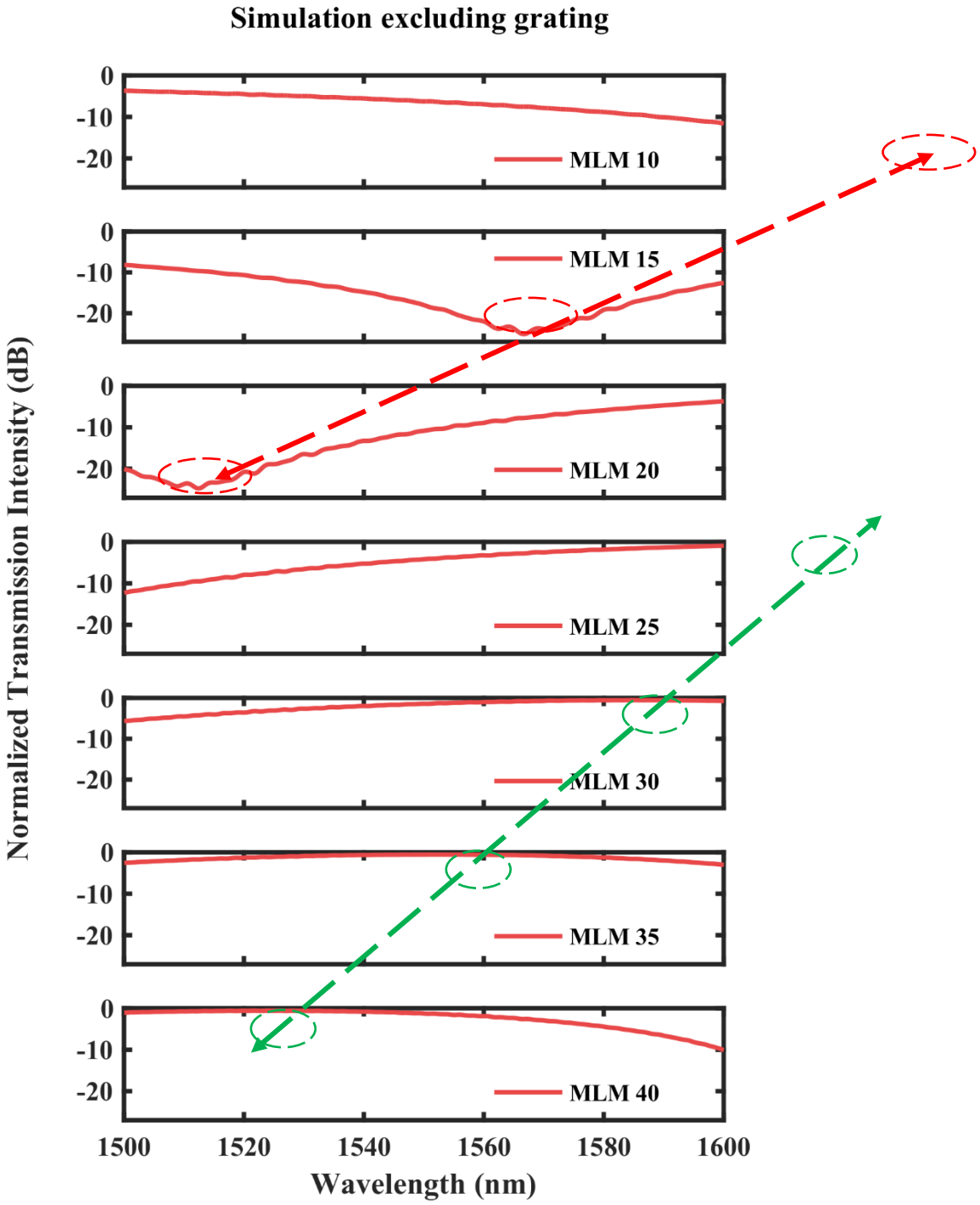

Figure 3.11: Simulation: Normalized transmission intensities in decibel scale (dB) of meandering loop mirrors with coupling lengths varying from 10 μm to 40 μm.

3.2 Meandering Resonator (MR)

After developing the basic understanding for the behavior of a single MLM, we investigate two cascaded MLMs. Since two cascaded MLMs form a Fabry-Pérot resonator, we call the cascaded MLM structures meandering resonators (MRs).

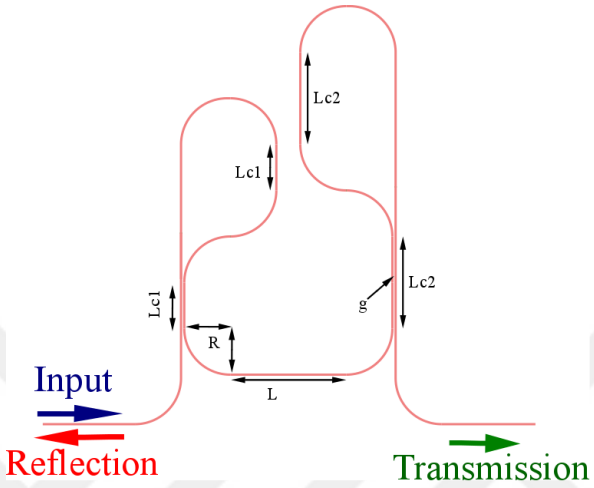

Figure 3.12: MR consisting of two MLMs with coupling lengths of Lc1 and Lc2 respectively.

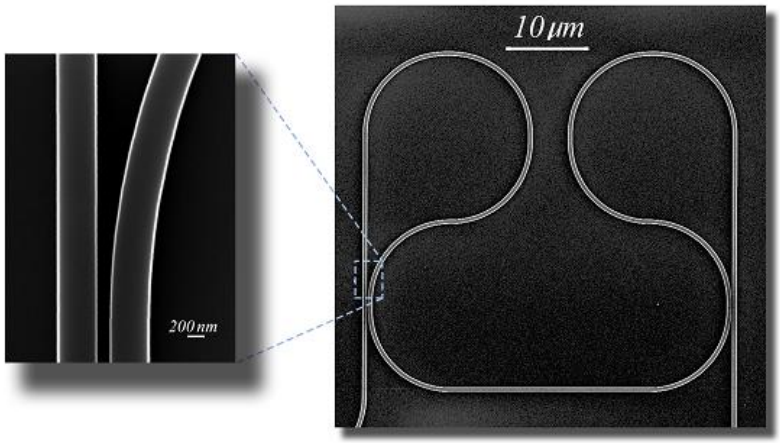

Figure 3.13: SEM of an MR consisting of two MLMs with same coupling lengths.

Figure 3.12 and Figure 3.13 show a layout and an SEM of a MR, respectively. Lc1 and Lc2 are the coupling lengths of the two DCs, R is the bending radii.

The response of an MR is similar to a Fabry-Pérot resonator as the reflectance tuning of the Fabry-Pérot mirrors is analogous to the coupling tuning in an MLM.

We investigated MRs for the cases, when Lc1 = Lc2 (symmetric MR) and Lc1 ≠ Lc2 (asymmetric MR). Optical path length (perimeter) of an MR can be given as

$$MR\ Lc1\ vs\ Lc2 = MLM\ Lc1 + MLM\ Lc2 + 2(\pi R + L) \tag{3.2}$$

Spectra in Figure 3.14 and Figure 3.15 show the simulation results for the transmission intensities in normalized and dB scales, respectively, for the MR structures with coupling lengths from 10 μm to 20 μm. A Fabry-Pérot like behavior is observed. At the maximum reflectivity points of the MLM, the energy stored in the MR is reduced, while the Q-factor rises.

Since the MLM is highly reflective at a wavelength of 1610 nm in MLM 12 to around 1510 nm in MLM 20. At these wavelengths, we expect to see the maximum Q-factor of the MR. We compared the simulation results in Figure 3.16 to the measurement results in Figure 3.17. The measured spectra are plotted for the chip-1 fabricated by ANT. These spectra were scanned for the wavelength range of 1480 nm to 1580 nm, whereas the simulation range is from 1500 nm to 1600 nm. In the overlap region between the simulated and measured spectra, the results correspond well to each other.

In Figure 3.18 and Figure 3.19, we plotted the normalized transmission intensities for the simulated, and the measured transmission intensities for the fabricated case, respectively. The dips can be located in both cases, and are indicated with a dashed red line. The slope of the mentioned red line indicates that, the high Q-factor peaks are moving to the lower wavelengths (blue shifting) as the coupling length is increased from 10 μm to 20 μm.

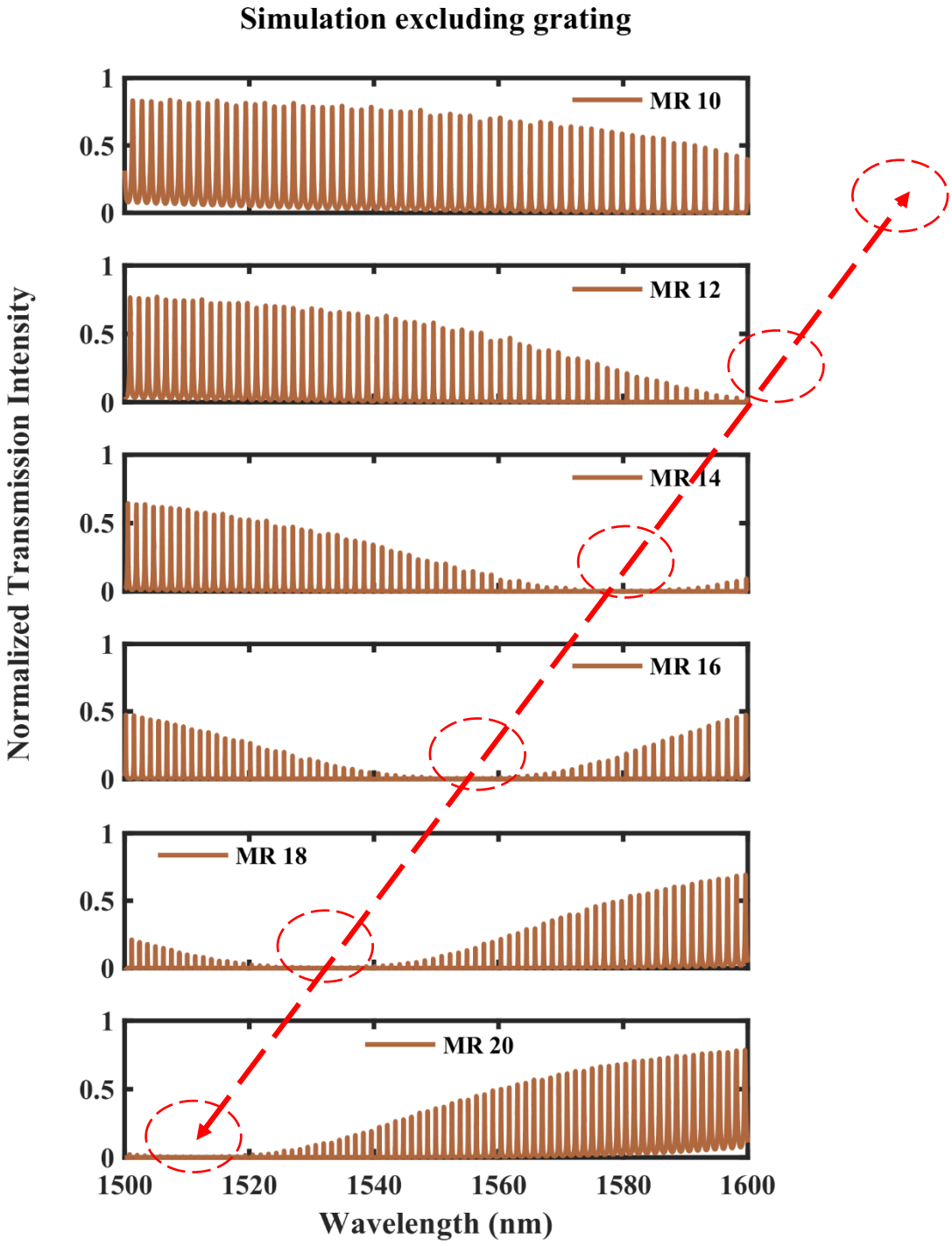

Figure 3.14: Simulation: Normalized transmission intensities of MR Lc, with coupling lengths Lc varying from 10 μm to 20 μm.

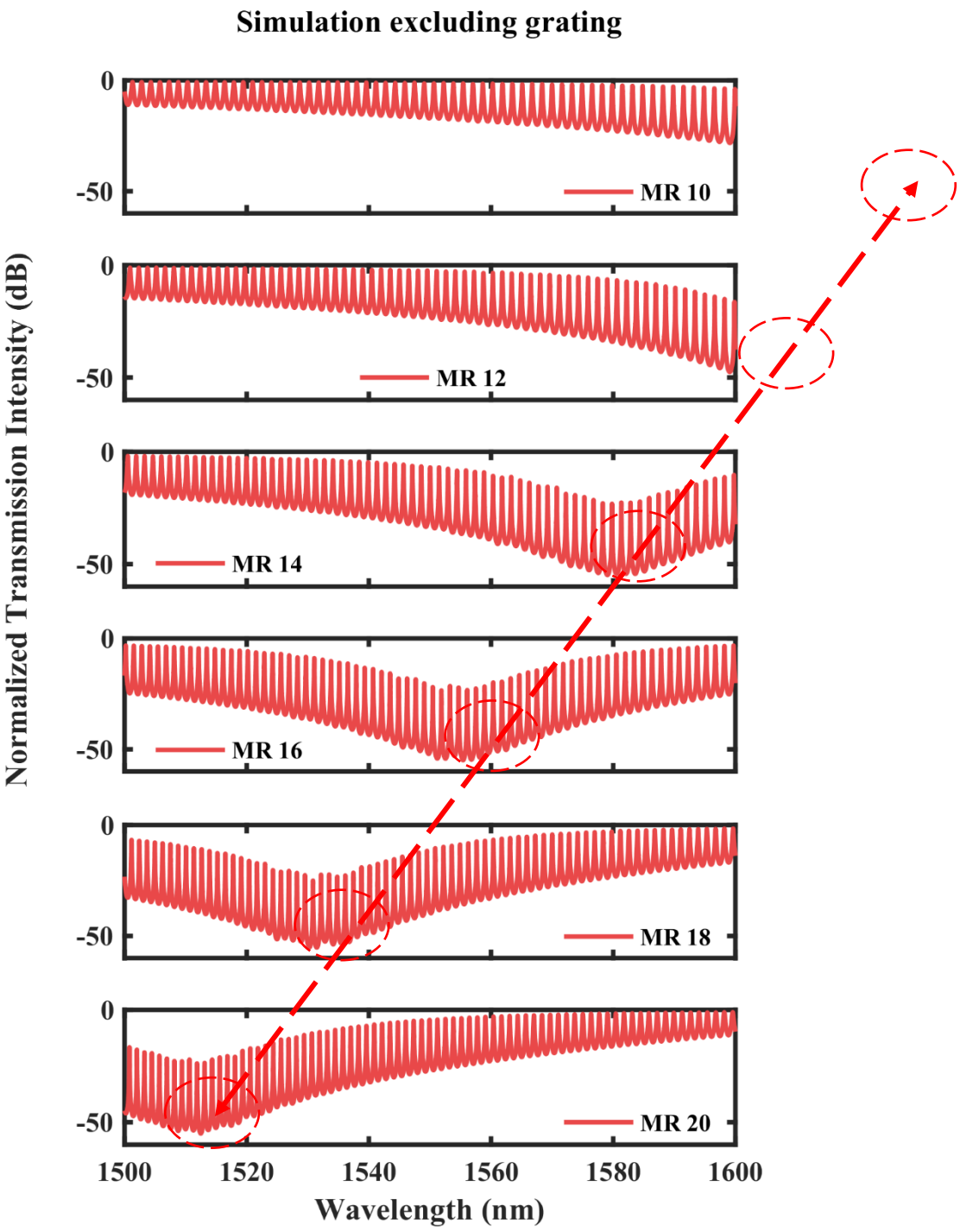

Figure 3.15: Simulation: Normalized transmission intensities in decibel scale (dB) of MR Lc, with coupling lengths Lc, varying from 10 μm to 20 μm.

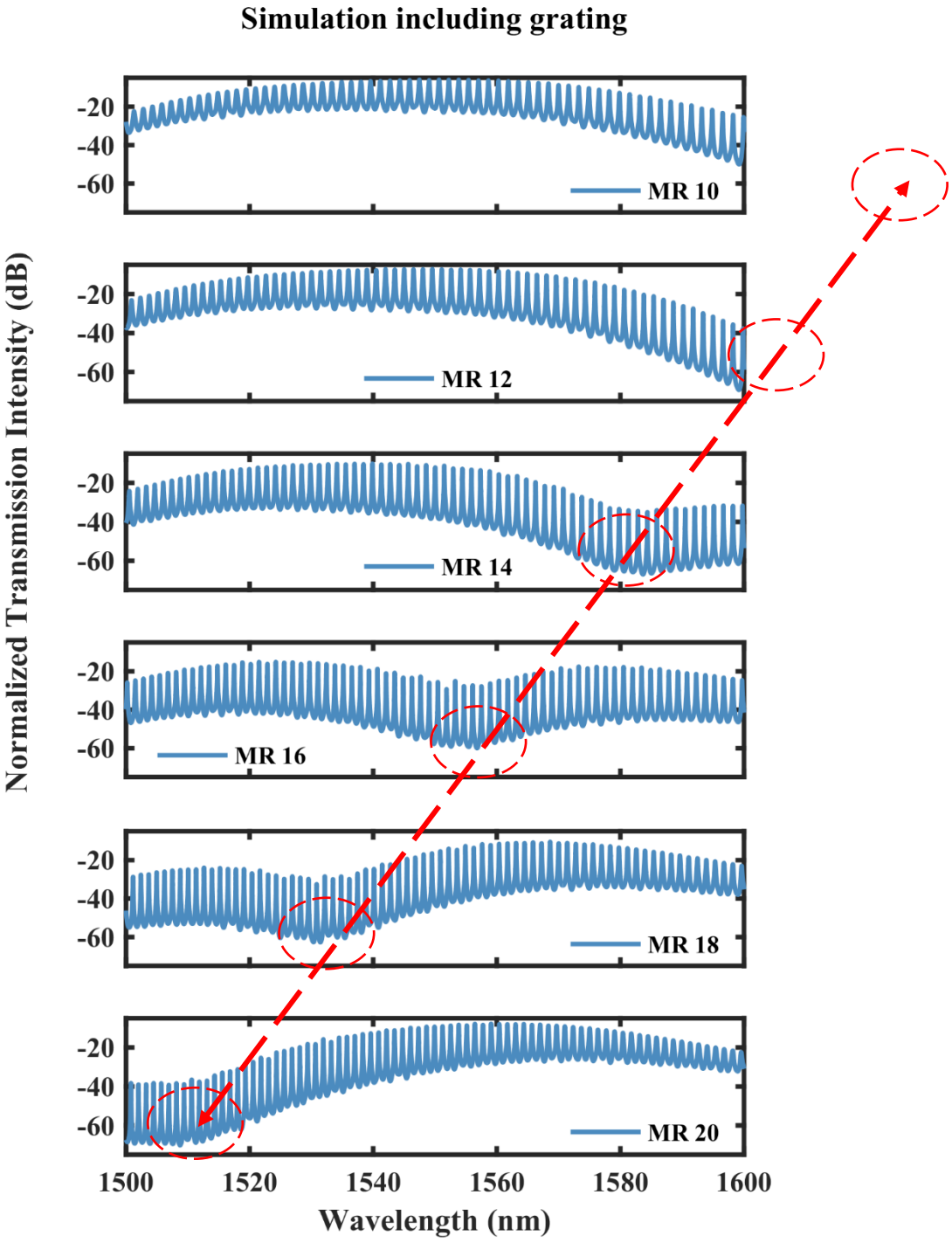

Figure 3.16: Simulation: Normalized transmission intensities in decibel scale (dB) of MR Lc, with coupling lengths Lc varying from 10 µm to 20 µm, modulated with grating couplers.

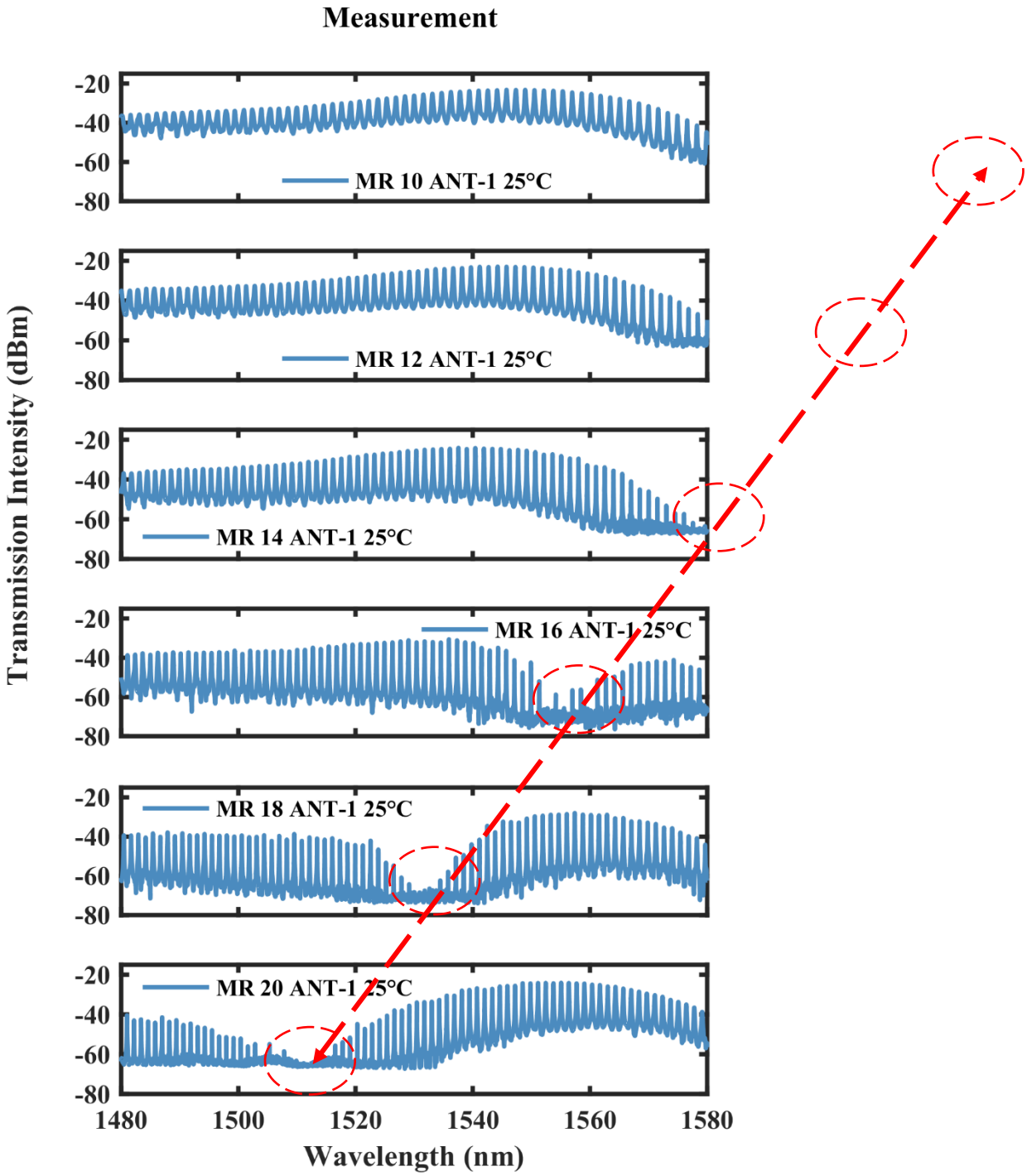

Figure 3.17: Measurement: Normalized transmission intensities in decibel scale (dBm) of MR Lc, with coupling lengths Lc, varying from 10 µm to 20 µm, modulated with grating couplers.

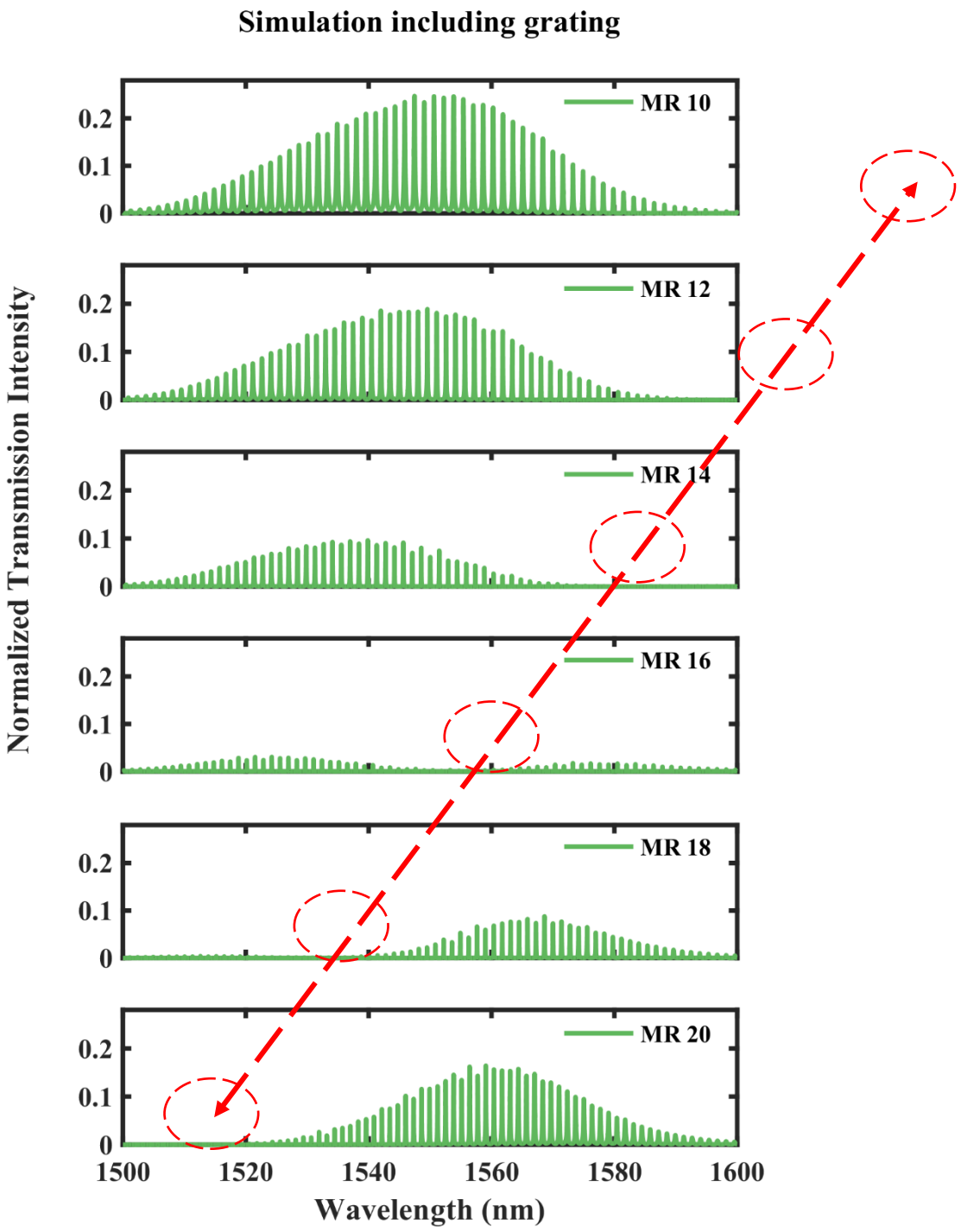

Figure 3.18: Simulation: Normalized transmission intensities of MR Lc, with coupling lengths Lc varying from 10 μm to 20 μm, modulated with grating couplers.

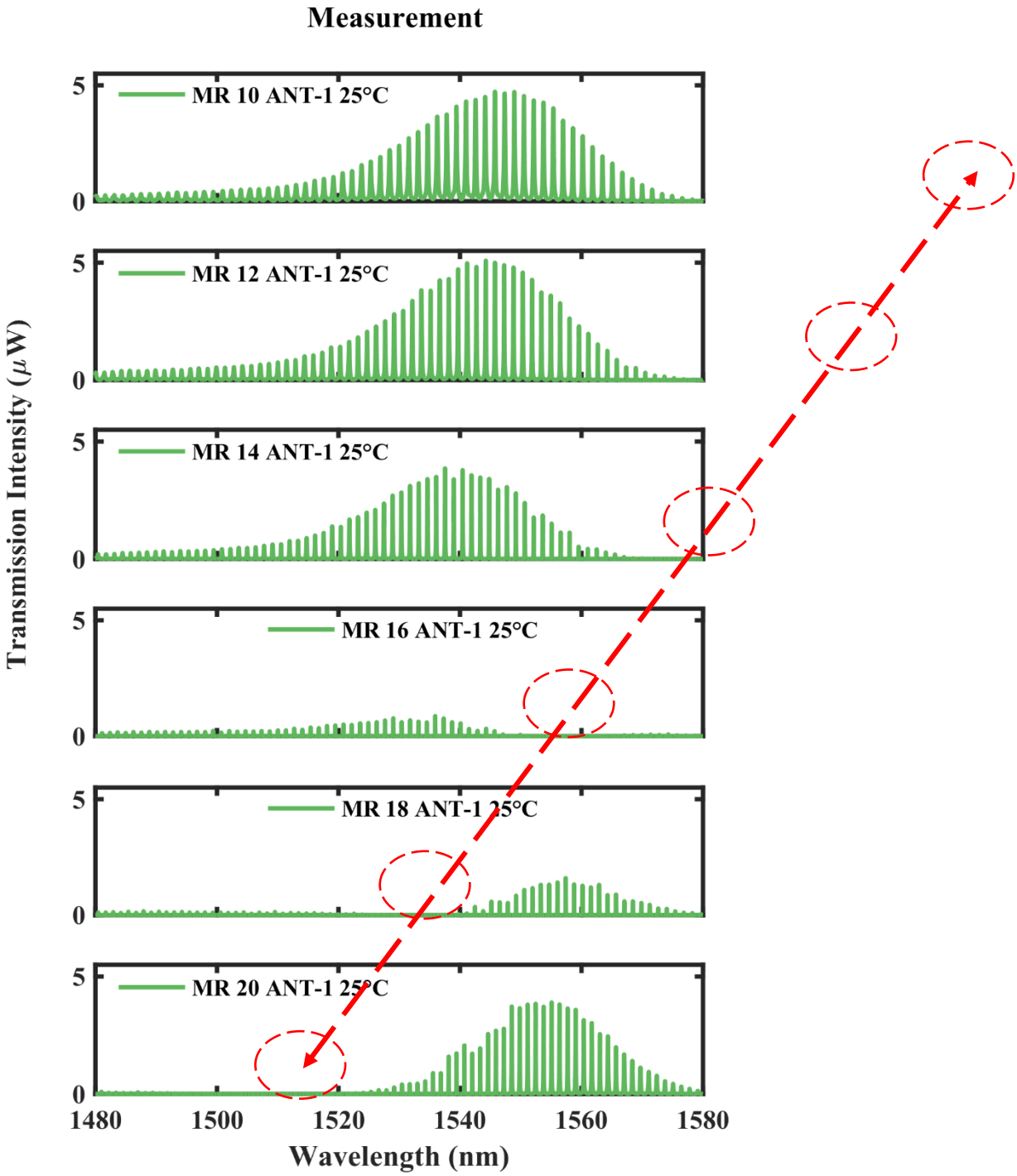

Figure 3.19: Measurement: Transmission intensities (mW) of MR Lc, with coupling lengths Lc varying from 10 µm to 20 µm, modulated with grating couplers.

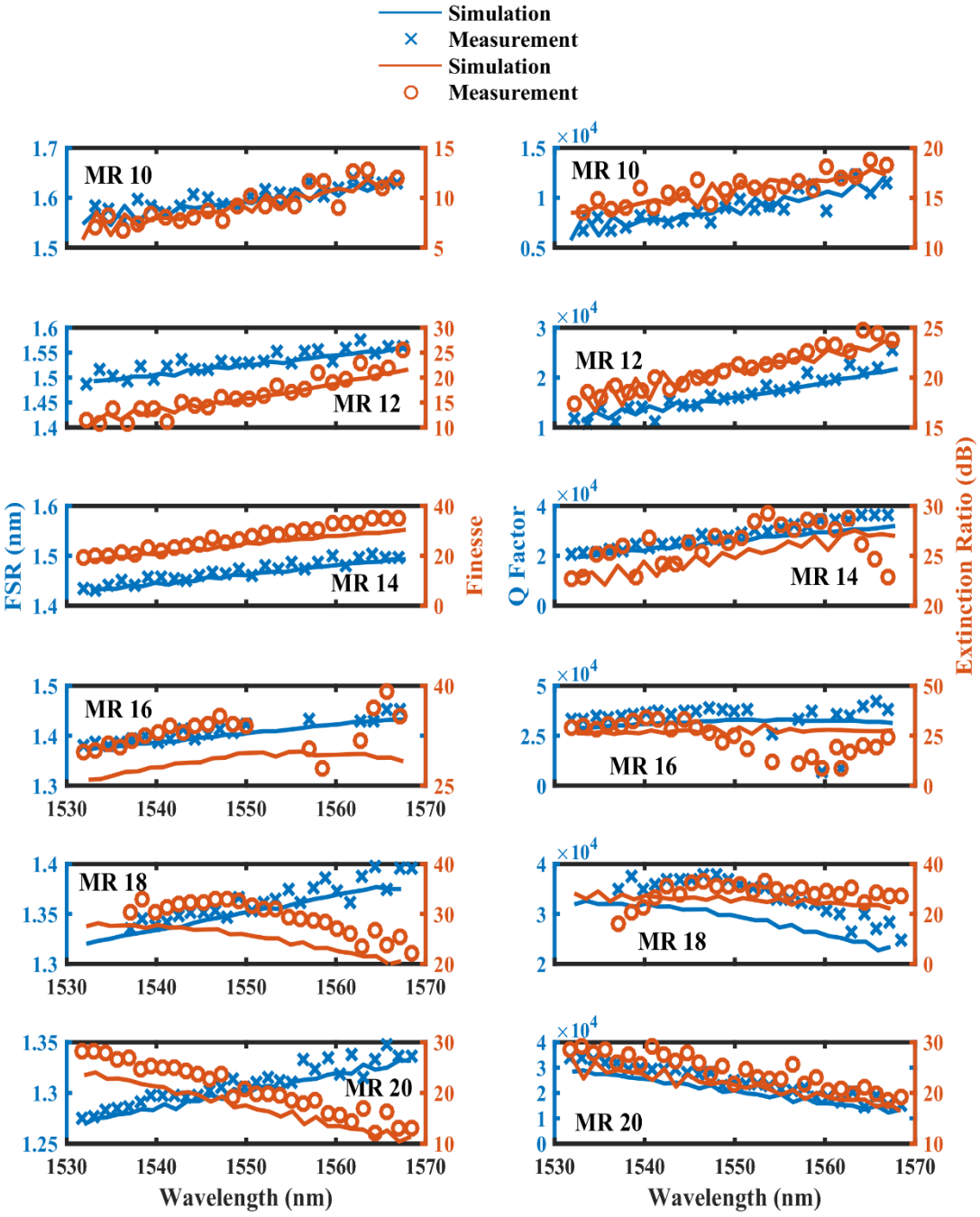

Figure 3.20: Figures of Merit for Simulated and Measured, MR Lc structures, with Lc varying from 10 µm to 20 µm

Figure 3.20, captures the overall performance of the MRs. Maximum Q-factor of around $5x10^4$ was observed in MR 16. Finesse increases from 5 to 30 in MR 10 to 16, then returns back to around a value of 10 in MR 20. Extinction ratios (ERs) are sensitive to the reflectance of the MLMs, and become worse at the high reflectance values of the mirror. FSR ranges from 1.25 nm to 1.7 nm.

3.3 MR with Asymmetric MLMs

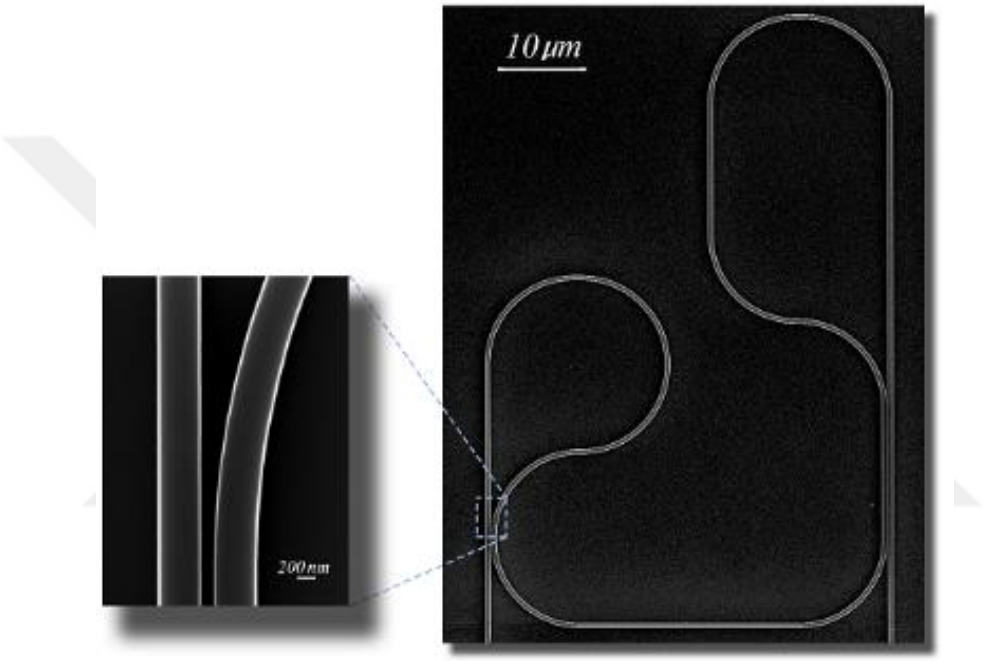

Figure 3.21: SEM of an MR consisting of two MLMs with different coupling lengths.

Simulation: Normalized transmission intensities in decibel scale (dB) of an MR with asymmetric MLMs, with coupling lengths Lc1 0 μm and Lc2 varying from 15 μm to 40 μm, modulated with grating couplers.

Measurement: Normalized transmission intensities in decibel scale (dB) of an MR with asymmetric MLMs, with coupling lengths Lc1 0 μm and Lc2 varying from 15 μm to 40 μm, modulated with grating couplers.

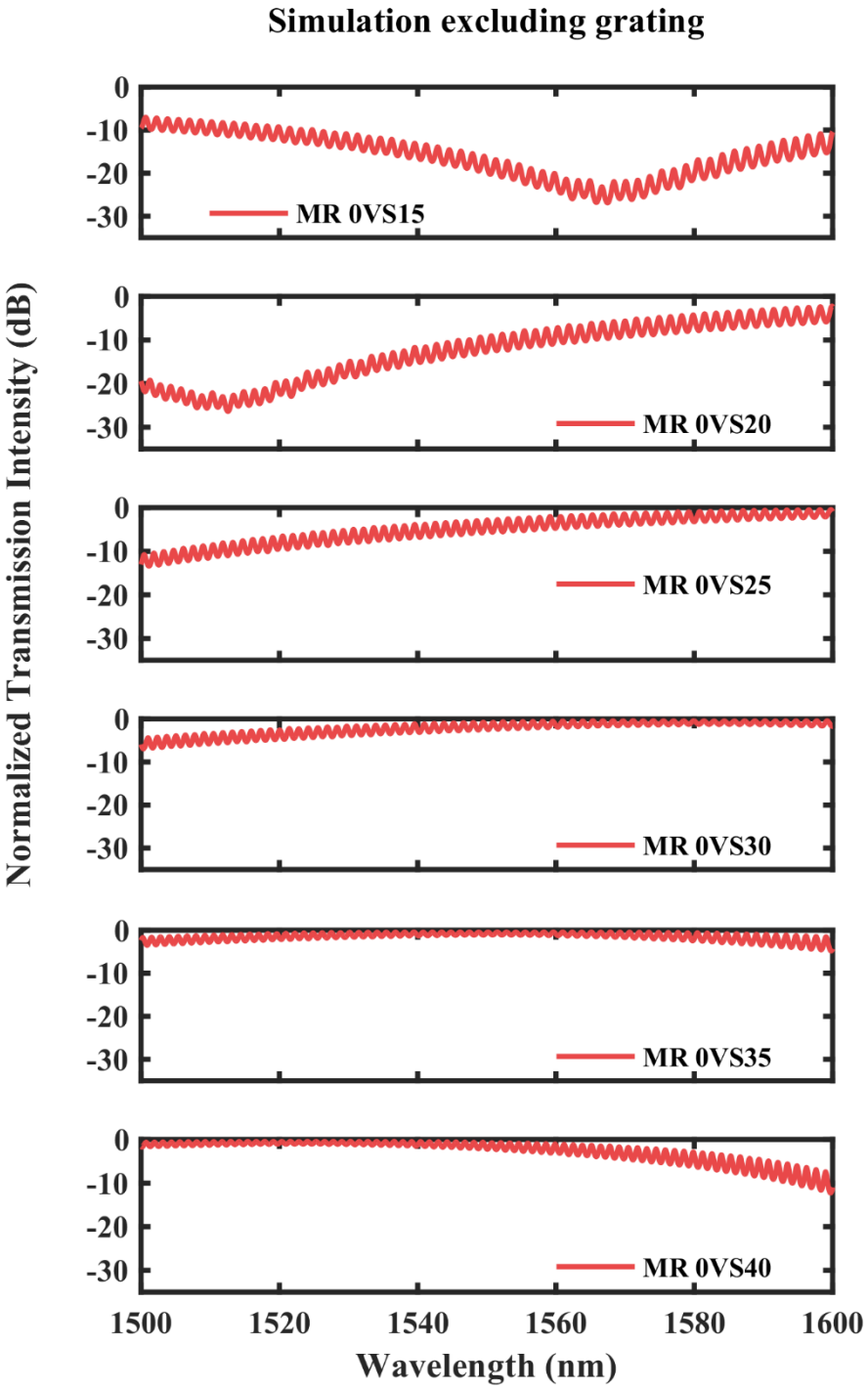

Figure 3.22: Simulation: Normalized transmission intensities in decibel scale (dB) of an MR with asymmetric MLMs, with coupling lengths Lc1 0 µm and Lc2 varying from 15 µm to 40 µm, modulated with grating couplers.

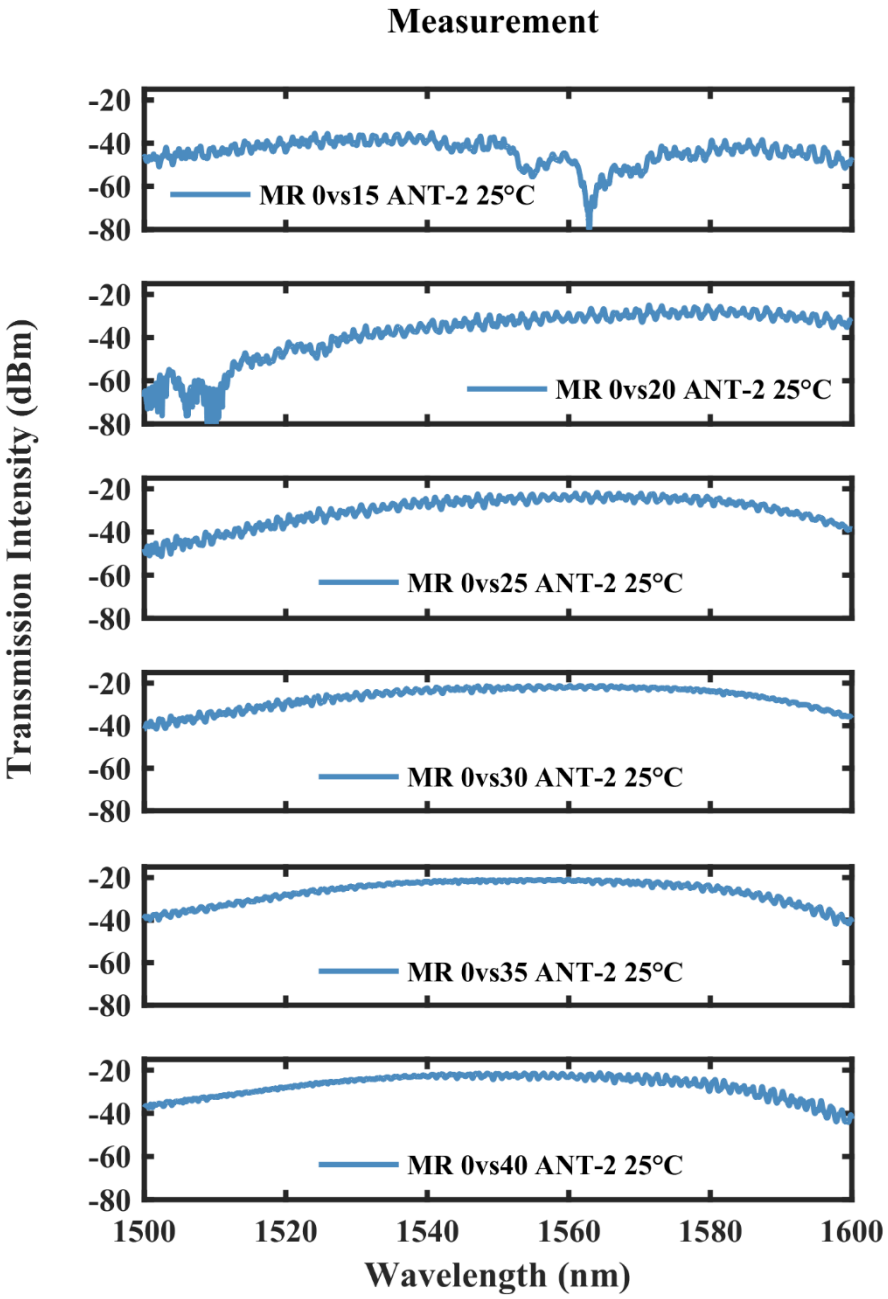

Figure 3.23: Measurement: Normalized transmission intensities in decibel scale (dB) of an MR with asymmetric MLMs, with coupling lengths Lc1 0 µm and Lc2 varying from 15 µm to 40 µm, modulated with grating couplers.

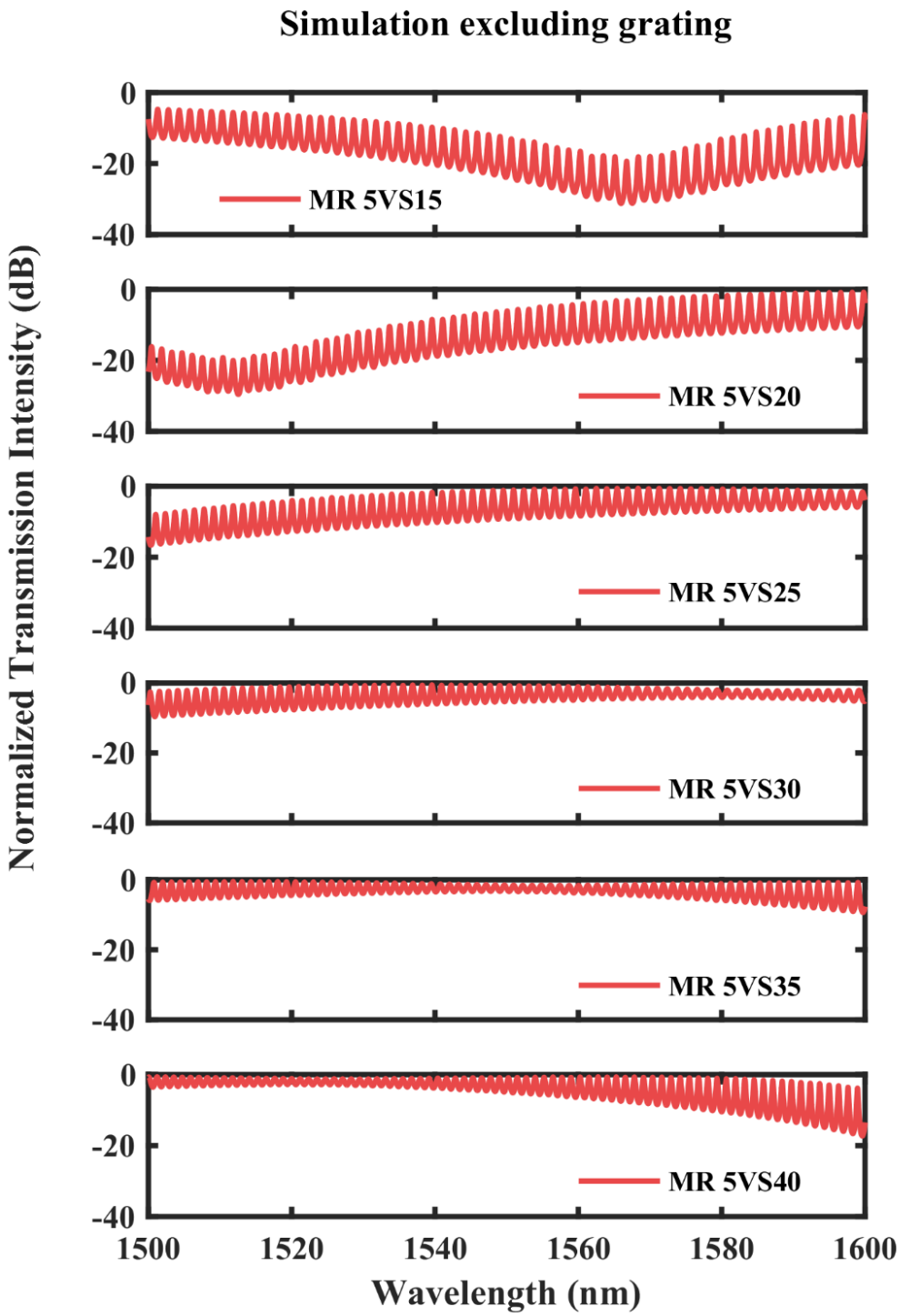

Figure 3.24: Simulation: Normalized transmission intensities in decibel scale (dB) of an MR with asymmetric MLMs, with coupling lengths Lc1 5 μm and Lc2 varying from 15 μm to 40 μm, modulated with grating couplers.

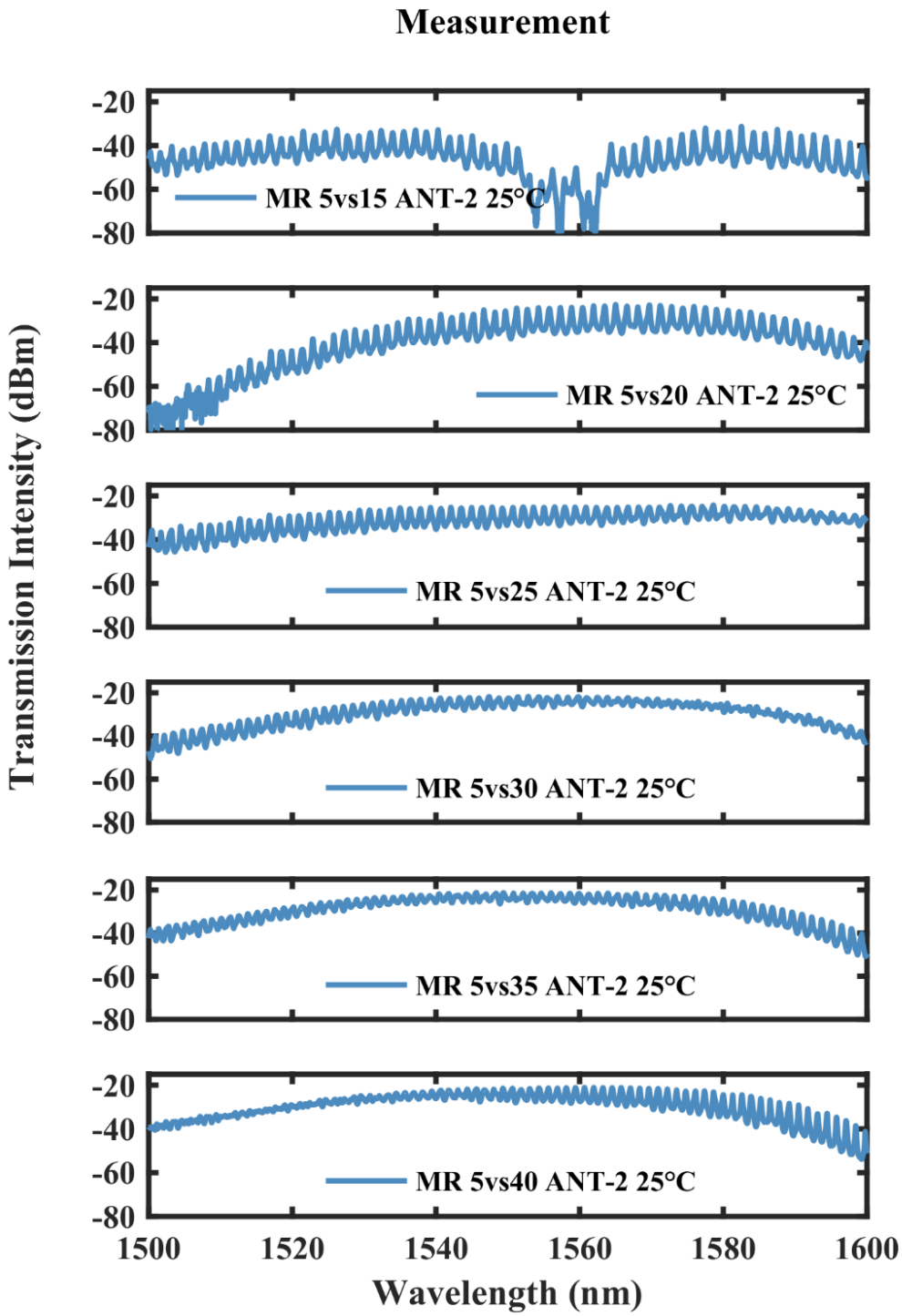

Figure 3.25: Measurement: Normalized transmission intensities in decibel scale (dB) of an MR with asymmetric MLMs, with coupling lengths Lc1 5 μm and Lc2 varying from 15 μm to 40 μm, modulated with grating couplers.

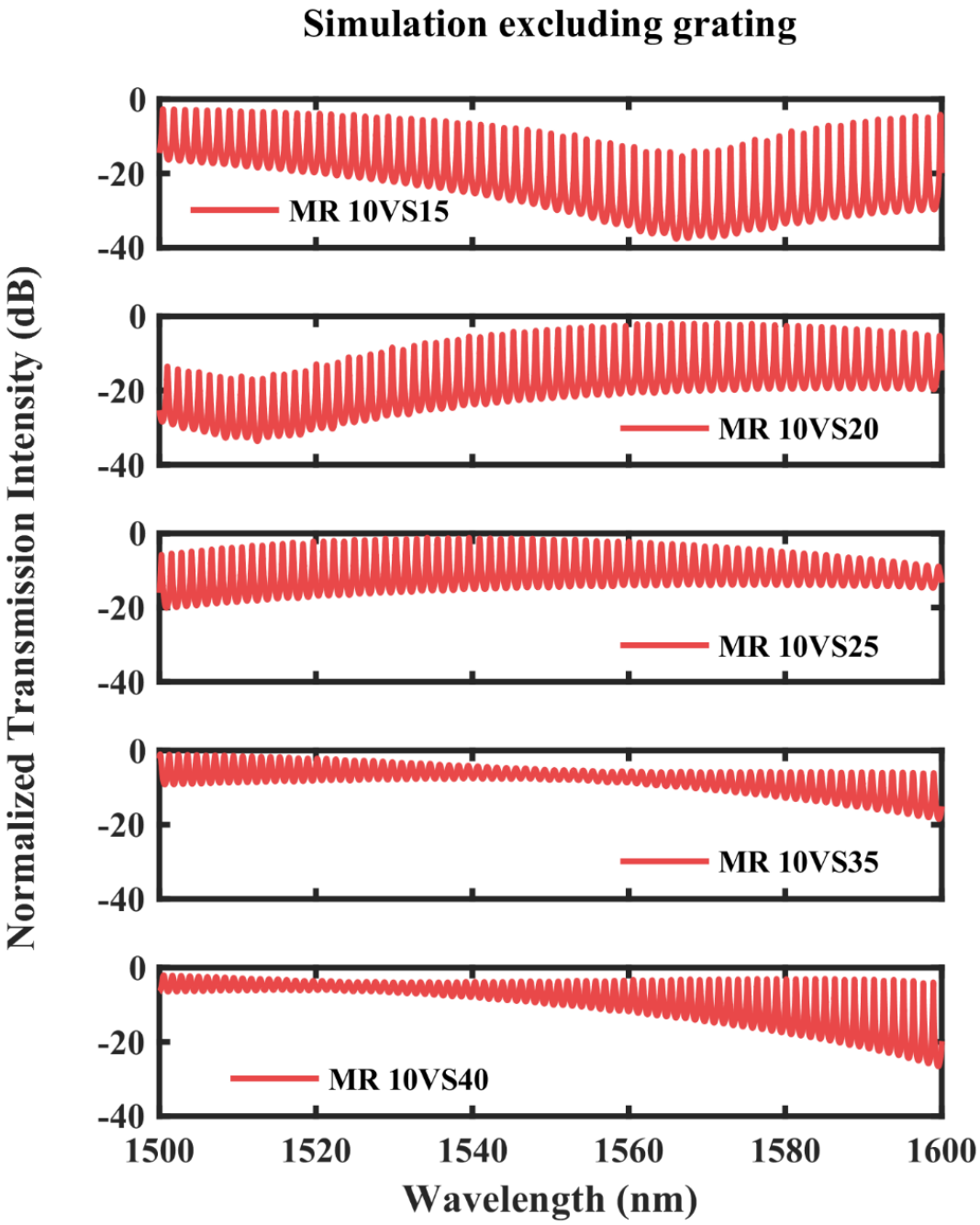

Figure 3.26: Simulation: Normalized transmission intensities in decibel scale (dB) of an MR with asymmetric MLMs, with coupling lengths Lc1 10 µm and Lc2 varying from 15 µm to 40 µm, modulated with grating couplers.

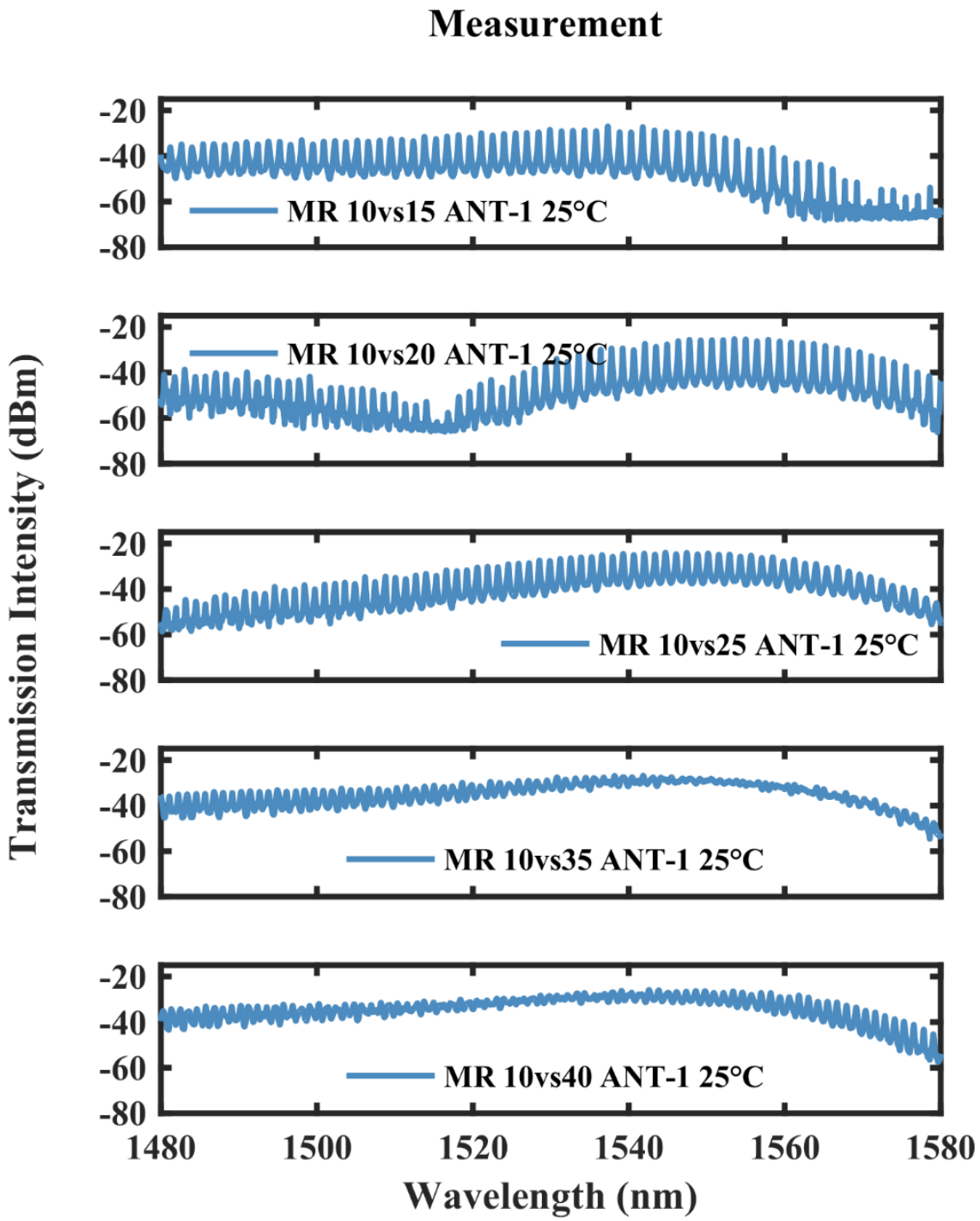

Figure 3.27: Measurement: Normalized transmission intensities in decibel scale (dB) of an MR with asymmetric MLMs, with coupling lengths Lc1 10 μm and Lc2 varying from 15 μm to 40 μm, modulated with grating couplers.

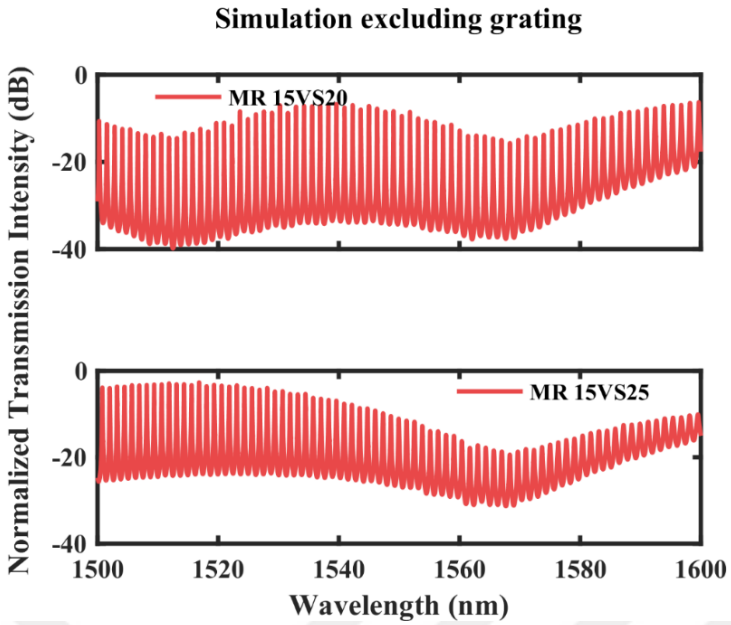

Figure 3.28: Simulation: Normalized transmission intensities in decibel scale (dB) of an MR with asymmetric MLMs, with coupling lengths Lc1 15 µm and Lc2 varying from 15 µm to 40 µm, modulated with grating couplers.

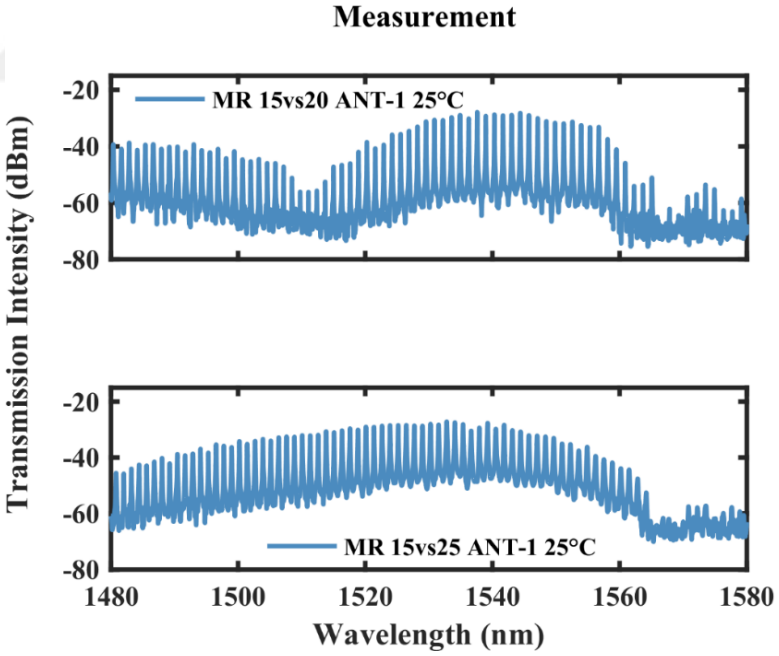

Figure 3.29: Measurement: Normalized transmission intensities in decibel scale (dB) of an MR with asymmetric MLMs, with coupling lengths Lc1 15 µm and Lc2 varying from 15 µm to 40 µm, modulated with grating couplers.

3.4 Antisymmetric meandering resonator (AMR)

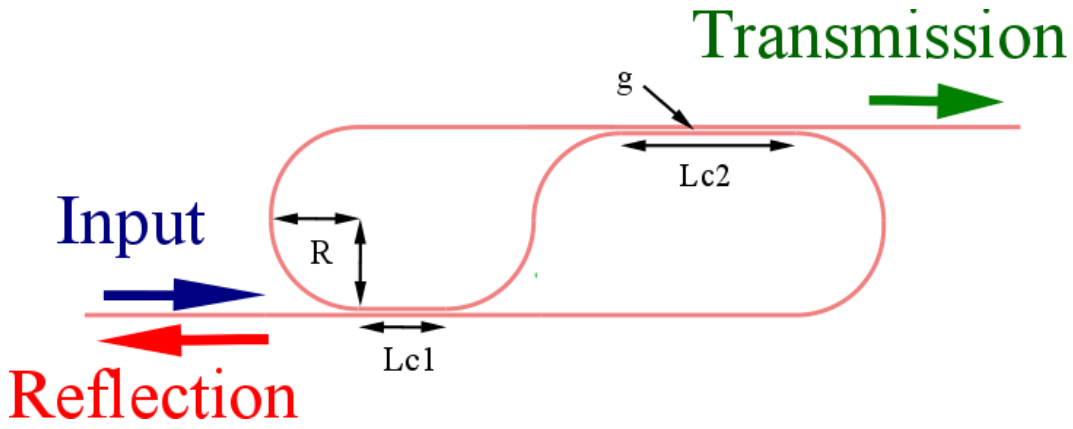

Figure 3.30: AMR consisting of two couplers of lengths of Lc1 and Lc2.

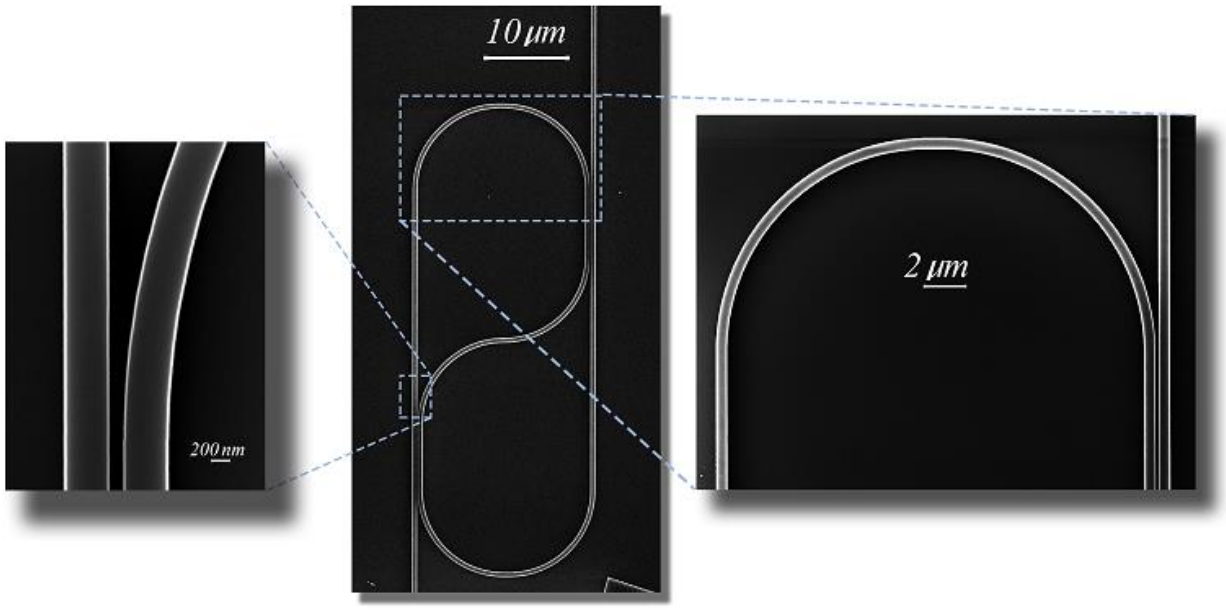

Figure 3.31: SEM of an AMR consisting of two couplers of similar lengths.

Figure 3.30 and Figure 3.31 shows a layout and an SEM of an AMR, respectively. Lc1 vs Lc2 are the coupling lengths of the two DCs, and R is the bending radii. AMR Lc denotes the case, when all the coupling lengths are equal, i.e., Lc1 = Lc2.

We have investigated AMRs for the cases when Lc1 = Lc2 (symmetric AMR) and Lc1 ≠ Lc2 (asymmetric AMR).

Optical path length (perimeter) of an AMR can be given as

$$AMR\ Lc = 2(R(\pi + 2) + 2\ Lc + g) \tag{3.3}$$

Spectra in Figure 3.32 and Figure 3.33 show the simulation results for the transmission intensities in normalized and dB scales, respectively, for the AMR structures with equal coupling lengths from 10 μm to 20 μm.

The resonance peaks move towards higher quality factor values as the coupling is increased. The dotted red line indicates the shift in the resonance condition due to the variation in the optical path length introduced by different coupling lengths of the directional couplers.

Figure 3.34 shows the intensities of AMR connected to the input and output grating couplers, for Lc = Lc1 = Lc2, where Lc is varied from 10 to 20 μm. Figure 3.35 shows the measured spectra of the AMR 10 to AMR 20. The resonant peak positions in the measurement are shifted, which is due to the effect of fabrication variations in the devices. Calculated FSRs for the measurements are in accordance with the simulations. Overall we see a good agreement between the simulations and the measurements.

To distinguish the resonance peaks from the side lobes, in Figure 3.36 and Figure 3.37 we have plotted the normalized intensities of the simulated and the measured spectra respectively.

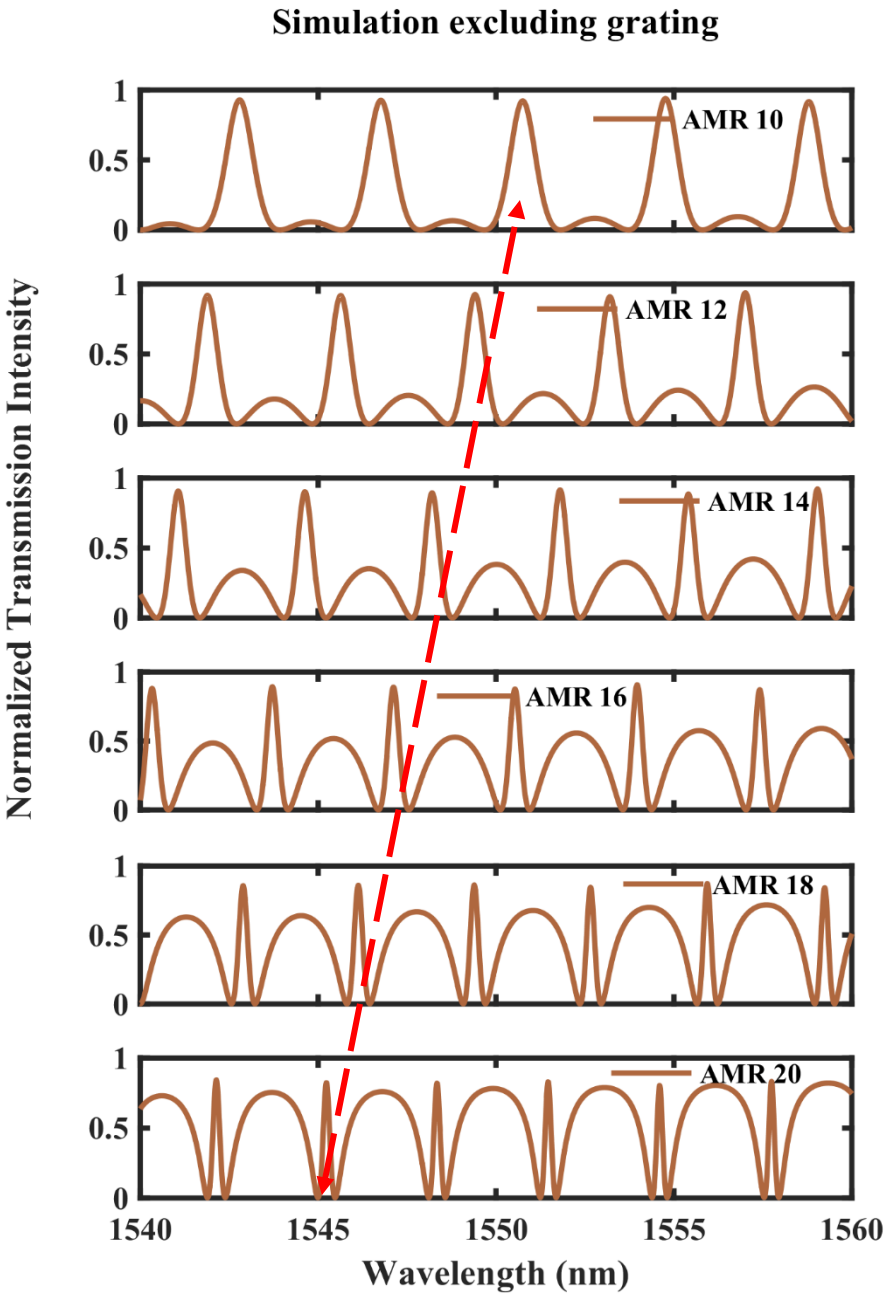

Figure 3.32: Simulation: Normalized transmission intensities of AMR Lc, with coupling lengths Lc varying from 10 μm to 20 μm.

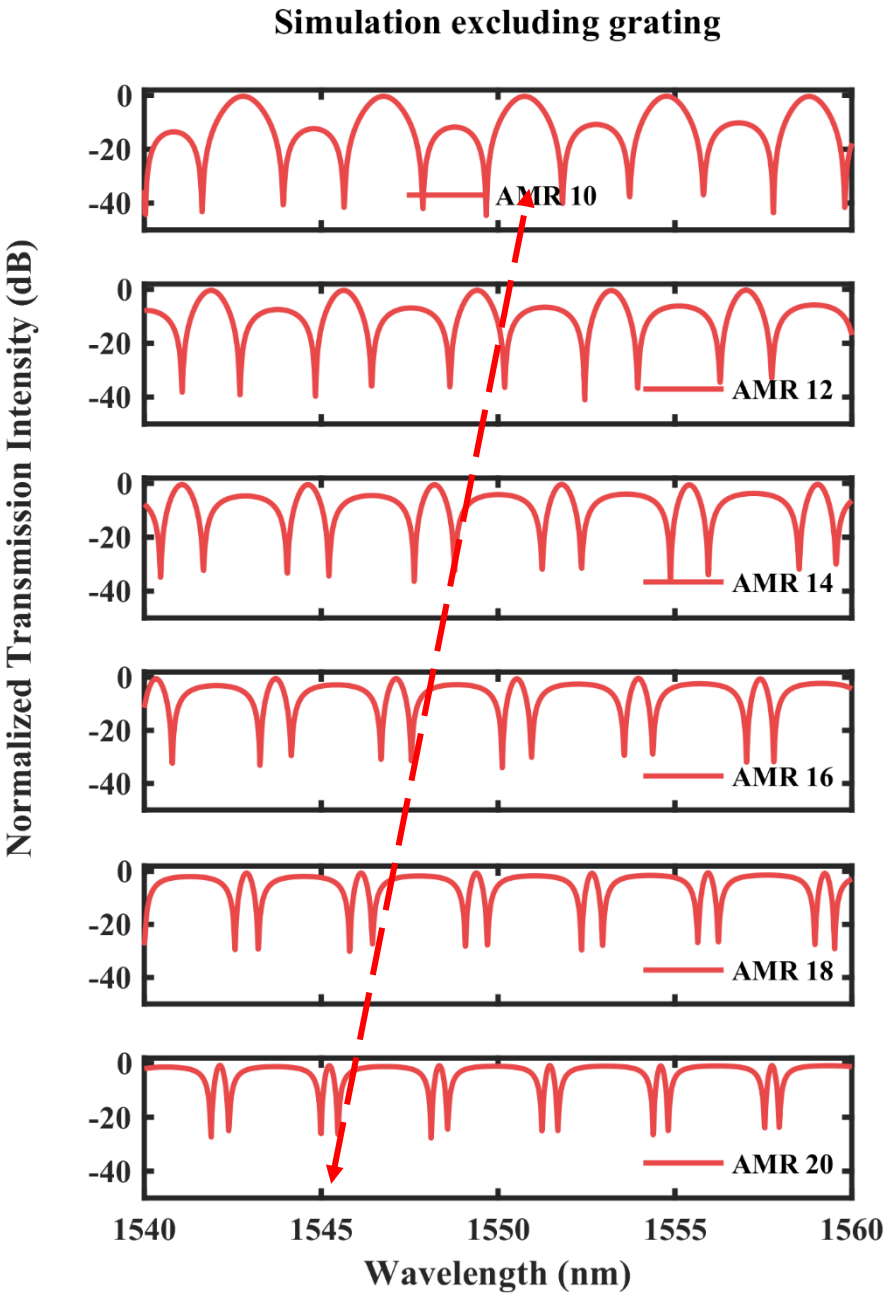

Figure 3.33: Simulation: Normalized transmission intensities in decibel scale (dB) of AMR Lc, with coupling lengths Lc, varying from 10 μm to 20 μm.

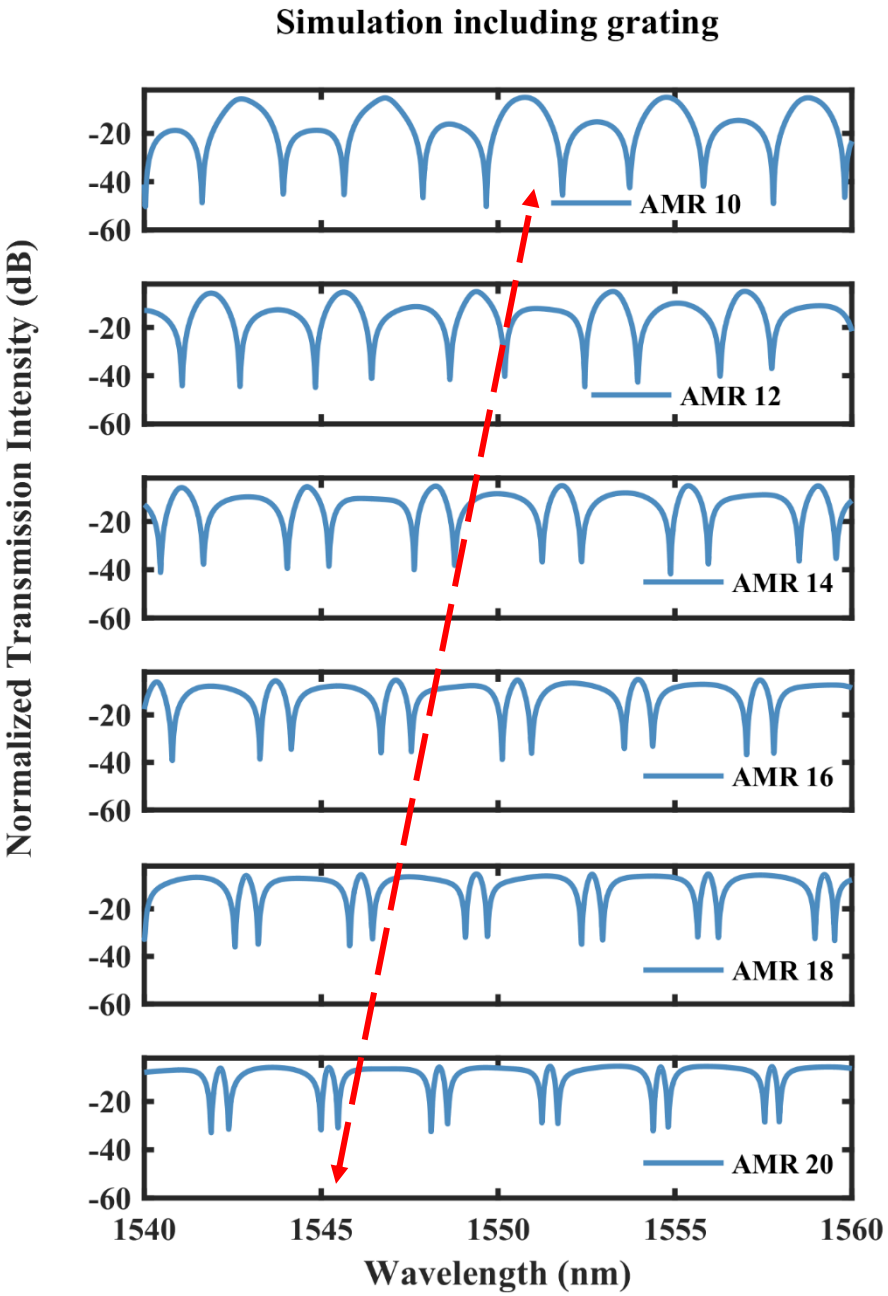

Figure 3.34: Simulation: Normalized transmission intensities in decibel scale (dB) of AMR Lc, with coupling lengths Lc varying from 10 μm to 20 μm, modulated with grating couplers.

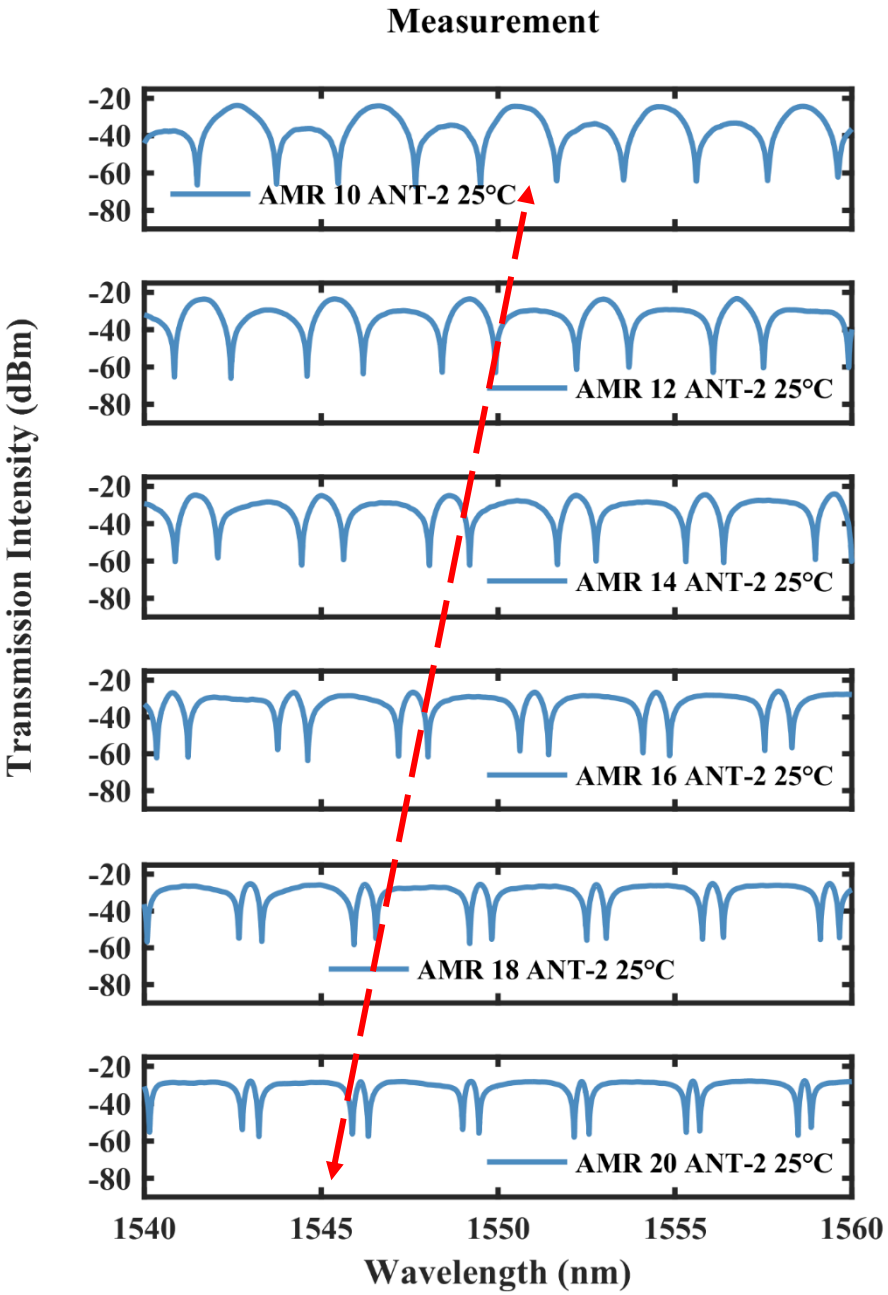

Figure 3.35: Measurement: Normalized transmission intensities in decibel scale (dBm) of MR Lc, with coupling lengths Lc varying from 10 µm to 20 µm, modulated with grating couplers.

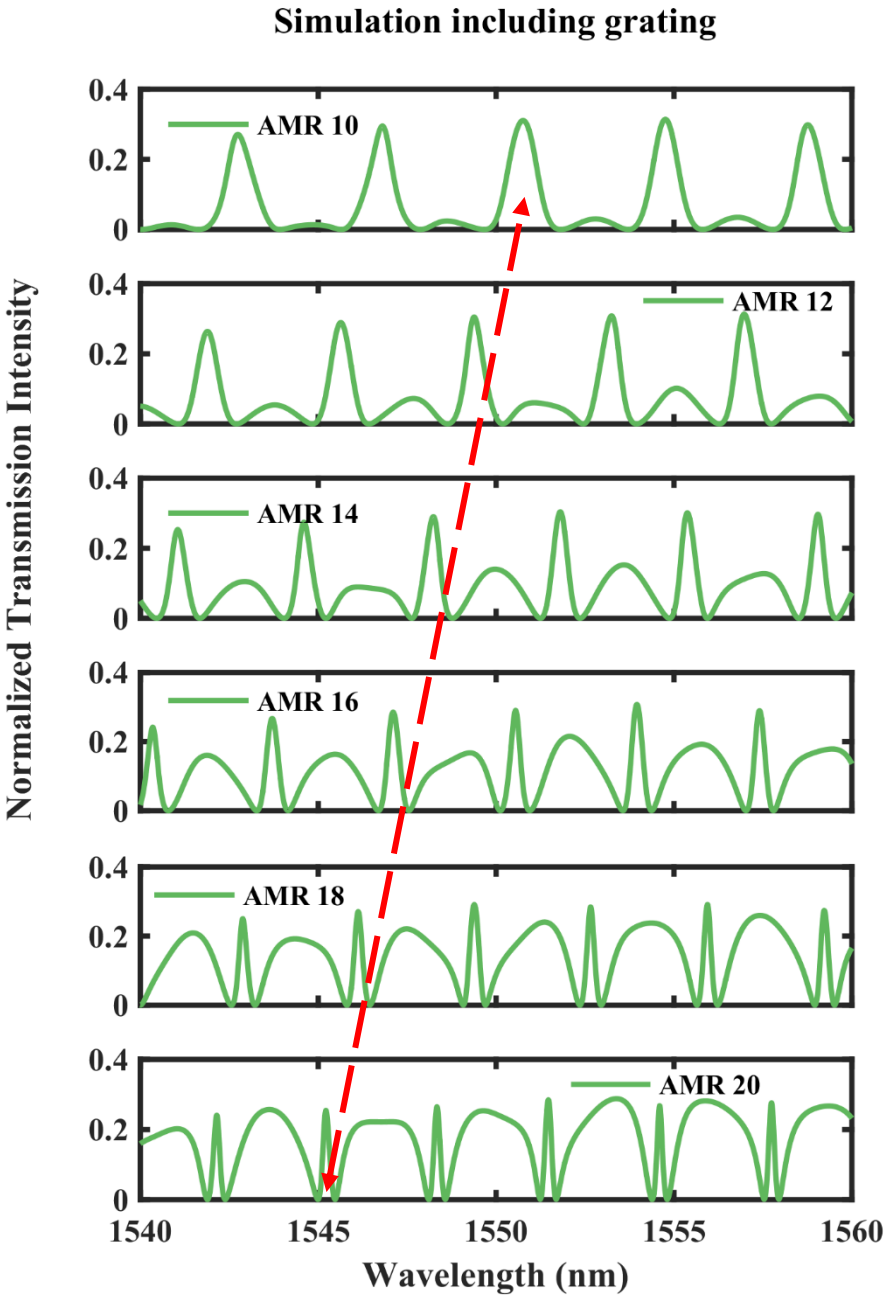

Figure 3.36: Simulation: Normalized transmission intensities of AMR Lc, with coupling lengths Lc varying from 10 μm to 20 μm, modulated with grating couplers.

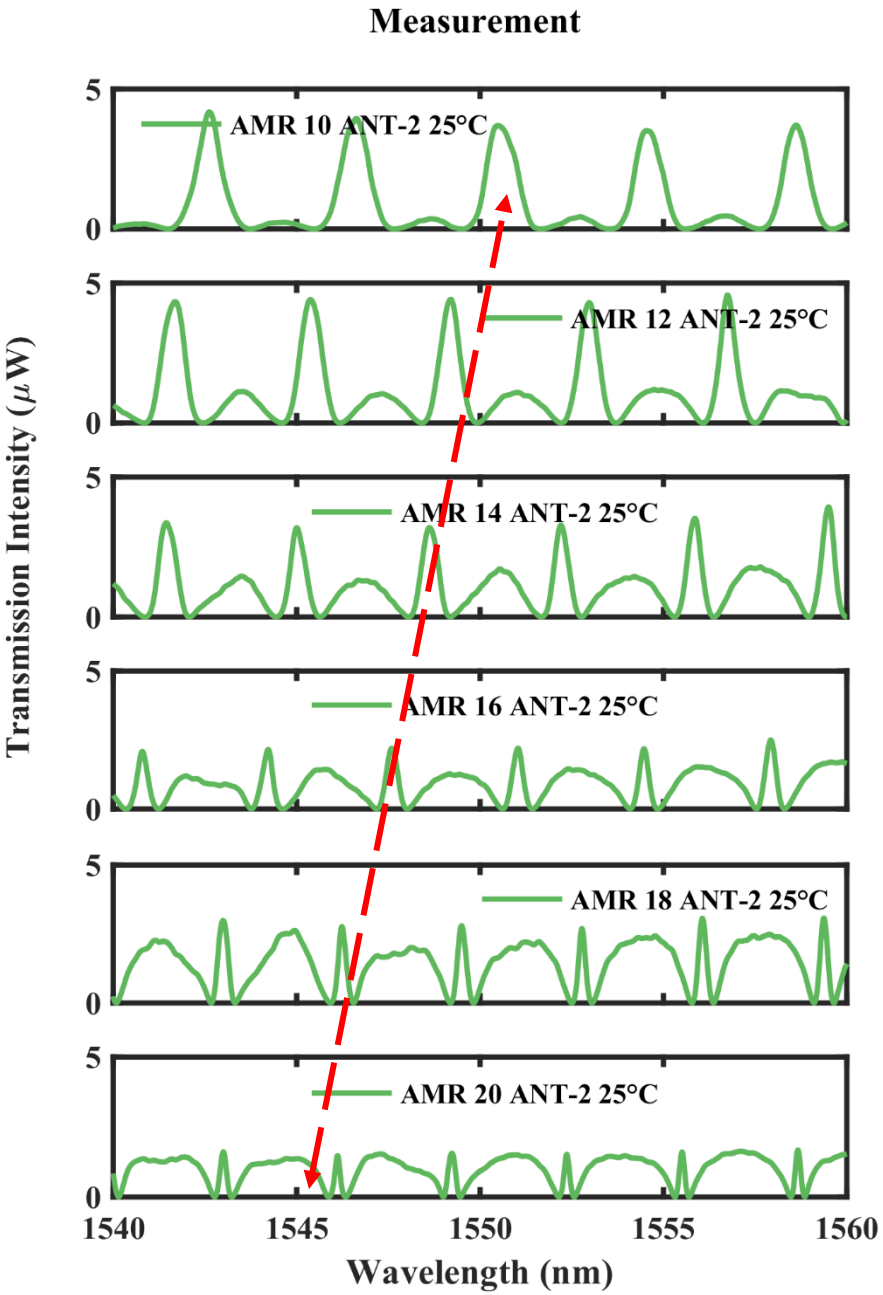

Figure 3.37: Measurement: Normalized transmission intensities of AMR Lc, with coupling lengths Lc varying from 10 μm to 20 μm, modulated with grating couplers.

3.5 AMR with Asymmetric DCs

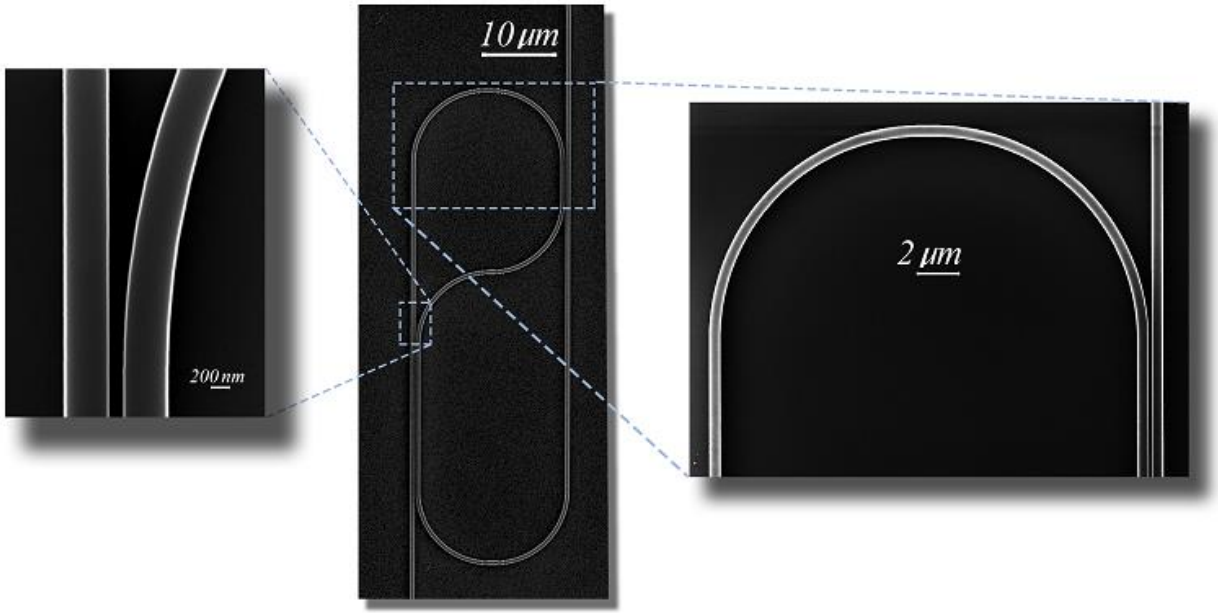

Figure 3.38: SEM of an asymmetric AMR Lc1 vs Lc2 constituting two directional couplers of different lengths Lc1 and Lc2.

The geometric path length can be written as follows:

$$AMR\ Lc1\ vs\ Lc2 = 2(R(\pi + 2) + Lc1 + Lc2 + g) \tag{3.4}$$

In the following section we investigate the AMR constituting of two DCs of different coupling lengths. Figure 3.39 shows the normalized transmission intensities in decibel scale (dB) of AMR with asymmetric DCs where, Lc1 = 0 μm, and Lc2 varying from 15 μm to 35 μm. In the transmission spectrum of AMR 0vs15, at the wavelength of 1550 nm, we start to observe the CRIT like effect. By tuning the wavelength further at around 1570 nm the induced transparency peak reaches the maximum value. The transmission spectra of AMR can achieve different line shapes at different coupling values, these effects in the transmission spectra of AMR devices can be explored in sensing and communication applications to achieve bandwidths of operations which are not limited by the FSR value.

The dashed red and green lines in Figure 3.39 indicates the maximum and minimum reflectivity values of MLM Lc2 respectively, these slopes were also discussed in Figure 3.11.

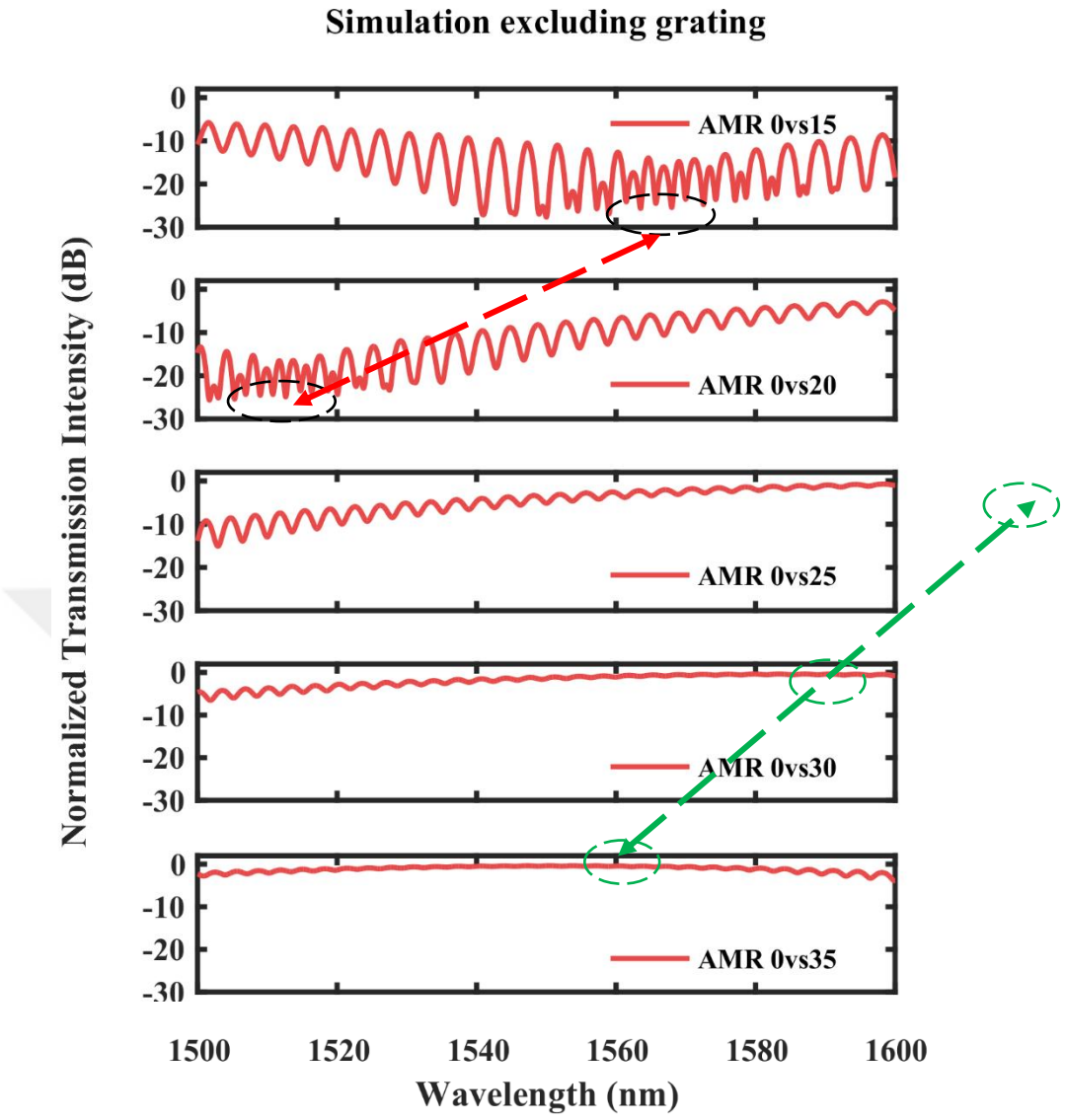

Figure 3.39: Simulation: Normalized transmission intensities in decibel scale (dB) of AMR Lc1 vs Lc2 constituting of asymmetric DCs Lc1 = 0 µm, and Lc2 varying from 15 µm to 35 µm.

Figure 3.40 shows the measurement spectra of the transmission intensities in decibel scale (dBm) of AMR constituting of asymmetric DCs, with coupling lengths Lc1 0 µm and Lc2 varying from 15 µm to 35 µm. The measurement spectra are blue-shifted by approximately 8 nm compared to the simulation. Since the measurements were taken at a temperature of 30 Celsius, these shifts are attributed to the fabrication and thermal variations. Overall the response of the AMR Lc1 vs Lc2 devices shows a good agreement between the simulations and measurements.

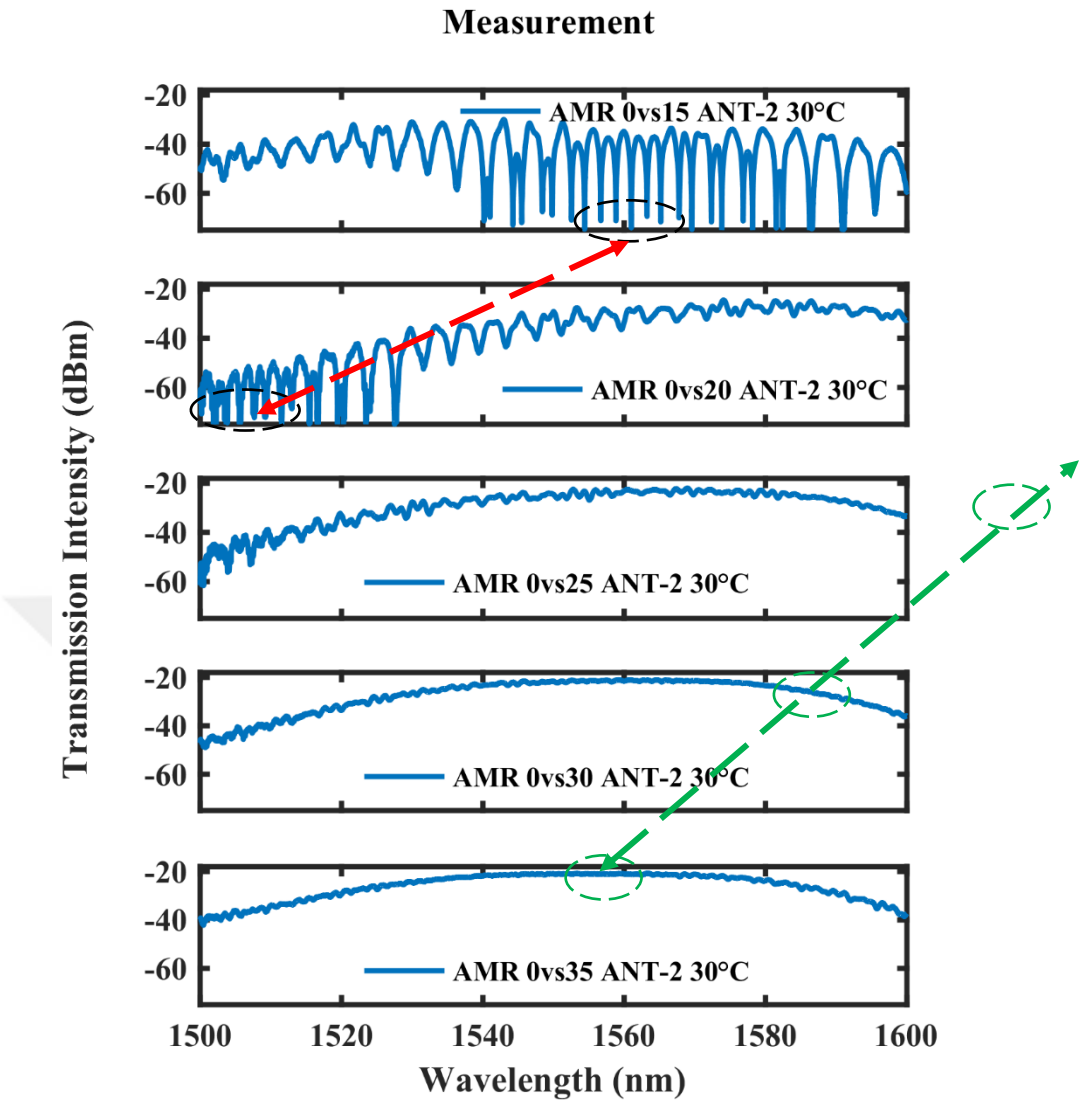

Figure 3.40: Measurement: Transmission intensities in decibel scale (dBm) of AMR Lc1 vs Lc2 constituting of asymmetric DCs, with coupling lengths Lc1 = 0 µm and Lc2 varying from 15 µm to 35 µm.

When the total interaction length of the DCs in AMR are increased the process of conversion of modes become slower, this is related to the tuning of the coupling of the coefficient. In Figure 3.41, simulation results for normalized transmission intensities in decibel scale (dB) of AMR constituting of asymmetric DCs, with coupling lengths Lc1 fixed to 5 µm and Lc2 varying from 15 µm to 40 µm are plotted. While tuning the wavelength from 1500 nm to 1600 nm, the AMR 5 vs 15 shows a mode being converted to a high Q factor values and is pushed by the

new mode rising in the middle of two resonant modes. Eventually the power is completely transferred to the new mode as is the case in AMR 5 vs 20 at around 1560 nm.

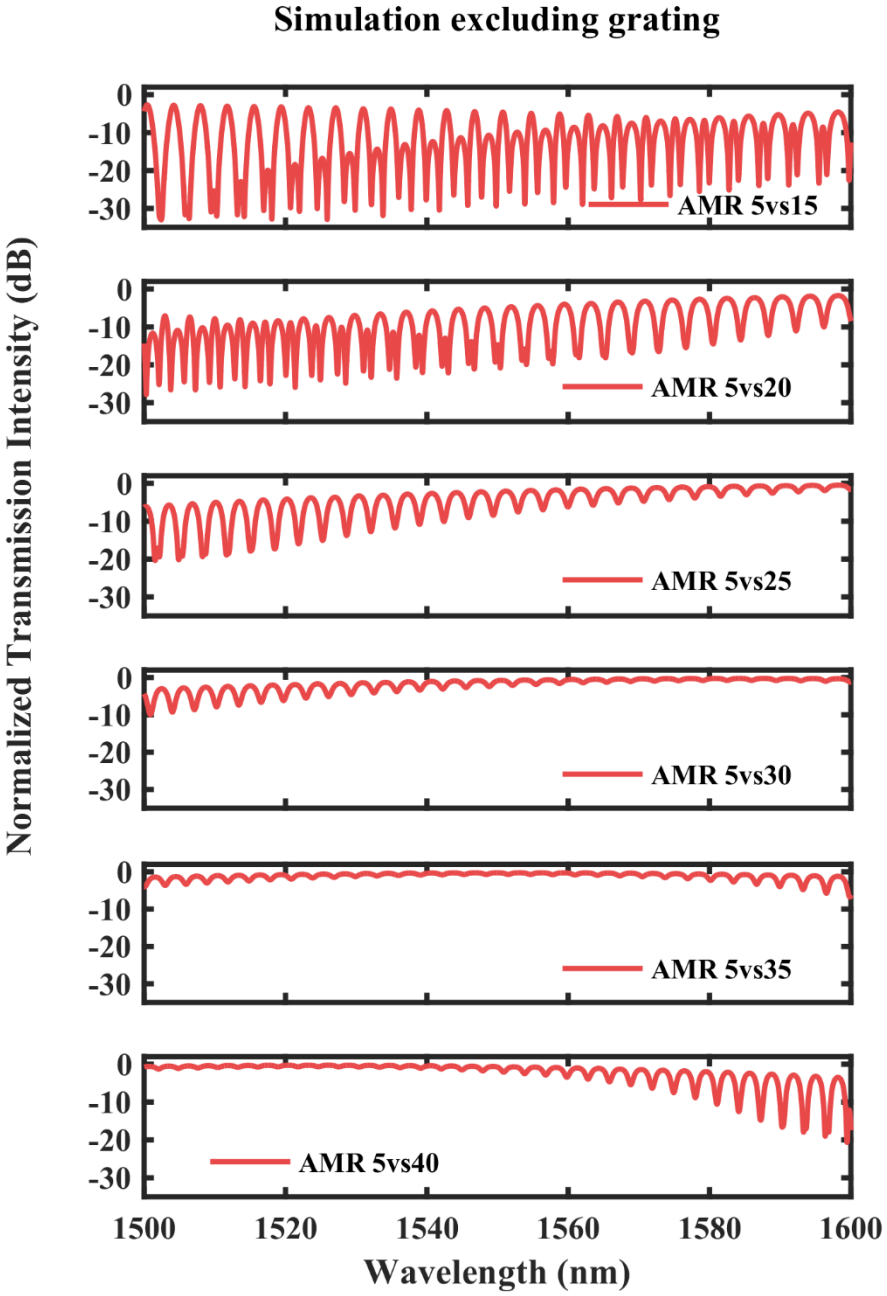

Figure 3.41: Simulation: Normalized transmission intensities in decibel scale (dB) of AMR Lc1 vs Lc2 constituting of asymmetric DCs, with coupling lengths Lc1 = 5 μm and Lc2 varying from 15 μm to 40 μm.

Figure 3.42, show the measured spectra of the devices coupled with the grating response. The power conversion from one family of modes to the other family of modes are consistent with the simulation spectra. The FSR values are also comparable with the theoretical values.

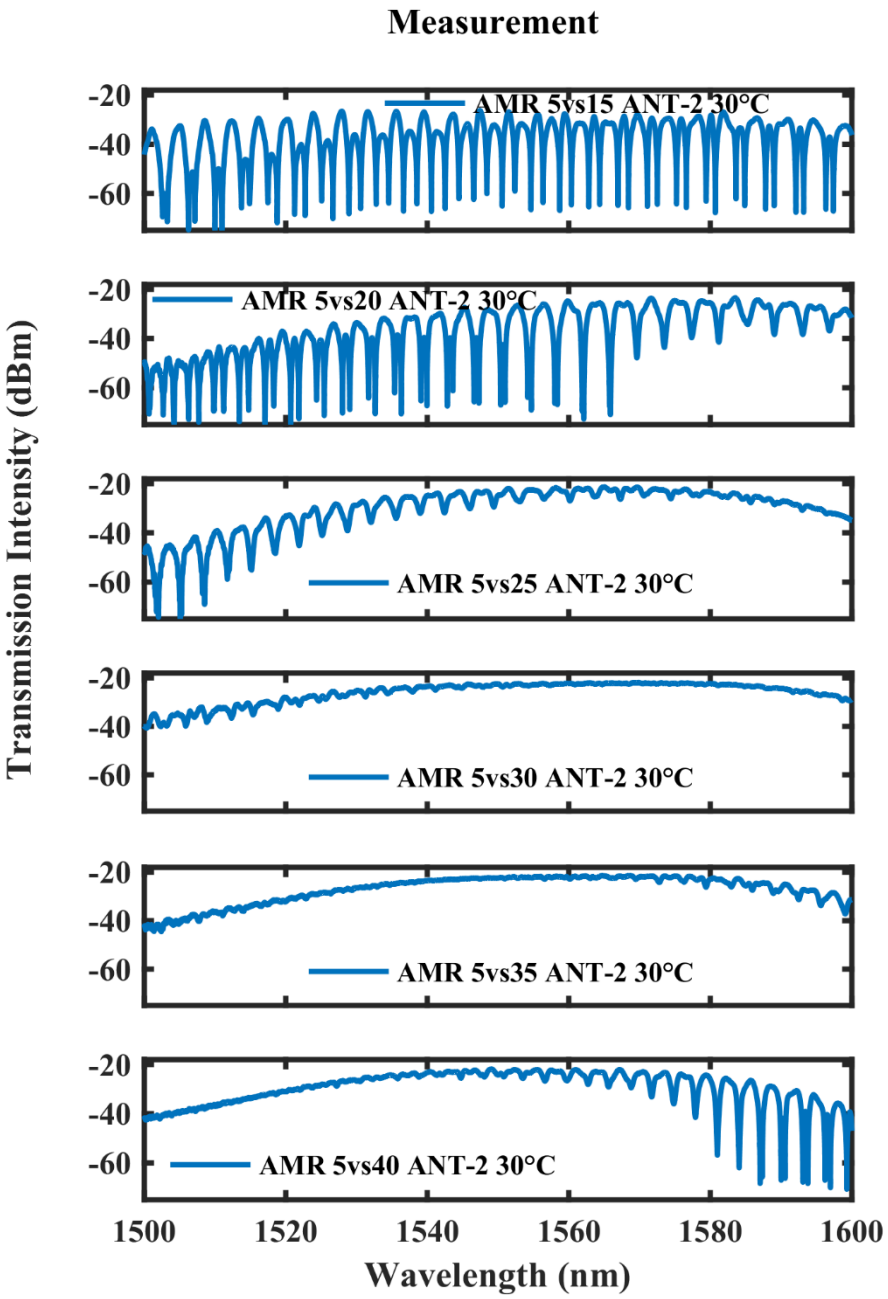

Figure 3.42: Measurement: Normalized transmission intensities in decibel scale (dB) of AMR Lc1 vs Lc2 constituting of asymmetric DCs, with Lc1 = 5 µm, and Lc2 varying from 15 µm to 40 µm.

Figure 3.43 show the simulated spectra of normalized transmission intensities in decibel scale (dB) of AMR constituting of asymmetric DCs with Lc1 fixed at 10 µm, and Lc2 varying from 15 µm to 35 µm. The FSR for this set of devices is smaller compared to the previous case, this is the effect of increasing the DC's interaction lengths. The mode seems to be high Q compared to the previous devices.

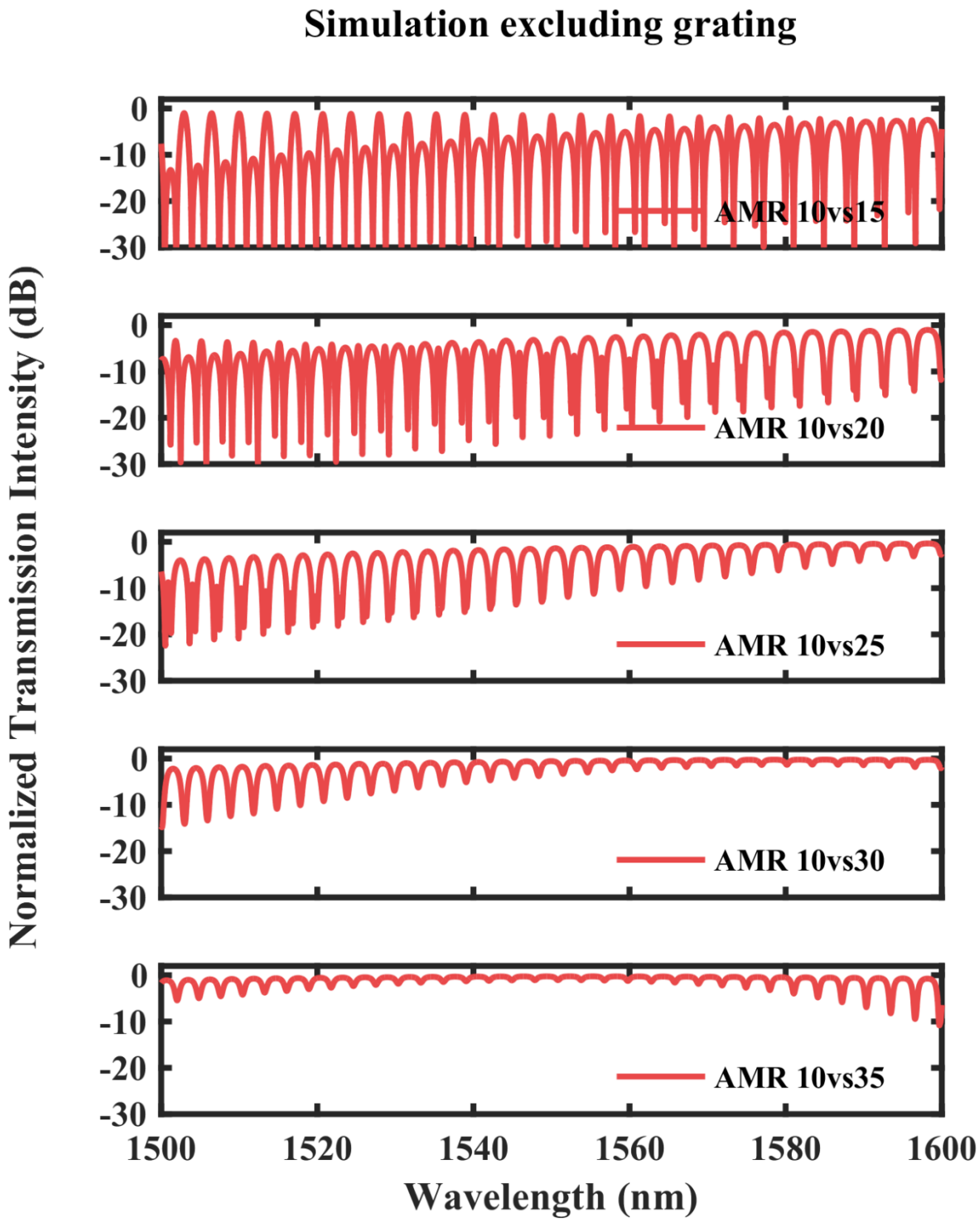

Figure 3.43: Simulation: Normalized transmission intensities in decibel scale (dB) of AMR Lc1 vs Lc2 constituting of asymmetric DCs with Lc1 fixed at 10 μm, and Lc2 varying from 15 μm to 35 μm.

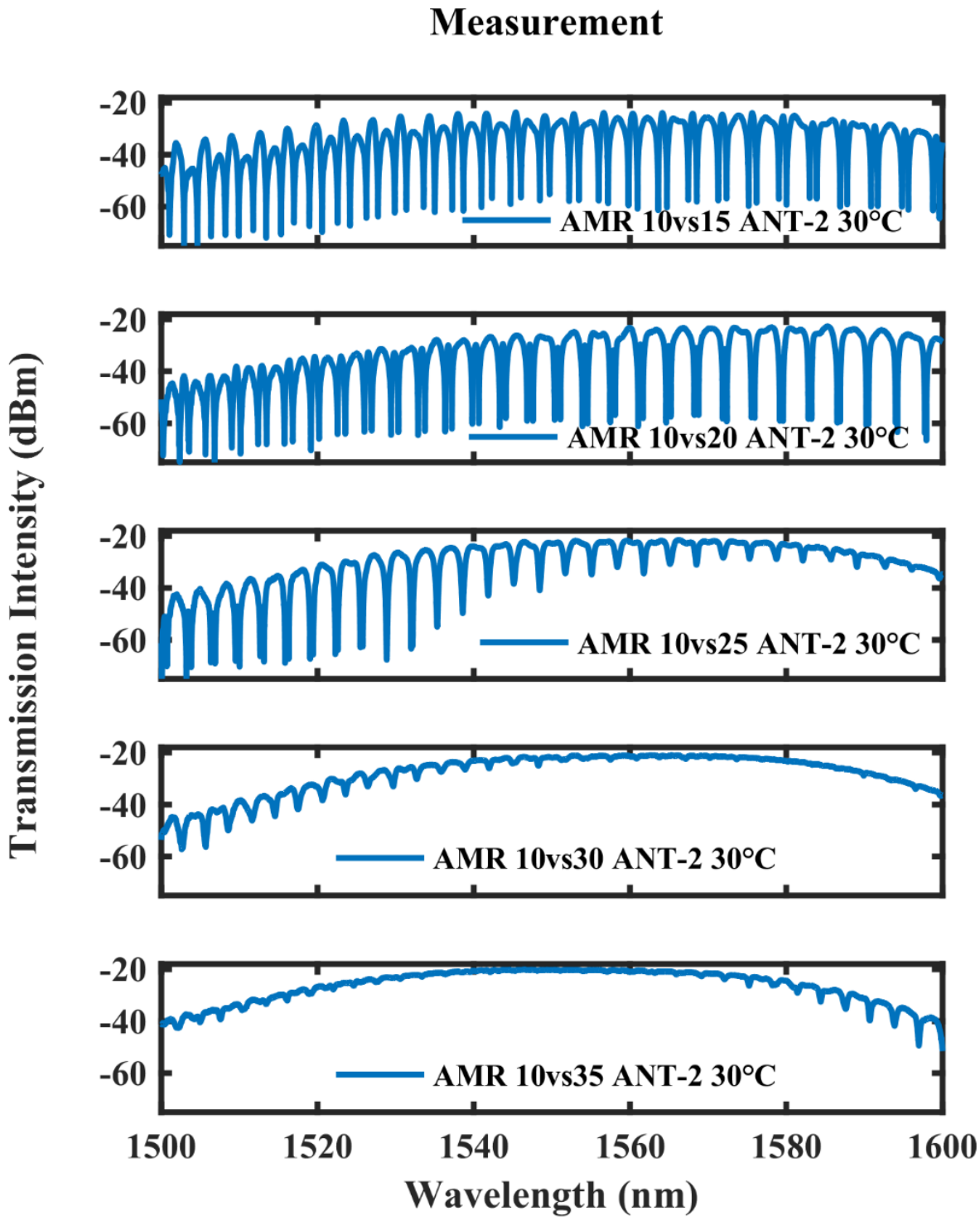

Figure 3.44: Measurement: Normalized transmission intensities in decibel scale (dB) of AMR Lc1 vs Lc2 constituting of asymmetric DCs, with coupling lengths Lc1 = 10 μm, and Lc2 varying from 15 μm to 35 μm.

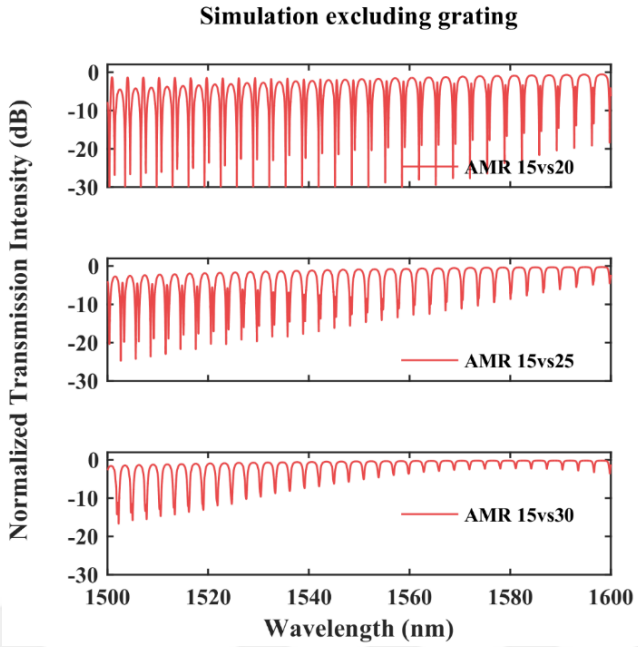

Figure 3.45: Simulation: Normalized transmission intensities in decibel scale (dB) of AMR Lc1 vs Lc2 constituting of asymmetric DCs, with coupling lengths Lc1 = 15 µm, and Lc2 varying from 20 µm to 30 µm.

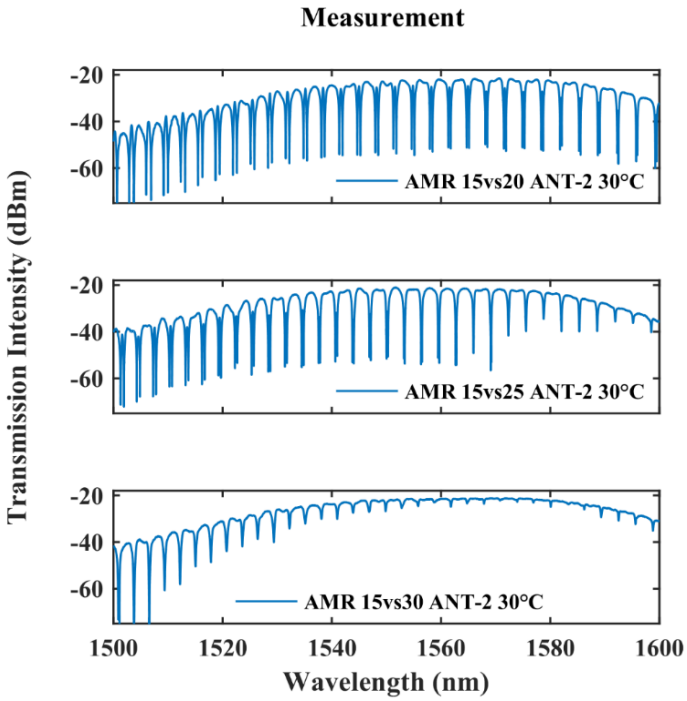

Figure 3.46: Measurement: Normalized transmission intensities in decibel scale (dB) of AMR Lc1 vs Lc2 constituting of asymmetric DCs, with coupling lengths Lc1 = 15 µm, and Lc2 varying from 20 µm to 30 µm.

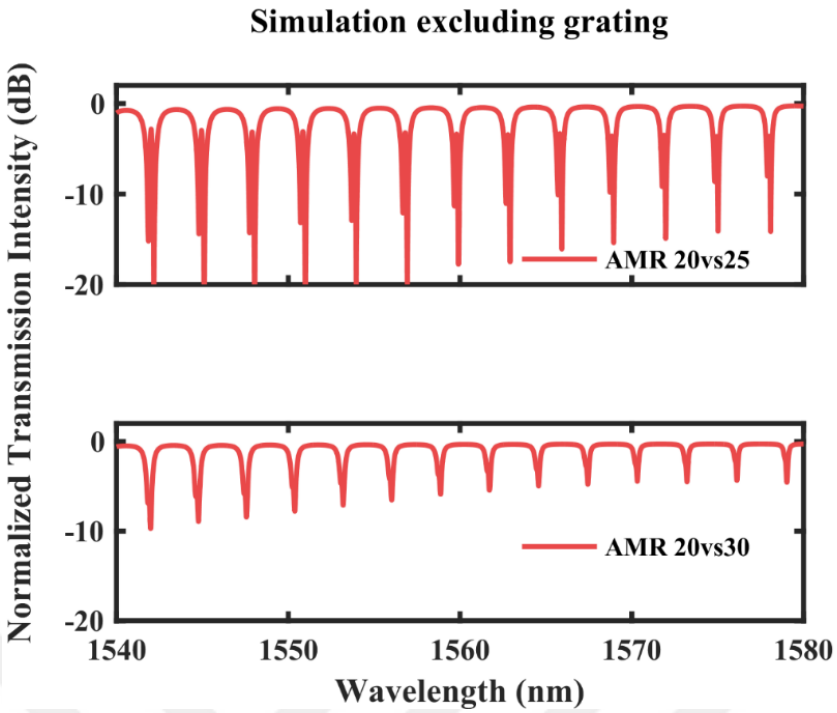

Figure 3.47: Simulation: Normalized transmission intensities in decibel scale (dB) of AMR with asymmetric DCs Lc1 20 µm, with coupling lengths Lc2 varying from 25 µm to 30 µm.

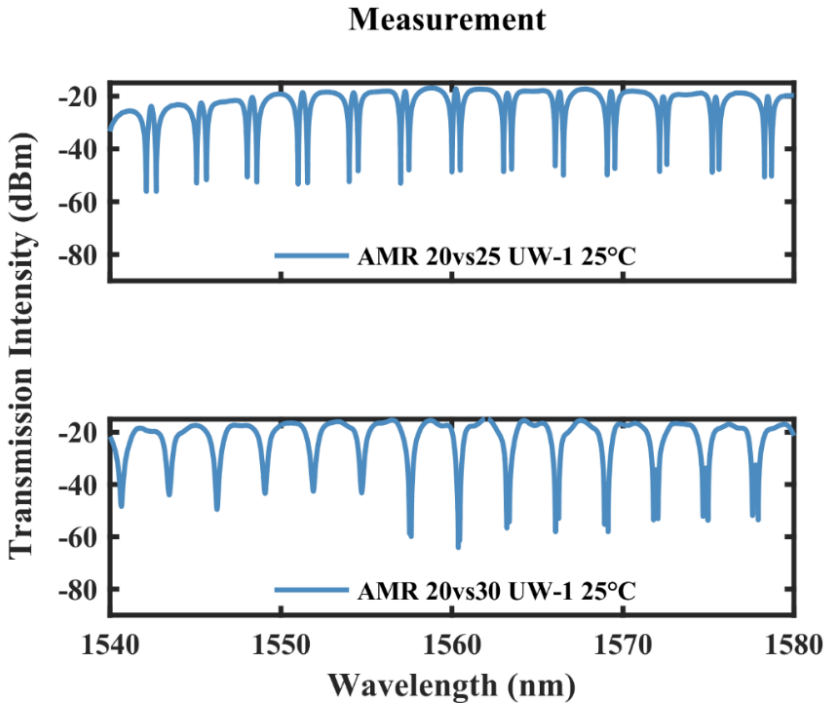

Figure 3.48: Measurement: Normalized transmission intensities in decibel scale (dB) of AMR with asymmetric DCs Lc1 20 µm, with coupling lengths Lc2 varying from 25 µm to 30 µm.

The cases plotted in Figure 3.45 to Figure 3.48 show the spectra of AMR Lc1 vs Lc2 devices with variations in directional couplers. In general we observe that the FSR is inversely proportional to the total interaction lengths of DCs, i.e., Lc1 + Lc2, whereas the Q factor can be tuned by selecting different coupling values. The CRIT like effect is also observed in the spectra by tuning the coupling of DCs. The Q factor values observed in AMR cases can be higher than the Lorentzian line shapes, observed in the MR case. The tenability of the CRIT mode and the energy transfer from one resonant family to the other, which pushes the existing resonant modes to high Q factor values.

The transmission spectra of AMR can achieve different line shapes at different coupling values, these effects in the transmission spectra of AMR devices can be explored in sensing and communication applications to achieve bandwidths of operations which are not limited by the FSR value.

3.6 Symmetric meandering resonator (SMR)

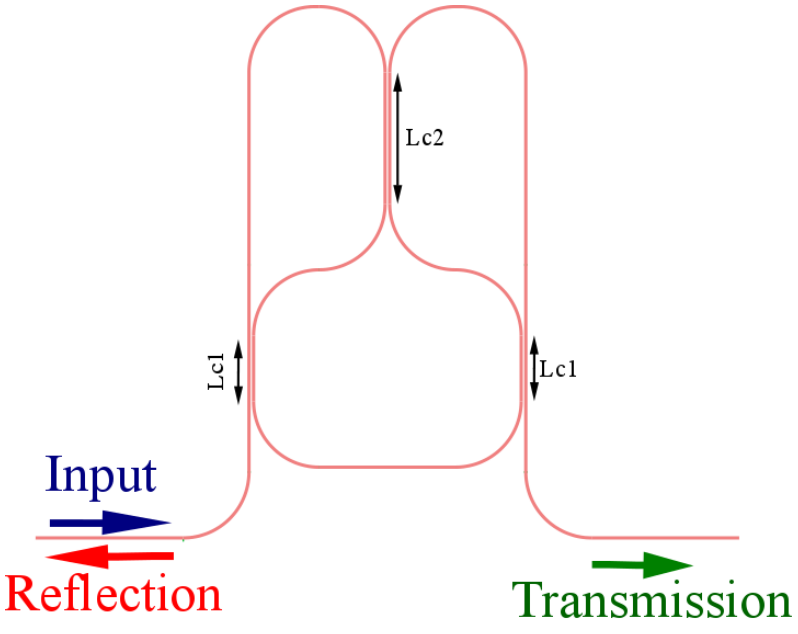

Figure 3.49: (SMR Lc1 vs Lc2) consisting of two couplers of lengths of Lc1 and one coupler of length Lc2.

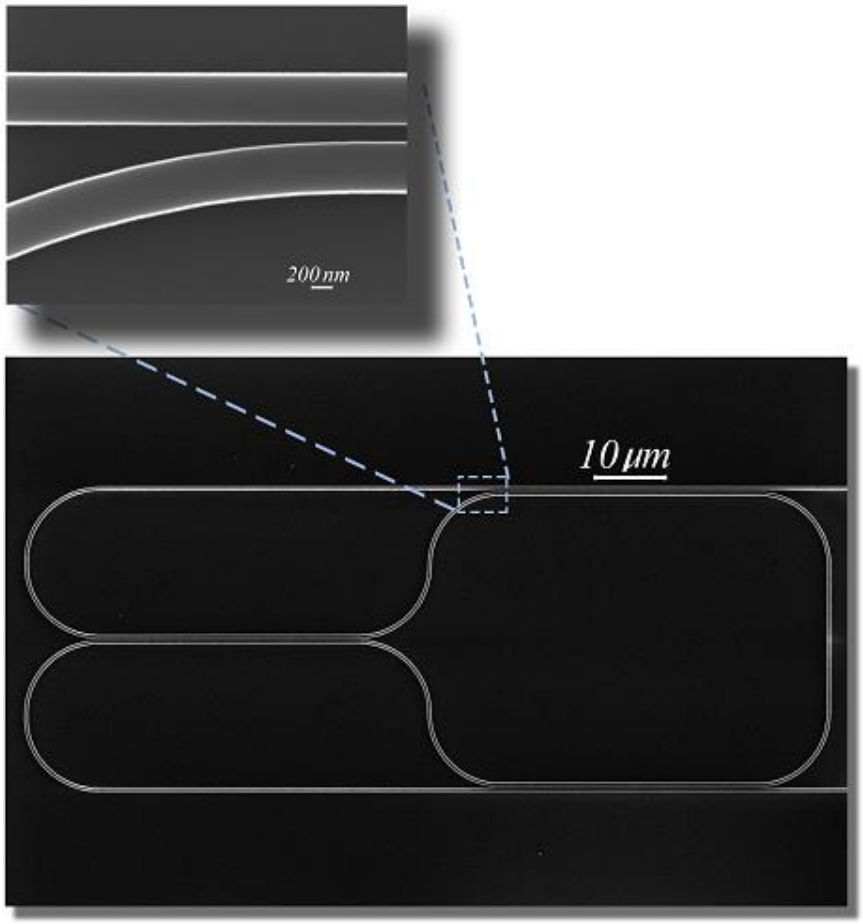

Figure 3.50: SEM of SMRs consisting of three directional couplers of same lengths.

Figure 3.49 and Figure 3.50 shows a layout and SEM of a SMR, respectively. Lc1 and Lc2 are the coupling lengths of the DCs, and R is the bending radius, which for our case is equal to 10 μm. SMR Lc denotes the case, where all the couplers have equal coupling lengths, i.e., Lc1 = Lc2.

SMR is a higher order AMR. If considered as a filter, the response of a higher order filter becomes closer to the ideal box shape. The SMR has a richer spectrum with mode splitting of tunable Fano and Lorentzian lineshapes. These responses make the SMR an ideal candidate for designing optical filters. Compared to the coupled ring resonators, SMRs have inherent thermal compensation mechanism, which eliminates the need to actively tuning the resonator to match the resonance mode in case of a thermal variation on the chip.

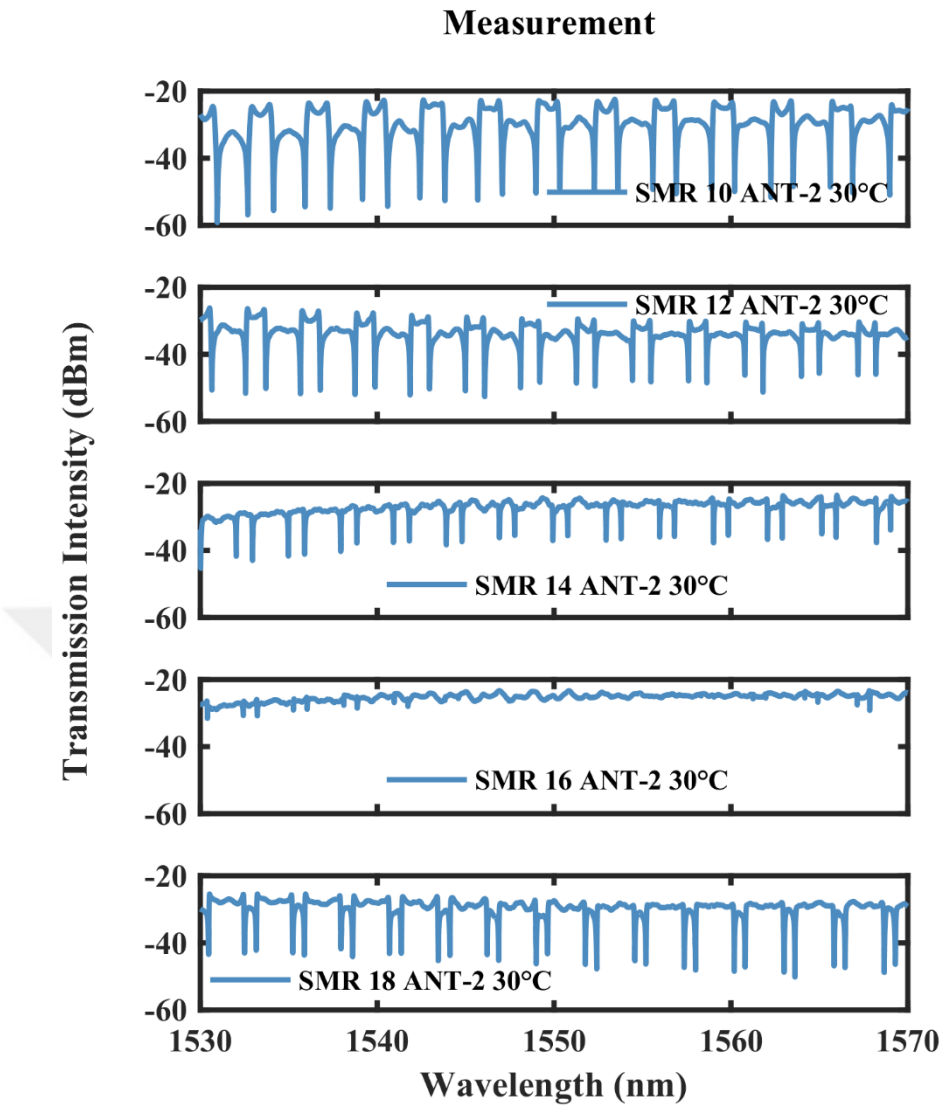

Figure 3.51: Measurement: Normalized transmission intensities in decibel scale (dBm) of SMR Lc, with coupling lengths Lc varying from 10 μm to 18 μm, modulated with grating couplers.

Spectra shown in Figure 3.51 and Figure 3.52 are the measured transmission intensities of SMR 10 to SMR 18, in dB and linear (μW) scale, respectively, for the chip-2 fabricated at the ANT. These spectra were scanned for the wavelength range of 1500 nm to 1600 nm, whereas the plotted range is from 1530 nm to 1570 nm Figure 3.7. The FSR of the spectrum is decreased, as we move from SMR with Lc = 10 μm to 18 μm. mode splitting gets decreased, while the Q-factor of the peaks is increased.

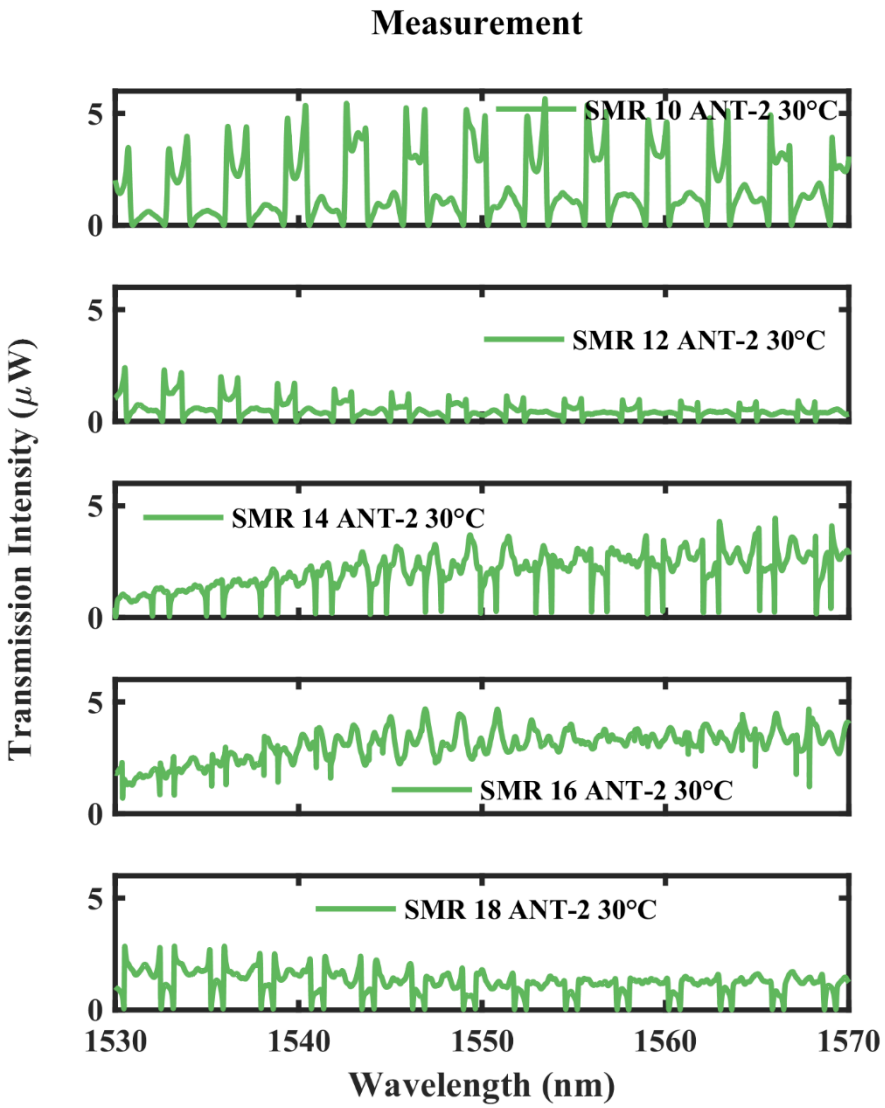

Figure 3.52: Measurement: Normalized transmission intensities of SMR Lc, with coupling lengths Lc varying from 10 μm to 18 μm, modulated with grating couplers.

The results demonstrate that, active tuning of SMR based optical filters can be achieved by coupling the device with electrical control circuits.

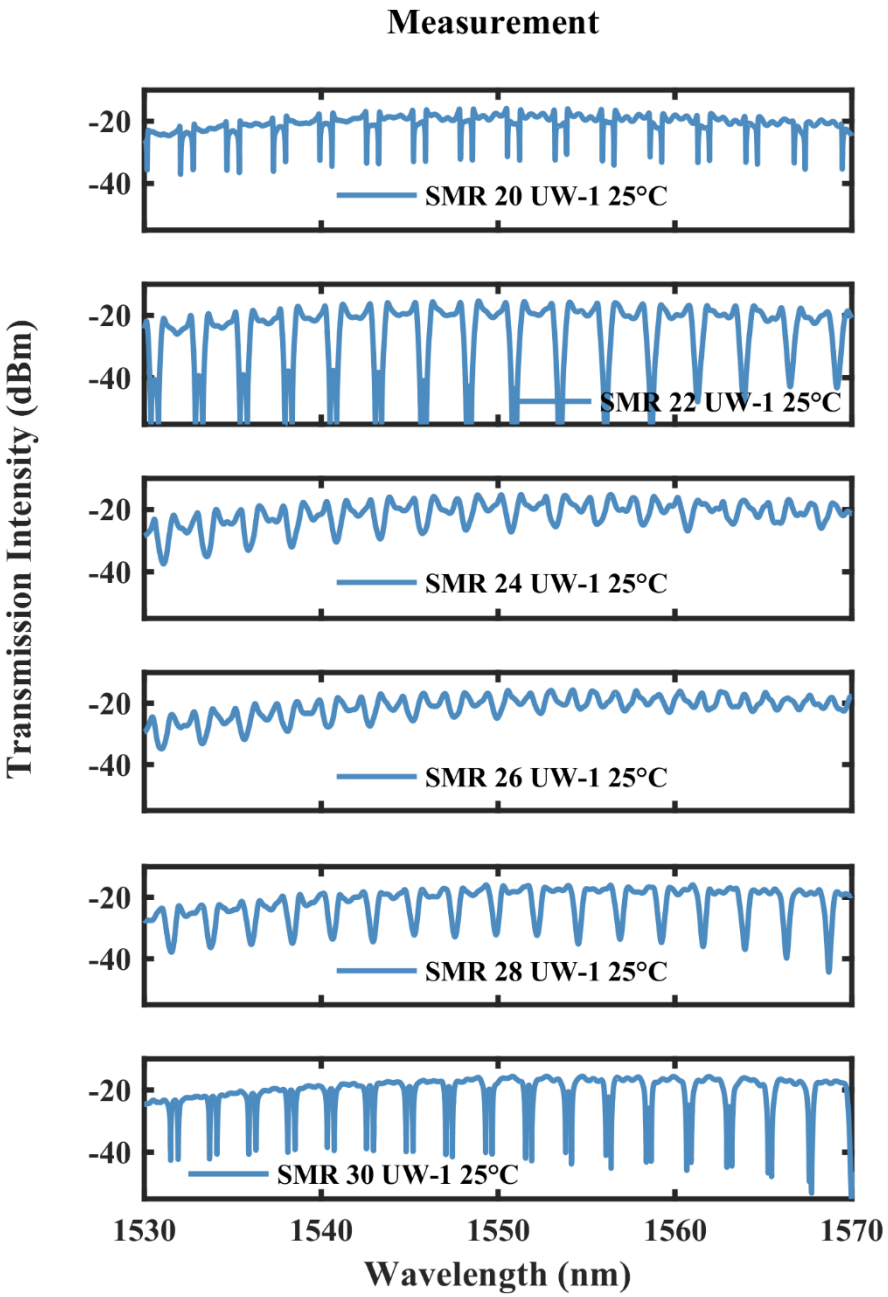

Figure 3.53: Measurement: Normalized transmission intensities in decibel scale (dBm) of SMR Lc, with coupling lengths Lc varying from 20 µm to 30 µm, modulated with grating couplers.

In Figure 3.53 and Figure 3.54 the transmission intensities of the SMR 20 to SMR 30 are plotted.

SMR22 shows the highest extinction ratios (ERs), which are desirable for interleaving.

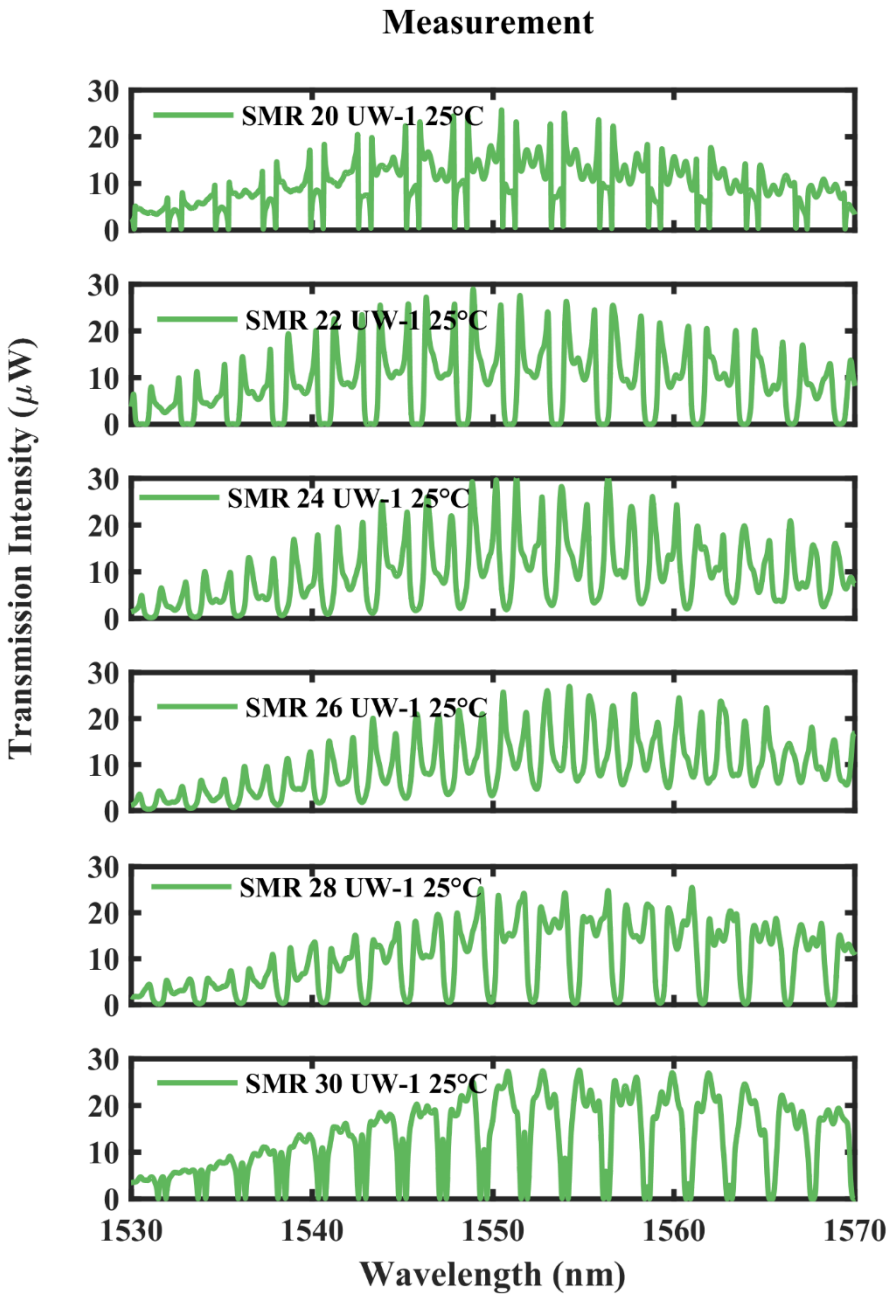

Figure 3.54: Measurement: Normalized transmission intensities of SMR Lc, with coupling lengths Lc varying from 20 μm to 30 μm, modulated with grating couplers.

4 Conclusions and future work

Meandering Loop Mirrors (MLMs) and resonators based on MLMs are designed, fabricated, and analyzed using silicon integrated photonics technology for operation in the standard near-infrared (near-IR) telecommunication band.

Optical waveguides, directional couplers (DCs), MLMs, meandering resonators (MRs), antisymmetric meandering resonators (AMRs), and symmetric meandering resonators (SMRs) with symmetric and antisymmetric DCs were designed, fabricated, and analyzed as a function of the DC length to scan the desired near-infrared (near-IR) telecommunication band. The free spectral range (FSR), finesse, quality factor (Q-factor), and extinction ratio (ER) are deduced from both the experimentally measured, and the numerically simulated transmission spectra, and were found to be in good agreement.

We analyzed the wavelength dependence of a DC, the DC is one of the basic elements used in our designs. We looked at the coupled and the transmitted port intensities, and compared them with the measurement results. These DCs were chosen for designing the meandering elements because the wavelength sweep would correspond to the tuning due to coupling of the devices. Then we studied the MLM spectral response, which incorporates a DC. After developing the basic understanding of DC and the MLM, we analyzed the spectral responses of more complex structures, e.g., MR, AMR, and SMR.

The resonance observed in the spectrum of de-embedding structure is due to the FP effect created by the reflections from the input and the output grating couplers. The free spectral range FSR for the simulated structure is 1.88 nm, which matches with the theoretical FSR value of

1.9 nm for a waveguide length of 160 μm with a group index of 4. The interference in MLM 10 (excluding grating) structure creates a pattern with a simulated FSR of 4.3 nm. Since the dynamic range of the interference is small compared to the FP effect, the change produced by this effect is not making a significantly visible modulation in the spectrum. The FP effect in MLM 10 (with gratings) with a smaller FSR of 1.6 nm is due to the reflections from the gratings. The FSR is smaller than the de-embedding structure's FSR of 1.8 nm, because of longer optical path length introduced by the MLM 10 itself.

The general response of a tunable mirror was observed for the MLMs, where the dip corresponds to the maximum reflectivity of the mirror. The dip position shifted, when the coupling length of the DC was varied. Contrary to the dips, the peaks were more prominent in the normalized transmission spectra of MLMs. The two different slopes in the MLM spectra indicate that, the couplers was mismatched and a chirp was observed in the coupling. The simulation results for the transmission intensities of the MR structures showed a Fabry-Pérot like behavior. At the maximum reflectance points of the MLM, the Q-factor was observed to be maximum. Maximum Q-factors of around $5x10^4$ was observed in MRs, whereas the maximum finesse (F) reaches 30. Extinction ratios are sensitive to the reflectance of the MLMs, and become worse at the high reflectance values of the mirror. The FSR ranges from 1.25 nm to 1.7 nm for our fabricated MR devices.

We have designed and analyzed the AMRs with both symmetric DCs (AMR Lc) and asymmetric DCs (AMR Lc1 vs Lc2). The AMRs showed a typical response which is similar to the coupled resonator induced transparency (CRIT), the analogue of the electromagnetically induced transparency (EIT), spectral response.

The resonance peaks move towards higher quality factor values as the coupling is increased. A shift in the resonance condition was observed due to the variation in the optical path length introduced by different coupling lengths of the directional couplers.

We plotted the intensities of AMR connected to the input and output grating couplers, for Lc = Lc1 = Lc2, where Lc is varied from 10 to 40 μm. In the measured spectra of the AMR, the resonant peak positions are shifted by 5 nm, which is attributed to the fabrication variations in lithography process of the devices. Calculated FSRs for the measurements are in accordance with the simulations. Overall we see a good agreement between the simulations and the measurements. To distinguish the resonance peaks from the side lobes, we have plotted the normalized intensities of the simulated and the measured spectra.

For the case of asymmetric DCs in AMR Lc1 vs Lc2 devices we studied the spectral responses with variations in directional coupler lengths. In general we observe that the FSR is inversely proportional to the total interaction lengths of DCs, i.e., Lc1 + Lc2, whereas the Q factor can be tuned by selecting different coupling values. The CRIT like effect is also observed in the spectra by tuning the coupling of DCs. The Q factor values observed in AMR cases can be higher than the Lorentzian line shapes, observed in the MR case. The tenability of the CRIT mode and the energy transfer from one resonant family to the other, which pushes the existing resonant modes to high Q factor values.

The transmission spectra of AMR can achieve different line shapes at different coupling values, these effects in the transmission spectra of AMR devices can be explored in sensing and communication applications to achieve bandwidths of operations which are not limited by the FSR value.

The SMR has a richer spectrum with mode splitting of tunable Fano and Lorentzian lineshapes. These responses make the SMR an ideal candidate for designing optical filters. Compared to

the coupled ring resonators, SMRs have inherent thermal compensation mechanism, which eliminates the need to actively tuning the resonator to match the resonance mode in case of a thermal variation on the chip. The results demonstrate that, active tuning of SMR based optical filters can be achieved by coupling the device with electrical control circuits.

All in all, MLMs and resonators based on MLMs show promise as a novel silicon photonic integrated circuit (Si-PIC) platform for optical communication, computation, and sensing.

Curriculum Vita

Muhammad Zakwan received his B.Sc. in Electrical Engineering, from Air University, Islamabad. He obtained his M.Sc. in Communication and Information Systems from Northwestern Polytechnic University, Xi'an.

After his M.Sc. degree, he was appointed as a lecturer at Air University. During 2013 and 2017 he joined Microphotonics Research laboratory as a research assistant completed his Ph.D. in Electrical and Electronics Engineering at Koç University, Istanbul.

His research interests include group IV photonics, Silicon photonic integrated circuits (Si-PICs), lasers, optical microcavities, semiconductor device physics, integrated circuit design, communication systems, mobile Ad-hoc networks, sensor networks, and control systems.

Publications

1. U. Sabahattin Gökay, M. Zakwan, A. Demir, and A. Serpengüzel, "Optical Fiber Excitation of Fano Resonances in a Silicon Microsphere," Fiber and Integrated Optics, vol. 35, no. 1, pp. 38-46, 2016

2. U. Sabahattin Gökay, M. Zakwan, and A. Serpengüzel, "Spherical silicon optical resonators: Possible applications to biosensing," European Physical Journal-Special Topics, vol. 223, no. 10, pp. 2003-2008, 2014.

3. O. M. Öztürk, M. M. Bayer, M. S. Anwar, M. Zakwan, and A. Serpengüzel, "Spectroscopy of a Nd:YVO4 diode pumped solid state laser," Microwave and Optical Technology Letters, vol. 59, no. 7, pp. 1636-1639, 2017.

References

[1] K. C. Kao, and G. A. Hockham, “Dielectric-fibre surface waveguides for optical frequencies,” *Proceedings of the Institution of Electrical Engineers,* vol. 113, no. 7, pp. 1151-1158, 1966.

[2] V. Singh, P. T. Lin, N. Patel, H. Lin, L. Li, Y. Zou, F. Deng, C. Ni, J. Hu, J. Giammarco, A. P. Soliani, B. Zdyrko, I. Luzinov, S. Novak, J. Novak, P. Wachtel, S. Danto, J. D. Musgraves, K. Richardson, L. C. Kimerling, and A. M. Agarwal, “Mid-infrared materials and devices on a Si platform for optical sensing,” *Science and Technology of Advanced Materials,* vol. 15, no. 1, pp. 014603, 2014.

[3] T. Liljeberg, "Silicon photonics and the future of optical connectivity in the data center," *in Proceedings of IEEE Optical Interconnects Conference,* A. Ghiasi and I. E. Lyubomirsky (Eds.), 2017, pp. 1-2.

[4] A. Boletti, D. Giacomuzzi, G. Parladori, P. Boffi, M. Ferrario, and M. Martinelli, “Performance comparison between electrical copper-based and optical fiber-based backplanes,” *Optics Express,* vol. 21, no. 16, pp. 19202-19208, 2013.

[5] D. A. B. Miller, “Device Requirements for Optical Interconnects to Silicon Chips,” *Proceedings of the IEEE,* vol. 97, no. 7, pp. 1166-1185, 2009.

[6] L. Chrostowski, and M. Hochberg, *Silicon photonics design: from devices to systems*, Cambridge University Press, Cambridge, 2015.

[7] R. Soref, “The Past, Present, and Future of Silicon Photonics,” *IEEE Journal of Selected Topics in Quantum Electronics,* vol. 12, no. 6, pp. 1678-1687, 2006.

[8] W. Bogaerts, S. K. Selvaraja, P. Dumon, J. Brouckaert, K. D. Vos, D. V. Thourhout, and R. Baets, “Silicon-on-Insulator Spectral Filters Fabricated With CMOS Technology,” *IEEE Journal of Selected Topics in Quantum Electronics,* vol. 16, no. 1, pp. 33-44, 2010.

[9] M. Asghari, and A. V. Krishnamoorthy, “Silicon photonics: Energy-efficient communication,” *Nature Photonics,* vol. 5, no. 5, pp. 268-270, 2011.

[10] L.-S. Wang, H. Wu, S. R. Desai, J. Fan, and S. D. Colson, “A Photoelectron Spectroscopic Study of Small Silicon Oxide Clusters: SiO2, Si2O3, and Si2O4,” *The Journal of Physical Chemistry,* vol. 100, no. 21, pp. 8697-8700, 1996.

[11] H. M. Jennings, B. J. Dalgleish, and P. L. Pratt, “Reactions between silicon and nitrogen,” *Journal of Materials Science,* vol. 23, no. 7, pp. 2573-2583, 1988.

[12] A. H. Cowley, and R. A. Jones, “Single-Source III/V Precursors: A New Approach to Gallium Arsenide and Related Semiconductors,” *Angewandte Chemie International Edition in English,* vol. 28, no. 9, pp. 1208-1215, 1989.

[13] W. Bogaerts, P. De Heyn, T. Van Vaerenbergh, K. De Vos, S. Kumar Selvaraja, T. Claes, P. Dumon, P. Bienstman, D. Van Thourhout, and R. Baets, “Silicon microring resonators,” *Laser and Photonics Reviews,* vol. 6, no. 1, pp. 47-73, 2012.

[14] W. M. J. Green, M. J. Rooks, L. Sekaric, and Y. A. Vlasov, “Ultra-compact, low RF power, 10 Gb/s silicon Mach-Zehnder modulator,” *Optics Express,* vol. 15, no. 25, pp. 17106-17113, 2007.

[15] Z. Lu, J. Jhoja, J. Klein, X. Wang, A. Liu, J. Flueckige, J. Pond, and L. Chrostowski, “Performance prediction for silicon photonics integrated circuits with layout-dependent correlated manufacturing variability,” *Optics Express,* vol. 25, no. 9, pp. 9712-9733, 2017.

[16] C. Doerr, L. Chen, D. Vermeulen, T. Nielsen, S. Azemati, S. Stulz, G. McBrien, X. M. Xu, B. Mikkelsen, M. Givehchi, C. Rasmussen, and S. Y. Park, "Single-chip silicon photonics 100-Gb/s coherent transceiver," *in Proceedings of OSA Optical Fiber Communication Conference: Postdeadline Papers, paper Th5C.1*, C. Doerr, K.-i. Sato and K. E. Tse (Eds.), 2014, pp. 1-3.

[17] C. A. Brackett, “Dense wavelength division multiplexing networks: principles and applications,” *IEEE Journal on Selected Areas in Communications,* vol. 8, no. 6, pp. 948-964, 1990.

[18] A. Liu, L. Liao, Y. Chetrit, J. Basak, H. Nguyen, D. Rubin, and M. Paniccia, “Wavelength Division Multiplexing Based Photonic Integrated Circuits on Silicon-on-Insulator Platform,” *IEEE Journal of Selected Topics in Quantum Electronics,* vol. 16, no. 1, pp. 23-32, 2010.

[19] A. Yariv, Y. Xu, R. K. Lee, and A. Scherer, “Coupled-resonator optical waveguide: a proposal and analysis,” *Optics Letters,* vol. 24, no. 11, pp. 711-713, 1999.

[20] B. E. Little, S. T. Chu, W. Pan, D. Ripin, T. Kaneko, Y. Kokubun, and E. Ippen, “Vertically coupled glass microring resonator channel dropping filters,” *IEEE Photonics Technology Letters,* vol. 11, no. 2, pp. 215-217, 1999.

[21] J. V. Hryniewicz, P. P. Absil, B. E. Little, R. A. Wilson, and P. T. Ho, "Higher order filter response in coupled microring resonators," *IEEE Photonics Technology Letters,* vol. 12, no. 3, pp. 320-322, 2000.

[22] S. Mookherjea, and A. Yariv, "Pulse propagation in a coupled resonator optical waveguide to all orders of dispersion," *Physical Review E,* vol. 65, no. 5, pp. 056601, 2002.

[23] J. E. Heebner, and R. W. Boyd, "SLOW AND STOPPED LIGHT 'Slow' and 'fast' light in resonator-coupled waveguides," *Journal of Modern Optics,* vol. 49, no. 14-15, pp. 2629-2636, 2002.

[24] S. Mookherjea, and A. Yariv, "Kerr-stabilized super-resonant modes in coupled-resonator optical waveguides," *Physical Review E,* vol. 66, no. 4, pp. 046610, 2002.

[25] K. Oda, N. Takato, H. Toba, and K. Nosu, "A wide-band guided-wave periodic multi/demultiplexer with a ring resonator for optical FDM transmission systems," *Journal of Lightwave Technology,* vol. 6, no. 6, pp. 1016-1023, 1988.

[26] Y. Zhang, W. Huang, X. Wang, H. Xu, and Z. Cai, "Design of flat-top interleaver and tunable dispersion compensator using cascaded Sagnac loop mirrors and ring resonators," *Applied Optics,* vol. 48, no. 32, pp. 6213-6222, 2009.

[27] J. Song, Q. Fang, S. H. Tao, M. B. Yu, G. Q. Lo, and D. L. Kwong, "Proposed silicon wire interleaver structure," *Optics Express,* vol. 16, no. 11, pp. 7849-7859, 2008.

[28] W. Bogaerts, P. Dumon, D. V. Thourhout, D. Taillaert, P. Jaenen, J. Wouters, S. Beckx, V. Wiaux, and R. G. Baets, "Compact Wavelength-Selective Functions in Silicon-on-Insulator Photonic Wires," *IEEE Journal of Selected Topics in Quantum Electronics,* vol. 12, no. 6, pp. 1394-1401, 2006.

[29] Y. Zhang, S. Yang, H. Guan, A. E.-J. Lim, G.-Q. Lo, P. Magill, T. Baehr-Jones, and M. Hochberg, "Sagnac loop mirror and micro-ring based laser cavity for silicon-on-insulator," *Optics Express,* vol. 22, no. 15, pp. 17872-17879, 2014.

[30] Y. Zhang, M. Streshinsky, A. Novack, Y. Ma, S. Yang, A. E.-J. Lim, G.-Q. Lo, T. Baehr-Jones, and M. Hochberg, "A compact and low-loss silicon waveguide crossing for O-band optical interconnect," *in Proceedings of SPIE Silicon Photonics IX*, J. Kubby and G. E. T. Reed (Eds.), 2014, pp. 899002-8.

[31] X. Tu, T.-Y. Liow, J. Song, X. Luo, Q. Fang, M. Yu, and G.-Q. Lo, "50-Gb/s silicon optical modulator with traveling-wave electrodes," *Optics Express,* vol. 21, no. 10, pp. 12776-12782, 2013.

[32] L. Vivien, A. Polzer, D. Marris-Morini, J. Osmond, J. M. Hartmann, P. Crozat, E. Cassan, C. Kopp, H. Zimmermann, and J. M. Fédéli, "Zero-bias 40Gbit/s germanium waveguide photodetector on silicon," *Optics Express,* vol. 20, no. 2, pp. 1096-1101, 2012.

[33] A. J. Zilkie, B. J. Bijlani, P. Seddighian, D. C. Lee, W. Qian, J. Fong, R. Shafiiha, D. Feng, B. J. Luff, X. Zheng, J. E. Cunningham, A. V. Krishnamoorthy, and M. Asghari, "High-efficiency hybrid III-V/Si external cavity DBR laser for 3-μm SOI waveguides," *in Proceedings of IEEE 9th International Conference on Group IV Photonics*, vol. 13058961, M. Asghari and J. Michel (Eds.), 2012, pp. 317-319.

[34] J. E. Fritts, and R. D. Chamberlain, "Breaking the memory bottleneck with an optical data path," *in Proceedings of IEEE 35th Annual Simulation Symposium*, E. E. Karatza (Eds.), 2002, pp. 352-362.

[35] D. A. B. Miller, "Fundamental limit for optical components," *Journal of the Optical Society of America B,* vol. 24, no. 10, pp. A1-A18, 2007.

[36] J. Witzens, "Silicon photonics: Modulators make efficiency leap," *Nat Photon,* vol. 11, no. 8, pp. 459-462, 2017.

[37] L.-W. Luo, S. Ibrahim, A. Nitkowski, Z. Ding, C. B. Poitras, S. J. Ben Yoo, and M. Lipson, "High bandwidth on-chip silicon photonic interleaver," *Optics Express,* vol. 18, no. 22, pp. 23079-23087, 2010.

[38] Y. Wang, X. Wang, J. Flueckiger, H. Yun, W. Shi, R. Bojko, N. A. F. Jaeger, and L. Chrostowski, "Focusing sub-wavelength grating couplers with low back reflections for rapid prototyping of silicon photonic circuits," *Optics Express,* vol. 22, no. 17, pp. 20652-20662, 2014.

[39] L. Vivien, F. Grillot, E. Cassan, D. Pascal, S. Lardenois, A. Lupu, S. Laval, M. Heitzmann, and J. M. Fédéli, "Comparison between strip and rib SOI microwaveguides for intra-chip light distribution," *Optical Materials,* vol. 27, no. 5, pp. 756-762, 2005.

[40] T. Hiraki, T. Aihara, K. Hasebe, K. Takeda, T. Fujii, T. Kakitsuka, T. Tsuchizawa, H. Fukuda, and S. Matsuo, "Heterogeneously integrated III–V/Si MOS capacitor Mach–Zehnder modulator," *Nat Photon,* vol. 11, no. 8, pp. 482-485, 2017.

[41] P. Abbamonte, G. Blumberg, A. Rusydi, A. Gozar, P. G. Evans, T. Siegrist, L. Venema, H. Eisaki, E. D. Isaacs, and G. A. Sawatzky, "Crystallization of charge holes in the spin ladder of Sr14Cu24O41," *Nature,* vol. 431, no. 7012, pp. 1078-81, 2004.

[42] F. Morichetti, S. Grillanda, and A. Melloni, “Breakthroughs in Photonics 2013: Toward Feedback-Controlled Integrated Photonics,” *IEEE Photonics Journal,* vol. 6, no. 2, pp. 1-6, 2014.

[43] C. Fabry, and A. Perot, “Theorie et applications d’une nouvelle methode de spectroscopie interferentielle,” *Ann. Chim. Phys,* vol. 16, no. 7, pp. 115, 1899.

[44] A. Serpengüzel, G. Griffel, and S. Arnold, “Excitation of resonances of microspheres on an optical fiber,” *Optics Letters,* vol. 20, no. 7, pp. 654-656, 1995.

[45] A. Yariv, “Universal relations for coupling of optical power between microresonators and dielectric waveguides,” *Electronics Letters,* vol. 36, no. 4, pp. 321-322, 2000.

[46] C. B. Dağ, M. A. Anıl, and A. Serpengüzel, “Meandering Waveguide Distributed Feedback Lightwave Circuits,” *Journal of Lightwave Technology,* vol. 33, no. 9, pp. 1691-1702, 2015.

[47] V. Passaro, F. Dell’Olio, C. Ciminelli, and M. Armenise, “Efficient Chemical Sensing by Coupled Slot SOI Waveguides,” *Sensors,* vol. 9, no. 2, pp. 1012, 2009.

[48] J. Song, Q. Fang, S. H. Tao, T. Y. Liow, M. B. Yu, G. Q. Lo, and D. L. Kwong, “Fast and low power Michelson interferometer thermo-optical switch on SOI,” *Optics Express,* vol. 16, no. 20, pp. 15304-15311, 2008.

[49] C. B. Dağ, M. A. Anıl, and A. Serpengüzel, "Novel distributed feedback lightwave circuit elements," *in Proceedings of SPIE Smart Photonic and Optoelectronic Integrated Circuits XVII*, vol. 9366, L. A. Eldada, E.-H. Lee and S. E. He (Eds.), 2015, pp. 93660A-12.

[50] L. Ma, Z. Kang, Y. Qi, and S. Jian, “Tunable dual-wavelength fiber laser based on an MMI filter in a cascaded Sagnac loop interferometer,” *Laser Physics,* vol. 24, no. 4, pp. 045102, 2014.

[51] L. Liu, Q. Zhao, G. Zhou, H. Zhang, S. Chen, L. Zhao, Y. Yao, P. Guo, and X. Dong, “Study on an optical filter constituted by concatenated Hi-Bi fiber loop mirrors,” *Microwave and Optical Technology Letters,* vol. 43, no. 1, pp. 23-26, 2004.

[52] A. L. Steele, “Optical bistability, instabilities and power limiting behaviour from a dual nonlinear optical fibre loop mirror resonator,” *Optics Communications,* vol. 236, no. 1-3, pp. 209-218, 2004.

[53] X. Jiang, J. Wu, Y. Yang, T. Pan, J. Mao, B. Liu, R. Liu, Y. Zhang, C. Qiu, C. Tremblay, and Y. Su, “Wavelength and bandwidth-tunable silicon comb filter based on Sagnac loop mirrors with Mach-Zehnder interferometer couplers,” *Optics Express,* vol. 24, no. 3, pp. 2183-2188, 2016.

[54] L.-Y. Shao, Y. Luo, Z. Zhang, X. Zou, B. Luo, W. Pan, and L. Yan, “Sensitivity-enhanced temperature sensor with cascaded fiber optic Sagnac interferometers based on Vernier-effect,” *Optics Communications,* vol. 336, pp. 73-76, 2015.

[55] X. Sun, L. Zhou, J. Xie, Z. Zou, L. Lu, H. Zhu, X. Li, and J. Chen, “Tunable silicon Fabry-Pérot comb filters formed by Sagnac loop mirrors,” *Optics Letters,* vol. 38, no. 4, pp. 567-569, 2013.

[56] X. Jiang, J. Wu, L. Jiang, Y. Yang, P. Cao, X. Hu, T. Pan, and Y. Su, "Variable bandwidth comb filter based on tunable silicon Sagnac-loop reflectors," *in Proceedings of IEEE 11th International Conference on Group IV Photonics* G.-H. E. Duan (Eds.), 2014, pp. 217-218.

[57] Q. Li, T. Wang, Y. Su, M. Yan, and M. Qiu, “Coupled mode theory analysis of mode-splitting in coupled cavity system,” *Optics Express,* vol. 18, no. 8, pp. 8367-8382, 2010.

[58] L. Zhou, T. Ye, and J. Chen, “Coherent interference induced transparency in self-coupled optical waveguide-based resonators,” *Optics Letters,* vol. 36, no. 1, pp. 13-15, 2011.

[59] Z. Zou, L. Zhou, X. Sun, J. Xie, H. Zhu, L. Lu, X. Li, and J. Chen, “Tunable two-stage self-coupled optical waveguide resonators,” *Optics Letters,* vol. 38, no. 8, pp. 1215-1217, 2013.

[60] X. Sun, L. Zhou, J. Xie, Z. Zou, L. Lu, H. Zhu, X. Li, and J. Chen, “Investigation of Coupling Tuning in Self-Coupled Optical Waveguide Resonators,” *IEEE Photonics Technology Letters,* vol. 25, no. 10, pp. 936-939, 2013.

[61] J. Wu, P. Cao, T. Pan, X. Hu, X. Jiang, L. Jiang, and Y. Su, "High-speed fourth-order photonic differentiator based on silicon self-coupled optical-waveguide resonator," *in Proceedings of IEEE 11th International Conference on Group IV Photonics*, G.-H. E. Duan (Eds.), 2014, pp. 135-136.

[62] Q. Xu, S. Sandhu, M. L. Povinelli, J. Shakya, S. Fan, and M. Lipson, “Experimental realization of an on-chip all-optical analogue to electromagnetically induced transparency,” *Physical Review Letters,* vol. 96, no. 12, pp. 123901, 2006.

[63] X. Sun, L. Zhou, X. Li, Z. Hong, J. Xie, H. Zhu, Z. Zou, L. Lu, and J. Chen, "Experimental demonstration of self-coupled optical waveguide (SCOW)-based resonators," *in Proceedings of IEEE 17th Opto-Electronics and Communications Conference*, S. Bae Lee and K. Kim (Eds.), 2012, pp. 541-542.

[64] L. Zhou, T. Ye, and J. Chen, "Waveguide self-coupling based reconfigurable resonance structure for optical filtering and delay," *Optics Express*, vol. 19, no. 9, pp. 8032-44, 2011.

[65] W.-B. Yan, J.-F. Huang, and H. Fan, "Tunable single-photon frequency conversion in a Sagnac interferometer," *Scientific Reports*, vol. 3, pp. 3555, 2013.

[66] J. Scheuer, and O. Weiss, "The Serpentine Optical Waveguide: engineering the dispersion relations and the stopped light points," *Optics Express*, vol. 19, no. 12, pp. 11517-11528, 2011.

[67] S. Lai, Z. Xu, B. Liu, and J. Wu, "Compact silicon photonic interleaver based on a self-coupled optical waveguide," *Applied Optics*, vol. 55, no. 27, pp. 7550-7555, 2016.

[68] J. Song, L.-W. Luo, X. Luo, H. Zhou, X. Tu, L. Jia, Q. Fang, and G.-Q. Lo, "Loop coupled resonator optical waveguides," *Optics Express*, vol. 22, no. 20, pp. 24202-24216, 2014.

[69] L. Chrostowski, Z. Lu, J. Flueckiger, X. Wang, J. Klein, A. Liu, J. Jhoja, and J. Pond, "Design and simulation of silicon photonic schematics and layouts," *in Proceedings of SPIE Silicon Photonics and Photonic Integrated Circuits V*, vol. 9891, L. Vivien, L. Pavesi and S. E. Pelli (Eds.), 2016, pp. 989114-11.

[70] L. Chrostowski, Z. Lu, J. Flückiger, J. Pond, J. Klein, X. Wang, S. Li, W. Tai, E. Y. Hsu, C. Kim, J. Ferguson, and C. Cone, "Schematic driven silicon photonics design," *in Proceedings of SPIE Smart Photonic and Optoelectronic Integrated Circuits XVIII*, vol. 9751, S. He, E.-H. Lee and L. E. A. Eldada (Eds.), 2016, pp. 975103-14.

[71] W. Chen, Ş. Kaya Özdemir, G. Zhao, J. Wiersig, and L. Yang, "Exceptional points enhance sensing in an optical microcavity," *Nature*, vol. 548, no. 7666, pp. 192-196, 2017.

[72] R. J. Bojko, J. Li, L. He, T. Baehr-Jones, M. Hochberg, and Y. Aida, "Electron beam lithography writing strategies for low loss, high confinement silicon optical waveguides," *Journal of Vacuum Science & Technology B, Nanotechnology and Microelectronics: Materials, Processing, Measurement, and Phenomena*, vol. 29, no. 6, pp. 06F309, 2011.

[73] Richard Bojko. "University of Washington, Washington Nanofabrication Facility," https://ebeam.mff.uw.edu/ebeamweb/process/processmain.html.

[74] M. L. Photonics. http://mapleleafphotonics.com.

[75] M. Caverley. "Python code," https://siepic.ubc.ca/probestation.

[76] P. Connections. www.plcconnections.com.

[77] A. W. Snyder, Y. Chen, D. Rowland, and D. J. Mitchell, “Mismatched directional couplers,” *Optics Letters*, vol. 15, no. 7, pp. 357-359, 1990.